



UNIL | Université de Lausanne

Unicentre

CH-1015 Lausanne

<http://serval.unil.ch>

Year : 2023

Poroelastic Seismic Signatures of Fractured Geothermal Reservoirs

Quiroga Gabriel

Quiroga Gabriel, 2023, Poroelastic Seismic Signatures of Fractured Geothermal Reservoirs

Originally published at : Thesis, University of Lausanne

Posted at the University of Lausanne Open Archive <http://serval.unil.ch>

Document URN : urn:nbn:ch:serval-BIB_811B799B9B8C3

Droits d'auteur

L'Université de Lausanne attire expressément l'attention des utilisateurs sur le fait que tous les documents publiés dans l'Archive SERVAL sont protégés par le droit d'auteur, conformément à la loi fédérale sur le droit d'auteur et les droits voisins (LDA). A ce titre, il est indispensable d'obtenir le consentement préalable de l'auteur et/ou de l'éditeur avant toute utilisation d'une oeuvre ou d'une partie d'une oeuvre ne relevant pas d'une utilisation à des fins personnelles au sens de la LDA (art. 19, al. 1 lettre a). A défaut, tout contrevenant s'expose aux sanctions prévues par cette loi. Nous déclinons toute responsabilité en la matière.

Copyright

The University of Lausanne expressly draws the attention of users to the fact that all documents published in the SERVAL Archive are protected by copyright in accordance with federal law on copyright and similar rights (LDA). Accordingly it is indispensable to obtain prior consent from the author and/or publisher before any use of a work or part of a work for purposes other than personal use within the meaning of LDA (art. 19, para. 1 letter a). Failure to do so will expose offenders to the sanctions laid down by this law. We accept no liability in this respect.



UNIL | Université de Lausanne

Faculté des géosciences
et de l'environnement

INSTITUT DES SCIENCES DE LA TERRE

Poroelastic Seismic Signatures of Fractured Geothermal Reservoirs

THÈSE DE DOCTORAT

Présentée à la

Faculté des Géosciences et de l'Environnement de l'Université de Lausanne

pour l'obtention du grade de Docteur en sciences de la Terre

par

Gabriel Ernesto Quiroga

Directeur de Thèse

Prof. Dr. Klaus Holliger

Co-directeur de Thèse

Dr. J. Germán Rubino

Jury

Dr. Anne Obermann, Experte externe

Dr. Santiago G. Solazzi, Expert externe

Prof. Dr. György Hetényi, Expert interne

Lausanne, 2023

IMPRIMATUR

Vu le rapport présenté par le jury d'examen, composé de

Président de la séance publique :	M. le Professeur Pietro De Anna
Président du colloque :	M. le Professeur Pietro De Anna
Directeur de thèse :	M. le Professeur Klaus Holliger
Co-directeur de thèse :	M. le Docteur German Rubino
Expert interne :	M. le Professeur György Hetényi
Experte externe :	Mme la Docteure Anne Obermann
Expert externe :	M. le Docteur Santiago Solazzi

Le Doyen de la Faculté des géosciences et de l'environnement autorise l'impression de la thèse de

Monsieur Gabriel QUIROGA

*Titulaire d'un
Diplôme de Géophysicien
de l'Université National de La Plata, Argentine*

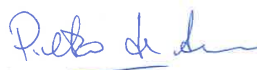
intitulée

POROELASTIC SEISMIC SIGNATURES OF FRACTURED GEOTHERMAL RESERVOIRS

Lausanne, le 20 décembre 2023

Pour le Doyen de la Faculté des géosciences et de l'environnement

Professeur Pietro De Anna



SUMMARY

Understanding the complex physical processes that define the seismic response of heterogeneous rock formations is a prerequisite for reaping the full benefits offered by modern seismic exploration techniques. In particular, understanding the impact of fractures is of interest, as they commonly govern both the mechanical and hydraulic properties of geological formations. When a seismic wave propagates through a fractured and fluid-saturated formation, pressure gradients develop between the softer fractures and the embedding porous background, as well as between connected fractures with different orientations. This in turn causes fluid to flow between the different regions, dissipating energy through viscous friction, and, thus, resulting in seismic attenuation and dispersion. The underlying process is known as wave-induced fluid pressure diffusion (FPD). In contrast to standard elastic modelling approaches, the theory of poroelasticity allows to model the seismic response of fluid-saturated porous rocks formations containing fractures in the mesoscopic scale range, that is, larger than the pore size but smaller than the prevailing seismic wavelength, while naturally accounting for FPD effects. However, poroelasticity is not widely employed as a seismic characterization tool, mainly due to the inherent complexity of this theory. In this Thesis, I explore practically relevant and pertinent scenarios related to enhanced geothermal reservoirs based on the theory of poroelasticity in order to showcase its potential to aid seismic characterization efforts. To do so, I

implement a poroelastic upscaling technique, in combination with a methodology based on the generation of stochastic distributions of fractures with realistic length distributions, which permits to obtain representative seismic signatures accounting for FPD effects.

The first project investigates the impact of wave-induced FPD effects in Rayleigh wave monitoring of reservoirs in fractured crystalline rocks. It is shown that, for the range of seismic frequencies, there is no dispersion or attenuation due to FPD effects, as these frequencies fall in the so-called non-dispersive plateau. This frequency regime prevails when, as a seismic wave passes, there is enough time for fluid pressure equilibration between connected fractures, but not enough time for fluid flow between fractures and background. Consequently, the connectivity of fractures can cause a significant reduction of the stiffening effect of the fluid located within them. This, in turn, has a strong impact on seismic velocity, which can only be appropriately modelled by taking FPD effects into account. The analysis also shows that body wave velocity and Rayleigh wave dispersion are sensitive to the degree of connectivity of fracture networks, as well as to fracture density variations. On the other hand, standard elastic modelling is shown to be insensitive to changes in fracture connectivity. This comparison illustrates the importance of FPD effects, as the degree of connectivity of fractures is a parameter that is of critical importance in the context of geothermal reservoir productivity, and ignoring its impact on seismic data can result in overestimating fracture density changes.

The second project explores the potential of poroelastic modelling to identify partial steam saturation in an otherwise water-saturated fractured geothermal reservoir. A sensitivity analysis shows that partial steam saturation manifests itself primarily as changes in P-wave velocity while the S-wave velocity is practically unchanged. In addition, the results show that while both steam saturation changes and fracture density variations might cause similar changes on the P-wave velocity, their differing effects on the S-wave velocity allow for discrimination between the two scenarios. The impact of partial steam saturation on Rayleigh wave velocities, on the other hand, is shown to be negligible when considering a poroelastic approach, while elastic approaches overestimates this effect. Finally, inversion methods based on seismic reflection amplitude with angle are shown to be sensitive to steam saturation changes and to have the potential to discern between changes due to steam saturation or fracture density variations.

For the third and last project, the detailed characteristics of the poroelastic representation of fractures are explored in order to improve the realism of the modelled seismic response of fractured formations. To do so, existing datasets from the literature are employed to determine relationships between fracture aperture, permeability, and compliance with fracture length. These relationships are then utilized to obtain the seismic response of formations containing fractures at different scales. The fracture density is kept constant to facilitate the analysis. The results show that shorter fractures tend to control the seismic response of fractured formations, and are associated

with lower velocities and higher dispersion and attenuation levels, mainly due to their lower dry frame elastic moduli. It is also shown that the transition frequency associated with FPD effects between connected fractures shifts to lower frequencies for shorter fractures, which causes a significant reduction of the range of frequencies corresponding to the non-dispersive plateau. These characteristics are not appreciated when considering length-independent fracture properties, which can lead to erroneous predictions of the seismic response of fractured formations. The study considers dynamic and static estimations of compliance to derive fracture properties, and it is demonstrated that considering the former results in negligible attenuation and dispersion even for elevated values of fracture density, while the latter is associated with a significant impact on the seismic response of the fractured formation.

Contents

Summary	3
1 Introduction	12
1.1 Motivation	12
1.2 Poroelastic Effects in Fractured Media	18
1.2.1 Numerical Considerations	23
1.2.2 Fracture Network Representation	25
1.3 Thesis Outline	26
List of Figures	11
List of Tables	11
2 Effects of Fracture Connectivity on Rayleigh Wave Disper-	
sion	30
2.1 Abstract	31
2.2 Introduction	32
2.3 Methodology	36

2.3.1	Rayleigh Wave Dispersion	36
2.3.2	Effective Body Wave Properties of Fractured Rocks in a Poroelastic Context	39
2.4	Results	48
2.4.1	Numerical Framework	48
2.4.2	Constant Length Fracture Distributions	51
2.4.3	Stochastic Distribution of Fracture Lengths	59
2.5	Discussion	71
2.6	Conclusions	76
2.7	Acknowledgments	77

3 Seismic Signatures of Partial Steam Saturation in Fractured

	Geothermal Reservoirs: Insights From Poroelasticity	79
3.1	Abstract	80
3.2	Introduction	81
3.3	Methodology	86
3.3.1	Numerical Upscaling Procedure	86
3.3.2	Fracture Network Properties	92
3.3.3	Fluid Pressure Diffusion Effects	95
3.4	Results	99
3.4.1	Seismic Response of Partially Saturated Fractured Gran- ite	99
3.4.2	Impact of Partial Saturation on Seismic Monitoring Techniques	111

3.5	Discussion	124
3.6	Conclusions	128
3.7	Acknowledgments	129
3.8	Appendix A	
	Poroelastic Characterization Workflow	130
3.9	Appendix B	
	Standard Deviation of the Effective Velocities	132
4	Effective Seismic Properties of Fractured Rocks: The Role Played by Fracture Scaling Characteristics	135
4.1	Abstract	136
4.2	Introduction	137
4.3	Length-scaling Fracture Properties	141
	4.3.1 Poroelastic Representation of Fractures	141
	4.3.2 Fracture Aperture	142
	4.3.3 Permeability	146
	4.3.4 Dry Frame Elastic Moduli	147
4.4	Effective Seismic Properties of Fractured Rocks	151
4.5	Seismic Signatures of Formations Containing Fractures With Correlated Properties	157
	4.5.1 Samples With Isolated Fractures	157
	4.5.2 Samples With Connected Fractures	163
	4.5.3 Impact of Fracture Density Definitions	172
4.6	Discussion	176

4.7	Conclusions	179
5	Conclusions and Outlook	183
5.1	Summary and Conclusions	183
5.2	Outlook	189
	References	193

Chapter 1

Introduction

1.1 Motivation

Due to the inherent risks of nuclear energy production, most recently evidenced by the disaster of the nuclear power plant of Fukushima, Japan, in 2011, the energy policy of many developed countries is steering away from continuing the exploitation of nuclear plants. Switzerland, for example, is determined to discontinue the use of nuclear power once the current installations reach the end of their service lives (Swiss Federal Office of Energy, 2021). However, replacing nuclear power is challenging, as its contribution to the overall energy production is significant and unlikely to be able to be rapidly replaceable by conventional renewable energy sources, such as hydraulic, solar or eolic energy. This, in turn, would require to increase the consumption of fossil fuels. The use of fossil fuels has several disadvantages, most importantly the emission of CO₂ and other greenhouse gases. In the

current context of global warming, several countries pledged to reduce the CO₂ emissions to 80-95 % of their emission levels from 1990 by 2050, in accordance with the guidelines of the Intergovernmental Panel on Climate Change (2022, 2022). To satisfy these requirements, replacing the contribution of nuclear power with energy generated from sources with lower carbon footprint than fossil fuels is necessary.

In this context, geothermal energy has a potentially important role to play, as it is an energy source that produces small quantities of harmful emissions and it is, in principle, available everywhere in the world, as temperatures inherently increase with depth. Making use of this geothermal resource, however, is a challenging task. While the energy stored in the rocks at depth is plentiful, retrieving this energy safely and at a reasonable cost is difficult. Throughout the Earth's crust, the main heat distribution mechanism is conduction, which is too slow to be able to produce energy in sufficient quantities for human consumption, as evidenced by the low temperatures we observe on the Earth's surface. Water in the subsurface accelerates heat distribution, and its presence is needed for a location to be considered a geothermal reservoir. Shallower and relatively colder reservoirs are mainly employed to provide calefaction directly, as they are below the threshold for efficient electricity generation of $\sim 100^{\circ}\text{C}$, (e.g., Kohl et al., 2005). Deeper and hotter reservoirs can be used to generate electricity, which is the goal to replace nuclear power plants whose use is being discontinued.

Geothermal reservoirs that are located in sedimentary rocks with high

natural permeabilities are known as hydrothermal reservoirs. One example of such a reservoir in Switzerland is the one located at St. Gallen. This reservoir employed a naturally occurring fault zone as a deep heat exchanger. However, the exploitation of this reservoir was terminated in part due to the associated seismicity that affected the neighboring cities (e.g., Diehl et al., 2017; Edwards et al., 2015). On top of these risks, this type of reservoirs is scarce, and for that the most promising option for the future of electricity generation lies on petrothermal or enhanced geothermal systems (EGS) (Hirschberg et al., 2015). EGS tend to be located in crystalline rock formations with low intrinsic permeabilities. As permeability is a measure of the ability of the fluid to flow through rocks, high permeability values are of utmost importance for energy production in a geothermal context, as effective water circulation is required to efficiently extract heat from the reservoirs. In such rock formations, the most important contribution to the overall permeability of the formation comes from fractures.

Fractures are features commonly found in the Earth's crust and they represent preferential fluid pathways that can significantly increase the overall permeability of a formation. In particular areas, high degrees of fracturing may occur naturally, such as fault zones, but in general, natural fracture systems in crystalline rocks are insufficient for the economical exploitation of a geothermal resource. In these cases, the formation can be stimulated in order to increase the amount of fractures and/or their interconnectivity, since isolated fractures do not contribute to the overall permeability of the

formation. By forcefully injecting fluids and other agents into the formations, fractures can be generated, expanded, or interconnected, thus, increasing the permeability of the reservoir (e.g., Barbier, 2002).

The exploitation of EGS is inherently costlier and riskier than of hydrothermal resources, which makes viability studies particularly important. The information required to estimate the viability of a reservoir ranges from geological structural data to geophysical surveys, thermal and hydraulic borehole measurements (e.g., Kohl et al., 2005). Seismic methods are particularly suited to obtain structural information, alongside with data relating to the rock's properties. There are several examples in the literature of seismic methods employed to characterize and monitor fractured geothermal reservoirs (e.g., Adelinet et al., 2016; Obermann et al., 2015; Taira et al., 2018).

We can differentiate mainly between two types of seismic methods employed in a geothermal reservoirs. On the one hand, we have the seismic reflection method, which is an active method, as it employs artificial sources to generate vibrations, which are then registered by seismometers after having been reflected from contrasts in the material properties in the subsurface (e.g., Yilmaz, 2001). This method is sensitive to impedance contrasts, and it can be used to derive structural maps, P- and S-wave velocity distributions and other parameters, such as P- or S-impedance, derived from amplitude vs angle inversions. Reflection seismic surveys are the non-invasive method with the best resolution available for geothermal exploration, although their costs are elevated. Examples of reflection seismics employed in geothermal

context can be found in Adelinet et al. (2016); Batini and Nicolich (1985); Casini et al. (2010); Gunasekera et al. (2003), among others. On the other hand, passive seismic methods rely on naturally occurring seismic events instead of on artificial sources. In zones with important seismic activity, the energy from local earthquakes can be utilized to image the subsurface. This technique is known as local earthquake tomography. Passive seismic methods that employ natural ambient vibrations to characterize the subsurface are becoming increasingly common. These methods have been employed extensively with the purpose of monitoring geothermal reservoirs around the world (e.g., Taira et al., 2018; Toledo et al., 2022; Sánchez-Pastor et al., 2021) and particularly in Switzerland (e.g., Obermann et al., 2015; Planès et al., 2020; Hillers et al., 2015).

As mentioned before, a detailed characterization of the reservoir properties is paramount, as they determine the viability of a potential site. Particularly, the impact of fractures in the geological formations is of importance, as they greatly affect the effective permeability and storage capacity of rocks, especially considering that EGS are located in rocks with low natural permeability. However, the objective of linking hydraulic properties to the seismic response of rocks is still unresolved. This could be, in part, due to the extensive use of elastic methods to perform modelling and interpretation of seismic data. Models based on linear elasticity neglect complex interactions between the fluid contained within the formations and the host rock frame, making the modelled seismic response insensitive to the hydraulic characteristics of

the formation.

In this regard, the theory of poroelasticity of Biot (1941; 1962) represents a significant improvement over elastic approaches for realistically modelling the seismic response of geological formations. This theory allows to consider the movement of the pore fluid with respect to the rock's elastic frame, which, in turn, causes energy dissipation. This points to the fact that modelling the seismic response under the scope of Biot's theory is more likely to find connections between the hydraulic properties of geological formations and their seismic response.

The literature on methodological works based on the theory of poroelasticity documents several breakthroughs in the last decade, which have yet to be incorporated into applied characterization efforts. The objective of this thesis is to bridge the gap between the necessities of geothermal exploration for more accurate models and the recent developments in the realm of poroelasticity. The hypothesis on which this work is based on is that the use of poroelastic modelling can improve the interpretation of seismic data in the context of monitoring of geothermal reservoirs. In particular, this thesis aims to determine whether poroelastic effects can substantially affect seismic data from fractured reservoirs, and whether accounting for these poroelastic effects can improve the characterization of these environments. In the following, I present a brief introduction to the theory of poroelasticity in general and its relevance to fracture media in particular. I then proceed with a brief description of the basic methodology employed in the course of the

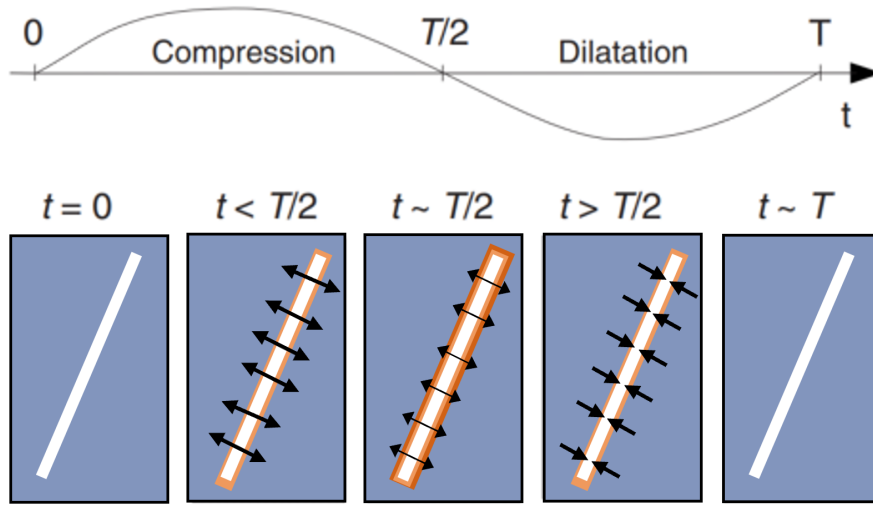


Figure 1.1: Schematic illustration of wave-induced fluid flow (WIFF) in the presence of fractures. During the compression cycle of a wave with period T , there is fluid flow from the softer fractures towards the stiffer background, as indicated by the arrows. Conversely, during the extension cycle of the wave, the fluid flow direction reverses. Orange colors denote the pressure gradients next to the fractures. Modified from Müller et al. (2010).

research. Finally, I present an outline of the projects that constitute the main contribution of this thesis.

1.2 Poroelastic Effects in Fractured Media

Fractures are ubiquitous throughout the Earth's upper crust and are characterized by strongly differing mechanical and hydraulic properties with respect to the embedding background. For these reasons, fractures tend to

control the effective mechanical and hydraulic properties of the formation. Consequently, the study of fractures is of vital importance for applications of economic or environmental importance, such as tunneling, hydrocarbon exploration, CO₂ sequestration, and, in particular, the exploration and monitoring of geothermal reservoirs. Fractures prevail over a wide range of scales (e.g., Vermilye and Scholz, 1995; Bonnet et al., 2001), from the regional scale all the way down to the microscopic one.

Seismic waves travelling through fractured media tend to experience an increase in attenuation, dispersion, and scattering as well as a general decrease in the overall propagation velocity. The relative scale of the fractures with respect to the prevailing seismic wavelengths determines which physical mechanisms dominate. Mesoscopic scale fractures, which are the focus of this study, are much smaller than the prevailing wavelengths, but much larger than the pore scale. These fractures are of particular interest, as they are below the resolution of seismic methods while having significant impact on the hydraulic and mechanical properties of the medium. For these reasons, it is important to properly take into account the effects that these fractures have in the seismic response of the formations that contain them in order to determine if seismic methods can be used to infer properties of interest, such as fracture density or connectivity, which may have a direct impact on the productivity of a reservoir.

When a seismic wave travels through a formation containing mesoscale fractures, pore fluid pressure gradients arise between the softer fractures and

the stiffer embedding background as well as between interconnected fractures (e.g., Rubino et al., 2013, 2014, 2016; Vinci et al., 2014; Gurevich et al., 2009). These pressure imbalances generate oscillatory fluid flow, which, due to viscous losses, dissipates the energy of the seismic wave. A schematic illustration of this phenomenon is shown in Figure 1.1. This fluid flow can occur between the fractures and their embedding background, generating what is known as fracture-to-background fluid pressure diffusion (FB-FPD), as well as between connected fractures of different orientations, generating what is known as fracture-to-fracture FPD (FF-FPD) (Rubino et al., 2013, 2014). Figures 1.2a to 1.2c show the pressure distribution of a sample, representative of a fractured formation, composed of two orthogonally intersecting fractures in response to an oscillatory vertical compression, which emulates the strains produced by a vertically traveling P-wave. Figures 1.2d to 1.2f show a schematic representation of the direction of the corresponding wave-induced fluid flow. For lower frequencies, as shown in Figures 1.2a and 1.2d, there is enough time in a wave semi-cycle for pressure to equilibrate between the connected fractures, whereas fluid flow is established between the fractures and the background. This is the FB-FPD phenomenon, and it occurs for lower frequencies than FF-FPD as the embedding background has significantly lower permeabilities than the fractures. The reason for this is that more time is needed to establish hydraulic communication between the fractures and the background than between interconnected fractures. Figures 1.2b and 1.2e illustrate FF-FPD, where fluid flow and, thus, velocity disper-

sion and attenuation, is caused by local fluid pressure gradients occurring between intersecting fractures having different orientations. For this frequency range, there is not enough time in a semi-cycle for fluid flow to occur between fractures and background, but there is enough time for fluid to flow between fractures, as the permeability of fractures is higher than that of the background. Finally, above the frequency range at which FF-FPD prevails, there is not enough time in a semi-cycle for fluid to flow between fractures and background, or between connected fractures, and the sample behaves as if fractures were hydraulically isolated. This is the so-called no-flow or elastic limit, beyond which the medium essentially behaves elastically (Figures 1.2c and 1.2f).

The energy losses caused by the movement of the viscous pore fluid manifest themselves in the form of seismic attenuation and velocity dispersion. Figure 1.3 shows a schematic representation of the behaviour of body wave velocities of formations containing connected fractures (blue line) and formations that do not (red line) as a function of frequency. As explained before, FB-FPD prevails for lower frequencies and FF-FPD prevails for higher frequencies. These regimes are shown highlighted in yellow and it can be seen that are the frequency ranges where velocity dispersion is present. For frequencies lower than those corresponding to FB-FPD, the so-called low-frequency limit is obtained, which is compatible with Gassmann's (1951) fluid substitution approach. The frequencies between both dispersion regimes constitute the so-called non-dispersive plateau, which, for low permeability

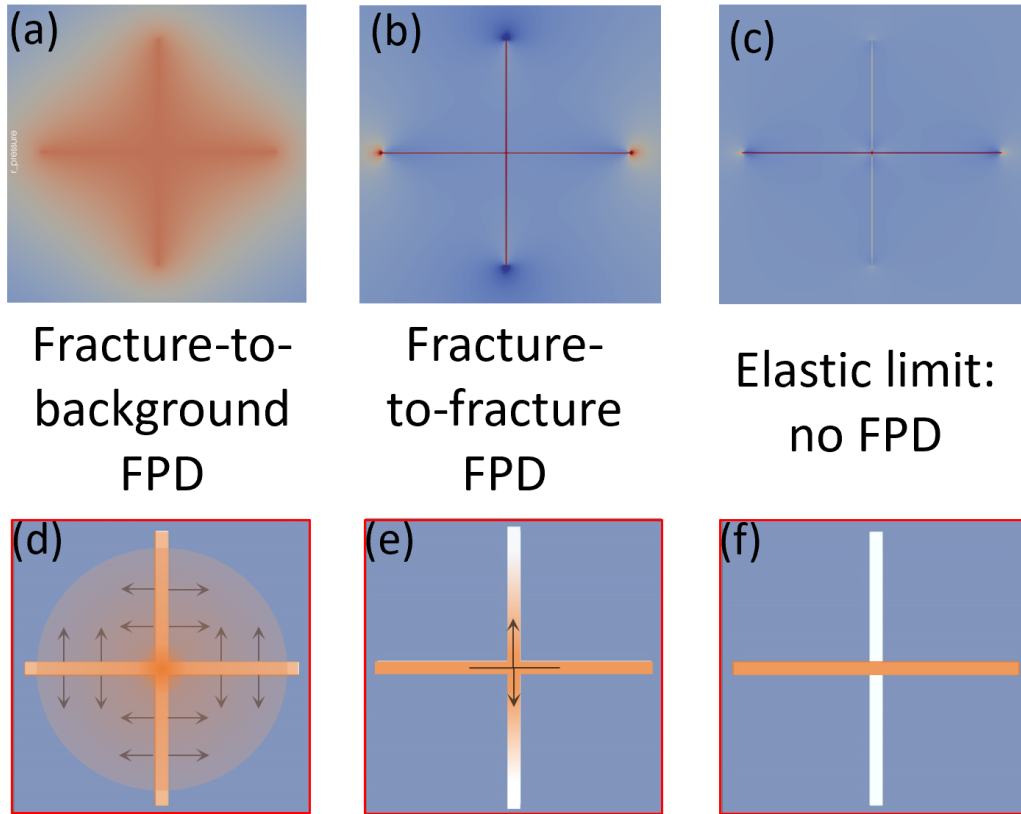


Figure 1.2: (a, b, c) Fluid pressure distributions in an orthogonally intersecting fracture pair subjected to a vertical compression for different dispersion regimes. Increasing pressure is denoted by progressive intensities of orange. (a) FB-FPD: pressure exchange between fractures and background rock; (b) FF-FPD: pressure exchange between connected fractures; (c) elastic equivalent case: pressure confined to the horizontal fracture. Schematic illustrations of fluid flow in the formation for the different dispersion regimes, (d) FB-FPD; (e) FF-FPD; and (f) elastic limit.

formations, it encompasses the typical seismic frequency range. Although there is neither attenuation nor velocity dispersion in this frequency range, FPD effects in the presence of connected fractures produce a significant velocity drop. This velocity reduction in the case of connected fractures is due to a reduction of the stiffening effect of the fracture fluid in response to fluid pressure release into connected fractures. This means that, even though the characteristic of body wave velocities in the plateau are representative of an elastic medium, the associated velocity change can only be modelled in the context of the theory of poroelasticity. Finally, for frequencies higher than those corresponding to FF-FPD, the samples behave as if fractures were hydraulically isolated, which is consistent with an elastic characterization of the medium.

1.2.1 Numerical Considerations

To obtain effective seismic properties of a porous medium containing mesoscale fractures, a corresponding representative elementary volume (REV) is subjected to numerical relaxation tests consisting of harmonic displacements applied on its boundaries (e.g., Rubino et al., 2009). A sample corresponds to a REV (i) if it is structurally typical of the studied rock volume and (ii) if the inferred seismic properties are independent of the boundary conditions applied (e.g., Milani et al., 2016; Caspari et al., 2016). However, the numerical simulation of wave propagation accounting for the effects of mesoscale fractures on seismic attenuation and dispersion is computationally

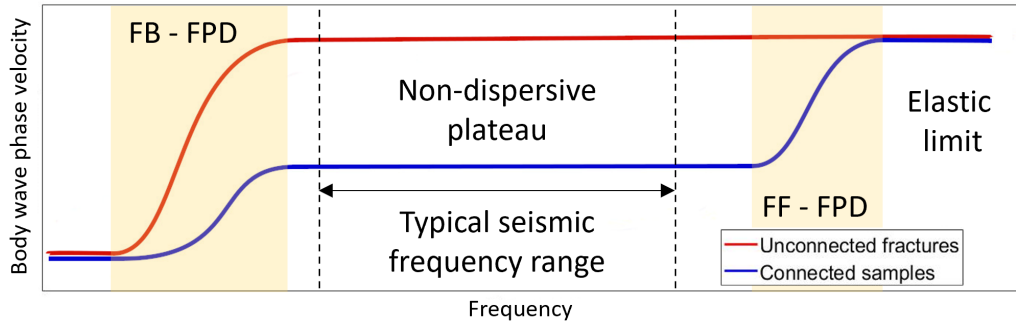


Figure 1.3: Schematic representation of the body wave phase velocity in the presence of (blue) connected and (red) unconnected fractures as function of frequency. Highlighted in yellow are the FB-FPD and FF-FPD dispersion regimes. Between these regimes a non-dispersive plateau is situated, which, for low-permeability formations, tends to comprise the frequency range typically used in seismic exploration. For frequencies higher than those corresponding to FF-FPD, there is no time in a half-cycle to produce WIFF and the medium behaves elastically.

prohibitive, due to the very fact that the scale, at which these effects prevail, is much smaller than the seismic wavelengths (e.g., Rubino et al., 2016). To circumvent this problem, in this thesis I employ effective-medium-type upscaling approaches to model the response of fractured formations containing realistic fracture length distributions. These methods have proven to be an efficient means of characterizing FPD effects in formations containing mesoscale heterogeneities and/or fractures. The particularities of the numerical procedure employed is described in detail in each of the chapters, which are standalone scientific works.

1.2.2 Fracture Network Representation

In order to produce realistic models of fractured rocks, it is important to represent the key features of natural fracture networks as closely as possible. In a poroelastic setting, fractures are represented by their geometrical characteristics, porosity, permeability, dry frame bulk and shear moduli, and the mechanical properties of the grains. Several authors (e.g., de Dreuzy et al., 2001; Bonnet et al., 2001; Hatton et al., 1994; Vermilye and Scholz, 1995) have studied the statistical properties of fractures, such as length, aperture, and permeability, among others. The distribution of length of fractures can be reproduced by means of a power law distribution. For this thesis, I employ the following equation, (e.g., Hunziker et al., 2018; de Dreuzy et al., 2001; Bonnet et al., 2001)

$$n(L) = F_d(a - 1) \frac{L^{-a}}{L_{min}^{1-a}}; L \in [L_{min}, L_{max}], \quad (1.1)$$

where L is the fracture length, $n(L)$ is the density function quantifying the number of fractures in the considered fractured formation with a length comprised between L and $L + dL$, where dL denotes an infinitesimal increment of length, a is the so-called characteristic exponent of the fracture size distribution, and L_{min} and L_{max} are the minimum and maximum length values, respectively. The exponent a can take values between 1.5 and 3 and controls the prevalence of shorter to longer fractures within the limits given by L_{min} and L_{max} . F_d is the fracture density, which, in 2D, is computed as the ratio of the fracture area over the total sample area.

With regard to the aperture of the fractures, for the two initial projects of

the thesis, a constant aperture for the fractures is chosen, which, alongside the considered lengths, result on a range of aspect ratios compatible with the available evidence found in nature (e.g., Vermilye and Scholz, 1995). Similarly, the rest of the properties are considered as homogeneous. The third project accounts for the fact that the compliance, aperture and permeability of fractures scale with their lengths, based on empirical relationships that are described in the corresponding methodology.

1.3 Thesis Outline

Having introduced the basic concepts that are common to the research documented in this thesis, the next three chapters correspond to associated scientific manuscripts. The first two manuscripts have been published in *Journal of Geophysical Research: Solid Earth and Geophysics*, respectively, while the third manuscript is still under preparation.

Chapter 2 presents the initial manuscript produced during my PhD work. In this manuscript, the impact of poroelastic effects on Rayleigh wave velocity dispersion of fractured formations is studied. This work was motivated by the proliferation of passive seismic approaches being employed as monitoring tools for geothermal reservoirs. In this work, sensitivity analyses are performed that compare poroelastic and elastic approaches, in order to understand the interpretation problems an inadequate modelling could cause on monitoring efforts. The effects of fracture connectivity and fracture density are also studied and it is demonstrated that these two factors play important

roles on the seismic response of fractured formations.

Chapter 3 is based on the context of high-enthalpy fractured geothermal reservoirs and explores the potential for seismic methods to detect the presence of steam. The methodology employed is similar to that of the previous chapter with the inclusion of partial saturation into the models. Sensitivity analyses are carried out to determine the behavior of body wave velocities, which are compared to the results of the preceding chapter. The objective is to identify seismic characteristics to show possible interpretation tools to differentiate between fracture density and steam saturation changes. The manuscript is then completed with an analysis of Rayleigh wave velocity dispersion and of a seismic reflection amplitude with incidence angle study to showcase the impact of partial steam saturation in those methods.

Chapter 4 revisits the conceptualization of fractures as poroelastic inclusions. Specifically, I seek to explore the impact that more realistic fracture modelling may have on the seismic response of fractured formations. This is achieved by employing data from different works to determine empirical relationships between fracture length and aperture, permeability and compliance. The results are shown for simple geometries that allow to understand the governing physical processes involved and to determine the possible impact in applied scenarios.

The subsequent concluding remarks summarize the results and the importance of accounting for poroelastic effects when modelling the seismic response of geothermal reservoirs. Finally, a brief outlook into possible future

works that could expand this line of research is given.

Chapter 2

Effects of Fracture Connectivity on Rayleigh Wave Dispersion

Gabriel E. Quiroga¹, J. Germán Rubino², Santiago G. Solazzi¹, Nicolás D.
Barbosa¹, and Klaus Holliger¹

¹ Institute of Earth Sciences, University of Lausanne, Lausanne,
Switzerland.

² CONICET, Centro Atómico Bariloche - CNEA, San Carlos de Bariloche,
Argentina.

Published as: Quiroga, G. E., Rubino, J. G., Solazzi, S. G., Barbosa, N. D.,
and Holliger, K. (2022). Effects of fracture connectivity on Rayleigh wave
dispersion. *Journal of Geophysical Research: Solid Earth*, 127(3),
e2021JB022847.

2.1 Abstract

Passive seismic characterization is an environmentally friendly method to estimate the seismic properties of the subsurface. Among its applications, we find the monitoring of geothermal reservoirs. One key characteristic to ensure a productive management of these reservoirs is the degree of fracture connectivity and its evolution, as it affects the flow of fluids within the formation. In this work, we explore the effects of fracture connectivity on Rayleigh wave velocity dispersion accounting for wave-induced fluid pressure diffusion (FPD) effects. To this end, we consider a stratified reservoir model with a fractured water-bearing formation. For the stochastic fracture network prevailing in this formation, we consider varying levels of fracture density and connectivity. A numerical upscaling procedure that accounts for FPD effects is employed to determine the corresponding body wave velocities. We use a Monte-Carlo-type approach to obtain these velocities and incorporate them in the considered fractured reservoir model to assess the sensitivity of Rayleigh wave velocity dispersion to fracture connectivity. Our results show that Rayleigh wave phase and group velocities exhibit a significant sensitivity to the degree of fracture connectivity, which is mainly due to a reduction of the stiffening effect of the fluid residing in connected fractures in response to wave-induced FPD. These effects cannot be accounted for by classical elastic approaches. This suggests that Rayleigh wave velocity changes, which are commonly associated with changes in fracture density, may also be related to changes in interconnectivity of pre-existing or newly generated fractures.

Plain Language Summary

Low-intensity seismic energy generated by natural or anthropogenic sources is used to obtain a number of physical properties of the subsurface. Amongst a wide range of applications, this technique is increasingly employed to characterize fractured geothermal reservoirs and to monitor their evolution. The interconnectivity of fractures is a critical characteristic of such reservoirs as it enables preferential pathways for fluid flow. Conventional models for interpreting such seismic data are based on linear elasticity and cannot account for realistic effects related to the interactions of pore fluid pressure and fracture connectivity. To alleviate this problem, we employ an advanced model that accounts for these so-called wave-induced fluid pressure diffusion (FPD) effects. We find that changes in the connectivity of fractures have a significant impact on seismic surface wave recordings. This opens the perspective of using such observations to monitor the hydraulic evolution of fractured reservoirs during successive production and stimulation cycles.

2.2 Introduction

Fractured rock formations are of increasing interest and importance for a wide range of applications throughout the Earth, environmental, and engineering sciences. Fractures tend to constitute preferential pathways for fluid flow and, as such, the hydraulic properties of a formation are greatly affected by the presence and connectivity of fractures. This, in turn, manifests itself

in the need of new methods and techniques to detect fractures and characterize their geometrical, mechanical, and hydraulic properties. In this context, the use of passive seismic sensing to monitor the evolution of fracture networks has established itself due to its efficiency, reliability, and non-invasive nature. Prominent examples of scenarios where this technique has proven to be valuable include the monitoring of volcanic activity (e.g., Brenguier et al., 2008; Obermann et al., 2013), CO₂ sequestration (e.g., Boullenger et al., 2015; Gassenmeier et al., 2014), and geothermal energy production (e.g., Calò et al., 2013; Obermann et al., 2015; Taira et al., 2018).

Passive seismic methods comprise a vast range of approaches and techniques which employ the energy of naturally occurring seismicity to gain information of the subsurface. In active seismic regions, the energy released from natural earthquakes in the area can be used for this purpose. This method is known as local earthquake tomography (LET) (e.g., Aki and Lee, 1976; Thurber, 1983). Conversely, ambient-noise correlation or passive seismic interferometry is a passive seismic method based on surface wave analysis which is also applicable outside seismically active zones. Ambient-noise correlation is based on the inversion of Rayleigh wave velocity dispersion inferred from ambient seismic noise measurements to obtain S-wave velocity profiles of the studied zone. Even though this method initially started with pioneering works focused at the continental and regional scale (e.g., Campillo and Paul, 2003; Shapiro and Campillo, 2004), it quickly evolved towards smaller scales, proving its effectiveness as an exploration and monitoring tool for ap-

plications such as, for example, nuclear waste storage and CO₂ sequestration, which naturally target zones with low natural seismicity (Planès et al., 2020). Notably, this technique was employed successfully in the characterization of geothermal reservoirs by employing time lapse observations. Obermann et al. (2015) employed ambient-noise correlation in order to monitor the geothermal site of St. Gallen in Switzerland, which permitted the identification of aseismic perturbations associated with gas infiltration. More recently, Taira et al. (2018) used ambient-noise correlation to monitor the response of the Salton Sea geothermal site in the U.S.A. to fluid extraction and local earthquake activity. Interestingly, these authors attributed observed surface wave velocity reductions to the opening of preexisting fractures due to induced stresses. In addition to this, it can be expected that fluid pressure diffusion (FPD) effects play a role in this scenario, as in the presence of fluid saturated fractures, such poroelastic effects have a significant impact on the effective mechanical properties of the medium in response to seismic waves (e.g., Rubino et al., 2013, 2014, 2017). To date, surface wave analyses do not, however, account for wave-induced FPD.

When seismic waves travel through a fluid-saturated porous medium containing a distribution of mesoscopic fractures, that is, fractures larger than the typical pore size but much smaller than the prevailing seismic wavelengths, fluid pressure gradients are induced between compliant fractures and the stiffer embedding background, as well as between connected fractures (e.g., Rubino et al., 2013, 2014). The consequent pressure equilibration

processes, usually referred to as fracture-to-background (FB) and fracture-to-fracture (FF) FPD, result in a frequency dependence of the effective mechanical moduli of the medium. The prevalence of these mechanisms is dependent on the frequency of the seismic waves. In low-permeability formations and in presence of centimeter- to meter-scale fractures, FB-FPD typically prevails at frequencies below the seismic frequency range ($\lesssim 0.01$ Hz), while FF-FPD occurs at frequencies above the seismic frequency range ($\gtrsim 10^3$ Hz). The effects of FPD on body wave velocities of fractured rocks were extensively studied, and it was demonstrated that the density, connectivity and orientation of fractures have a significant impact on the phase velocity dispersion and attenuation as well as on the anisotropy of body wave velocities (e.g., Gurevich et al., 2009; Vinci et al., 2014; Rubino et al., 2017; Solazzi et al., 2020). However, the corresponding impact on surface wave properties, such as, for example, their velocity dispersion characteristics, in the context of subsurface exploration and monitoring settings remains largely unexplored. Previous works associate surface wave velocity decreases in seismically active environments with the opening of fractures and the associated increases of fracture density (e.g., Silver et al., 2007; Taira et al., 2015, 2018). However, this interpretation ignores the possibility that changes in the fracture density may also be associated with changes in the connectivity between fractures and disregards the associated FPD effects on the properties of surface waves.

The aim of this work is to explore the importance of fracture-related FPD effects on surface wave velocity dispersion. Our main objective is to better

understand the effects that fractures in general, and their interconnectivity in particular have on this widely used observable. The paper proceeds as follows. We begin by explaining the method used to compute synthetic Rayleigh wave dispersion curves in elastic layered media. We then outline of the theoretical basis of poroelasticity and the associated upscaling procedure employed to compute the effective seismic properties of fractured formations. Then, we consider a canonical model to explore the effects of FPD for a wide range of pertinent parameters, which allow us to systematically explore the effects of fracture density and interconnectivity on Rayleigh wave phase and group velocities. To assure the representativity of our results, we use a Monte Carlo approach to explore the corresponding parameter space. Rayleigh wave dispersion curves are analyzed for fracture distributions characterized by constant and variable length in order to determine if the multiplicity of scales prevailing in many natural settings has significant impact on the results.

2.3 Methodology

2.3.1 Rayleigh Wave Dispersion

Rayleigh waves propagate along the Earth's free surface as a superposition of P-waves and vertically polarized S-waves. They are characterized by a counter-clockwise elliptical particle motion, whose amplitude decays exponentially with distance from the free surface. Conversely, geometrical spreading effects are very small compared to those of body waves, and, hence,

Rayleigh waves tend to be prevalent in seismic recordings (e.g., Stein and Wysession, 2003). In a stratified medium with varying seismic velocities, Rayleigh wave propagation is dispersive, which manifests itself in a prominent frequency dependence of their phase velocities. The reason for this is that different frequencies are associated with different wavelengths and, thus, with different sensitivity to depth. Correspondingly, passive seismic approaches allow to characterize the subsurface through the inversion of Rayleigh wave dispersion curves extracted from ambient noise records (e.g., Socco et al., 2010; Wang and Yao, 2020).

We consider a layered medium whose axis of symmetry is normal to the surface and impose the following boundary conditions for waves travelling in a layered half-space in contact with a free surface: (i) no stress at the surface; (ii) no stress and strain at infinite depth; (iii) continuity of stress and displacements at layer interfaces; (iv) plane strain field. In this context, the equation of motion can be written as a linear differential eigenvalue problem (e.g., Aki and Richards, 1980)

$$\frac{d\mathbf{f}(z)}{dz} = \mathbf{A}(z)\mathbf{f}(z), \quad (2.1)$$

where \mathbf{f} is a vector composed of two displacement eigenfunctions and two stress eigenfunctions, \mathbf{A} is a 4x4 matrix depending on the vertical distribution of the of the subsurface properties and z is the vertical coordinate. Equation 1 has nontrivial solutions for certain values of the wavenumber. The associated equation is known as the Rayleigh secular equation and in its implicit form

is given by (e.g., Socco et al., 2010)

$$F_R[\lambda(z), G(z), \rho(z), k_j, f] = 0, \quad (2.2)$$

where λ and G are the Lamé parameters, ρ is the density, k_j is the wavenumber of the mode of propagation j , and f is the frequency. The variables corresponding to the material parameters of the subsurface depend on z . For a stratified medium where each layer has homogeneous mechanical properties, this problem can be expressed using a matrix formulation, as shown by the works of Thomson (1950) and Haskell (1953). These authors introduced the so-called matrix propagator method which conceptualizes the subsurface as a stack of layers overlying a semi-infinite half-space. These algorithms are commonly employed for the computation of Rayleigh wave dispersion curves for a wide variety of applications. Buchen and Ben-Hador (1996) provide a review of the most significant propagator matrix algorithms and introduce the so-called “fast delta matrix” method, which we use in this study. The procedure to determine the associated Rayleigh wave phase and group velocities consists of finding the roots of the Rayleigh secular equation (Equation 2), for which we use the secant method (e.g., Press et al., 1986). The fast delta matrix method employed here provides exact solutions for models consisting of a stack of horizontal, elastic, and isotropic layers.

The objective of this work is to assess the effects of FPD in porous media containing fracture networks on Rayleigh wave dispersion. To this end, we will consider a layered subsurface model in which one of the layers represents a fractured formation. In this context, various scenarios of fracture connec-

tivity are considered for Rayleigh wave dispersion modelling. The effective body wave velocities of the fractured formation required to compute Rayleigh wave dispersion are obtained by employing a numerical upscaling procedure, which is described in the following section.

2.3.2 Effective Body Wave Properties of Fractured Rocks in a Poroelastic Context

In the following, we briefly describe the effects of FPD on the seismic signatures of fractured rocks. This is followed by a brief review of Biot’s poroelasticity theory (Biot, 1962), which is subsequently employed to model FPD effects in fractured porous media. To do so, we employ the numerical upscaling procedure proposed by Rubino et al. (2016), which was recently implemented into a versatile finite-element package named “Parrot” and allows to consider stochastic fracture distributions of realistic complexity (Favino et al., 2020).

Fluid Pressure Diffusion Effects

When a seismic wave propagates through a fluid-saturated porous medium containing fractures in the mesoscopic scale range, FPD affects its phase velocity and amplitude. In presence of connected fractures, two manifestations of FPD can arise (Rubino et al., 2013): one is governed by FPD between compliant fractures and their stiffer embedding background and is referred to as FB-FPD; the other is associated with FPD between connected

fractures and is referred to as FF-FPD. Figures 2.1a to 2.1c show a representative rock sample of a medium of interest being subjected to harmonic displacements applied on its boundaries, which allow us to obtain the associated effective frequency-dependent elastic moduli (Rubino et al., 2016). Figures 2.1d to 2.1g show schematic illustrations of FPD effects in terms of the pressure distribution in a subsection of a fractured sample subjected to vertical compression (Figure 2.1a), which emulates the strains produced by a vertically travelling P-wave. Orange-colored regions of the medium denote the fluid pressure build-up created by the harmonic deformation and black arrows indicate the direction of the corresponding wave-induced fluid flow. The large stiffness contrast between fractures and background generates pressure gradients in response to the propagation of a seismic wave, which, in turn, generate oscillatory fluid flow between these regions and, thus, energy dissipation and velocity dispersion due to FB-FPD (Figure 2.1d). Figure 2.1f illustrates FF-FPD, where fluid flow and, thus, velocity dispersion and attenuation, is caused by local fluid pressure gradients occurring between intersecting fractures. Above the frequency range at which FF-FPD prevails, the sample behaves as if fractures were hydraulically isolated. This is the so-called no-flow limit, beyond which the medium essentially behaves elastically (Figure 2.1g). As mentioned before, for crystalline rocks, FB-FPD falls below the frequencies typical of passive seismic surveys, while FF-FPD corresponds to frequencies higher than those of passive seismics. As illustrated in Figure 2.1e, between these regimes we find a frequency range characterized by pres-

sure equilibrium between connected fractures, which substantially reduces the stiffening effect of the fracture fluid compared to the elastic case. Figure 2.1h then presents an illustration of the associated body wave phase velocity as a function of frequency for samples containing connected and unconnected fractures. The FB-FPD and FF-FPD dispersion ranges are highlighted in yellow. For frequencies higher than the FB-FPD regime and lower than the FF-FPD regime, there is a non-dispersive plateau in which the medium behaves effectively as being elastic. Although there is neither attenuation nor velocity dispersion in this frequency range, FPD effects in presence of connected fractures produce a significant velocity drop. This means that, even though the body wave velocities in the plateau are representative of an elastic medium, this velocity change can only be modelled in the context of the theory of poroelasticity. For many applications of interest, the frequency range of approximately 0.1 to 10 Hz, at which passive seismic surveys are usually carried out (e.g., Obermann et al., 2015; Taira et al., 2018) is within the limits of this non-dispersive plateau. This implies that, as long as the frequencies considered correspond to those of the non-dispersive plateau, an elastic modelling such as the one described in Section 2.1 can be employed to evaluate Rayleigh wave dispersion in layered media.

Numerical Upscaling Procedure

The direct numerical simulation of FPD effects on wave propagation is a complicated task. This is mainly due to the fact that the dominant scales

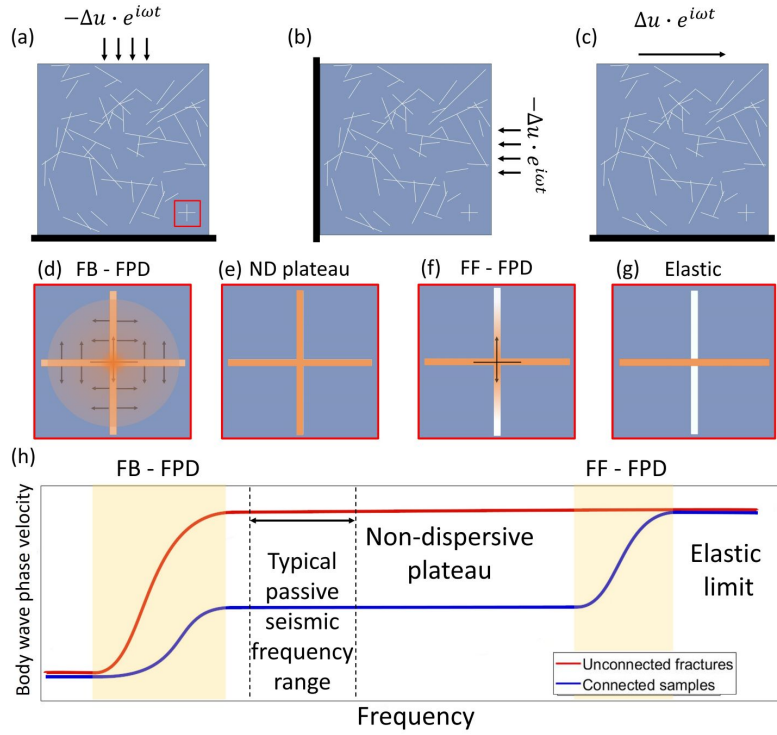


Figure 2.1: Schematic illustration of the (a) vertical, (b) horizontal, and (c) shear numerical oscillatory relaxation tests employed to obtain the equivalent stiffness matrix of the considered sample. (d, e, f, g) Fluid pressure distributions in a subsection of the sample highlighted in (a) subjected to a vertical compression for different dispersion regimes. Increasing pressure is denoted by progressive intensities of orange. (d) FB-FPD: pressure exchange between fractures and background rock, (e) non-dispersive (ND) plateau: pressure is equilibrated between connected fractures; (f) FF-FPD: pressure exchange between connected fractures; (g) elastic equivalent case: pressure confined to the horizontal fracture. (h) P- and S-wave velocities as functions of frequency for samples with unconnected fractures (red line) and connected fractures (blue line). The frequency ranges where body wave dispersion due to FB-FPD and FF-FPD prevails are highlighted in yellow. Typical frequency range of passive seismic studies is shown inside the ND plateau.

at which FPD takes place are much smaller than the seismic wavelengths (Rubino et al., 2016). For this reason, numerical upscaling procedures are commonly employed to achieve an effective characterization of heterogeneous poroelastic media. In order to obtain the effective upscaled seismic response of a medium of interest, we solve Biot's equations for a so-called representative elementary volume (REV) of the medium. An REV is defined as a subvolume that is structurally typical of the whole medium and for which the inferred properties are independent of the applied boundary conditions (e.g., Milani et al., 2016). Fractures are conceptualized as highly porous, permeable, and compliant inclusions embedded in a much stiffer and much less porous permeable background (e.g., Nakagawa and Schoenberg, 2007). As seismic attenuation and velocity dispersion due to FPD are governed by fluid pressure gradients, we can neglect inertial terms (e.g., Rubino et al., 2013). Hence, Biot's poroelastic equations of motion (Biot, 1956a,b) reduce to the so-called consolidation equations (Biot, 1941), which, in the space-frequency domain are given by

$$\nabla \cdot \boldsymbol{\sigma} = 0, \quad (2.3)$$

$$\nabla p_f = -i\omega \frac{\eta}{\kappa} \mathbf{w}, \quad (2.4)$$

where $\boldsymbol{\sigma}$ is the total stress tensor, p_f the pore fluid pressure, η the fluid viscosity, κ the permeability, ω the angular frequency, and \mathbf{w} the relative fluid-solid displacement. These equations are coupled by the stress-strain constitutive relations (Biot, 1962)

$$\boldsymbol{\sigma} = 2\mu_m \boldsymbol{\epsilon} + \mathbf{I}(\lambda_c \nabla \cdot \mathbf{u} - \alpha M \xi), \quad (2.5)$$

$$p_f = -\alpha M \nabla \cdot \mathbf{u} + M \xi, \quad (2.6)$$

where \mathbf{I} is the identity matrix, \mathbf{u} the solid displacement, and $\xi = -\nabla \cdot \mathbf{w}$ a measure of the local change in the fluid content. The strain tensor is given by $\boldsymbol{\epsilon} = \frac{1}{2}(\nabla \mathbf{u} + (\nabla \mathbf{u})^T)$, where the superscript T denotes the transpose operator. The Biot-Willis parameter α , the inverse of the fluid storage coefficient M , and the Lamé parameter λ_c are given by

$$\alpha = 1 - \frac{K_m}{K_s}, \quad (2.7)$$

$$M = \left(\frac{\alpha - \phi}{K_s} + \frac{\phi}{K_f} \right)^{-1}, \quad (2.8)$$

and

$$\lambda_c = K_m + \alpha^2 M - \frac{2}{3} \mu_m, \quad (2.9)$$

where ϕ denotes the porosity, μ_m the shear modulus of the bulk material, which is equal to that of the dry frame, and K_f , K_s , and K_m are the bulk moduli of the fluid phase, the solid grains, and the dry matrix, respectively. Please note that the dry frame modulus K_m is related to the undrained saturated modulus K_u through Gassmann's equation $K_m = K_u - \alpha^2 M$ (Gassmann, 1951). Due to computational constraints, we employ a 2D characterization for our medium under the hypothesis of plane strain conditions. The plane strain assumption implies that the considered fractures are long enough in the direction perpendicular to the considered plane of wave propagation to neglect pressure gradients, as well as normal and shear strains along this direction. This also implies that the seismic waves are assumed to propagate along the plane of the sample. In order to characterize the full

stiffness matrix of a 2D medium, we apply three oscillatory relaxation tests to a corresponding REV, whose boundary conditions are illustrated in Figure 2.1. The first test consists of a harmonic vertical compression (Figure 2.1a), performed by applying a time-harmonic homogeneous vertical displacement at the top boundary of the representative sample, while keeping the vertical displacement of the sample null at the bottom boundary. The second test is a harmonic horizontal compression test (Figure 2.1b) and consists on applying a normal displacement at a lateral boundary of the sample, while keeping the horizontal displacement null at the opposing boundary. The third and final test consist of applying a harmonic horizontal displacement at the top boundary of the sample, while keeping the bottom boundary fixed in place (Figure 2.1c). Following Favino et al. (2020), the displacements and pressures obey periodic boundary conditions unless stated otherwise.

Given that a heterogeneous poroelastic medium can be represented by an effective homogeneous viscoelastic solid (e.g., Rubino et al., 2016; Solazzi et al., 2016), the volumetric average of stress and strain, in response to the three tests, can be related through an equivalent frequency-dependent and anisotropic stiffness matrix (Rubino et al., 2016)

$$\begin{pmatrix} \langle \sigma_{11}(\omega) \rangle \\ \langle \sigma_{22}(\omega) \rangle \\ \langle \sigma_{12}(\omega) \rangle \end{pmatrix} = \begin{pmatrix} C_{11} & C_{12} & C_{16} \\ C_{12} & C_{22} & C_{26} \\ C_{16} & C_{26} & C_{66} \end{pmatrix} \begin{pmatrix} \langle \epsilon_{11}(\omega) \rangle \\ \langle \epsilon_{22}(\omega) \rangle \\ \langle 2\epsilon_{12}(\omega) \rangle \end{pmatrix}, \quad (2.10)$$

where $C_{ij}(\omega)$ are the components of the equivalent stiffness matrix in Voigt notation, and $\langle \epsilon_{ij}(\omega) \rangle$ and $\langle \sigma_{ij}(\omega) \rangle$ represent the volume-averages of the

strain and stress components, respectively. A least-squares procedure is employed to obtain the best-fitting values of C_{ij} using the averaged stress and strain fields obtained from the three tests for each frequency. The resulting P- and S-wave phase velocities are angle- and frequency-dependent, and are given by (Rubino et al., 2016):

$$V_{P,S}(\omega, \theta) = \frac{\omega}{\Re(\tilde{\nu}_{P,S}(\omega, \theta))}, \quad (2.11)$$

where \Re is the real part operator, $\tilde{\nu}_{P,S}(\omega, \theta)$ denotes the complex-valued wavenumbers obtained by solving the elastodynamic equation in a medium defined by the stiffness matrix in equation (2.10). The reader is referred to the works of Rubino et al. (2016) and Favino et al. (2020) for the details of this upscaling procedure. It is important to mention that these upscaling procedures allow us to obtain representative values of the rock physical properties of interest as long as the considered samples constitute an REV of the lithological unit of interest. In the presence of stochastic fracture distributions, identifying subvolumes that fulfill the criteria of an REV tends to be impractical due to the excessively large size of the samples that would be required for this purpose. To overcome this difficulty, we follow the approach of Rubino et al. (2009), who employ the previously outlined upscaling procedure in a Monte Carlo fashion on sub-REV-size samples. For this, we assume that the rock physical properties of the lithological unit of interest are statistically ergodic, and thus, stationary, such that spatial averages can be replaced by ensemble averages inferred through compressibility and shear tests to a multitude of random samples. This approach is equivalent to considering re-

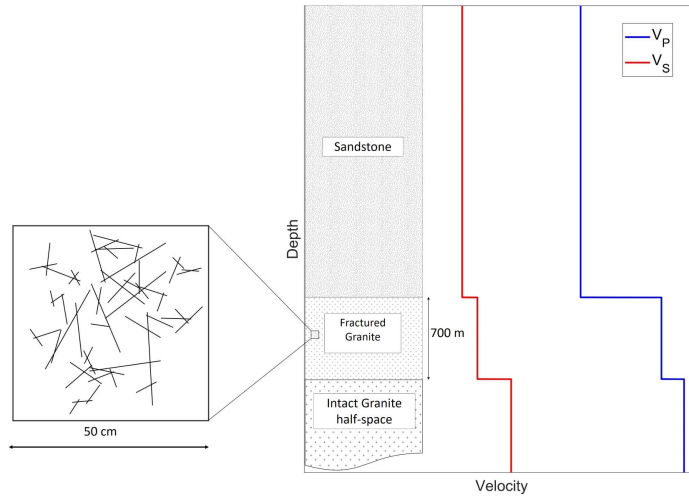


Figure 2.2: Schematic illustration of the canonical 1D model considered in this study showing the lithological column and the associated P- (blue) and S-wave (red) velocity profiles. The blow-up illustrates its detailed structure at the size of the samples considered in our upscaling procedure.

peated applications of the upscaling procedure to randomly chosen samples as a repeated measurement of the rock physical properties of the lithological unit of interest. As such, the representative mechanical properties can then be characterized by the corresponding mean values and variances inferred from a sufficiently large set of such measurements. Finally, please note that, while the velocities computed using the upscaling technique are in general frequency-dependent, in this work, we consider a frequency range in which the resulting velocities have no velocity dispersion.

2.4 Results

2.4.1 Numerical Framework

In order to assess the sensitivity of Rayleigh wave dispersion with regard to the effects of fractures in general and their interconnectivity in particular, we consider a canonical model composed of two horizontal layers overlying a half-space (Figure 2.2). The surficial layer corresponds to a 2500-m-thick sandstone formation, followed by a layer of fractured granite with a thickness of 700 m, and an underlying half-space consisting of intact granite. The sandstone layer is homogeneous and, hence, seismic waves traversing it are not attenuated or dispersed due to FPD effects. Its seismic properties are: $V_P = 3500$ m/s, $V_S = 2000$ m/s, and $\rho = 2500$ kg/m³ (Mavko et al., 1998). For the fractured granite layer, the fractures are represented using highly porous and permeable inclusions. As mentioned above, we assume the statistical stationarity of the properties of the formation, which allows us to carry out the upscaling procedure previously described. This layer is characterized by its fracture density, quantified as the ratio of fracture area over the sample area, the length distribution of fractures, and the number of connections between fractures. These parameters have a significant impact on the resulting body wave velocities of saturated fractured samples (e.g., Hunziker et al., 2018). The underlying granitic half-space has the same material properties as the intact parts of the fractured granitic layer. As the surficial sandstone layer, it is homogeneous and hence devoid of FPD effects. The

P- and S-wave velocities of this layer are computed as $V_P = \sqrt{\frac{K_u + 4/3\mu_m}{\rho_b}}$ and $V_S = \sqrt{\frac{\mu_m}{\rho_b}}$, respectively, where ρ_b is the bulk density of the medium. Note that one could alternatively obtain these velocities applying the upscaling procedure in the homogeneous layer. The physical properties of the granitic rocks and fractures are listed in Table 2.1. The granite properties correspond to those in Detournay and Cheng (1993) and the fracture and fluid properties to those from Rubino et al. (2017). The saturating pore fluid is brine, and the grain-level properties of the fractures are assumed to be consistent with those of the intact granite.

In order to estimate the body wave velocities of the fractured layer, we follow the upscaling procedure described in Section 2.2 employing isotropic rock samples with homogeneously oriented fractures. To explore the role played by the connectivity of the fractures, we consider two end-member-type scenarios: (i) fully connected and (ii) entirely unconnected fracture distributions. When generating a particular synthetic fractured sample, the center positions of the fractures are assigned randomly and fractures not meeting the stipulated connectivity criteria are substituted. This process is repeated until the desired fracture density is obtained and fractures are either fully connected or fully unconnected. To avoid that the substitution process generates preferential orientations of the fractures, the original orientations are retained during substitution. For each connectivity scenario we consider three fracture densities: 0.25%, 0.50%, and 0.75%. These values were chosen based on the feasibility of generating completely connected and

Table 2.1: Properties of intact granitic background rock and embedded fractures.

Property	Background	Fracture
Solid grain density	2700 kg/m ³	2700 kg/m ³
Solid grain bulk modulus	45 GPa	45 GPa
Dry frame shear modulus	19 GPa	0.02 GPa
Dry Frame bulk modulus	35 GPa	0.04 GPa
Permeability	1e-19 m ²	1e-10 m ²
Porosity	0.02	0.8
Fluid viscosity	1e-3 Pa.s	1e-3 Pa.s
Fluid bulk modulus	2.25 GPa	2.25 GPa
Fluid density	1090 kg/m ³	1090 kg/m ³

Note. Embedding background is assumed to correspond to intact granite (Detournay and Cheng, 1993). The pore fluid properties correspond to brine. Fractures are represented as highly compliant, porous, and permeable inclusions, whose grain-level properties correspond to those of the embedding background (Rubino et al., 2017).

unconnected distributions. Finally, we consider two cases of fracture length distributions. We begin with fractures of constant length, in order to isolate the effects of fracture connectivity from those associated with fracture length variation. Later, we repeat the analysis considering a more realistic scenario where fractures have varying lengths governed by a power law distribution, which allows us to assess the impact of effects related to fracture geometry. Recall that, in order to compute effective P- and S-wave velocities for a given fracture density and connectivity, we employ a Monte-Carlo-type approach in combination with the upscaling procedure. The corresponding convergence criterion is based on the stability of the standard deviation (Rubino et al., 2009). The convergence analysis of the Monte Carlo approach is performed for a frequency of 1 Hz, which is typical of Rayleigh waves in passive seismic studies and is located within the non-dispersive plateau illustrated in Figure 2.1. As mentioned before, the fact that the frequencies of interest for Rayleigh wave monitoring fall within the non-dispersive plateau allows us to employ a purely elastic modelling of Rayleigh wave dispersion.

2.4.2 Constant Length Fracture Distributions

In the following, we consider square samples with a side length of 50 cm drawn from the fractured granite formation (Figure 2.2). The fractures are represented as rectangular poroelastic features with an aperture of 0.4 mm and a length of 12 cm. We analyze the seismic response for fracture densities of 0.25%, 0.50%, and 0.75% for two end-member-type connectivities:

(i) connected case, where all fractures have at least one connection with another fracture; (ii) unconnected case, where the fractures do not have any connections with each other. A single realization from each set of samples is illustrated in Figure 2.3.

Recall that we infer effective body wave velocities for each fracture density and connectivity using a Monte Carlo approach. Figure 2.4 shows the results of the standard deviations as functions of the number of realizations for a frequency of 1 Hz, which is representative of Rayleigh wave studies and located within the non-dispersive plateau. We find that after 50 realizations, the standard deviations have stabilized and, thus, the average of the velocities of each sample set can be considered as being representative of the effective velocities of the corresponding fractured layers (Rubino et al., 2009).

Figure 2.5 shows the resulting effective P- and S-wave velocities as functions of frequency for the scenarios illustrated in Figure 2.3. In general, both P- and S-wave velocities decrease with increasing fracture densities. However, we observe that, when considering a constant fracture density, velocities for the unconnected case tend to be higher than those for the connected case. This velocity drop in presence of connected fractures, which is particularly prominent for frequencies around 1Hz, is due to FPD effects (Rubino et al., 2014, 2017). To reconcile this, it is important to account for the fact that, for such frequencies, there is not enough time in a half wave cycle to allow for hydraulic communication between fractures and background and, thus, fractures behave as hydraulically sealed. Therefore, in presence of unconnected

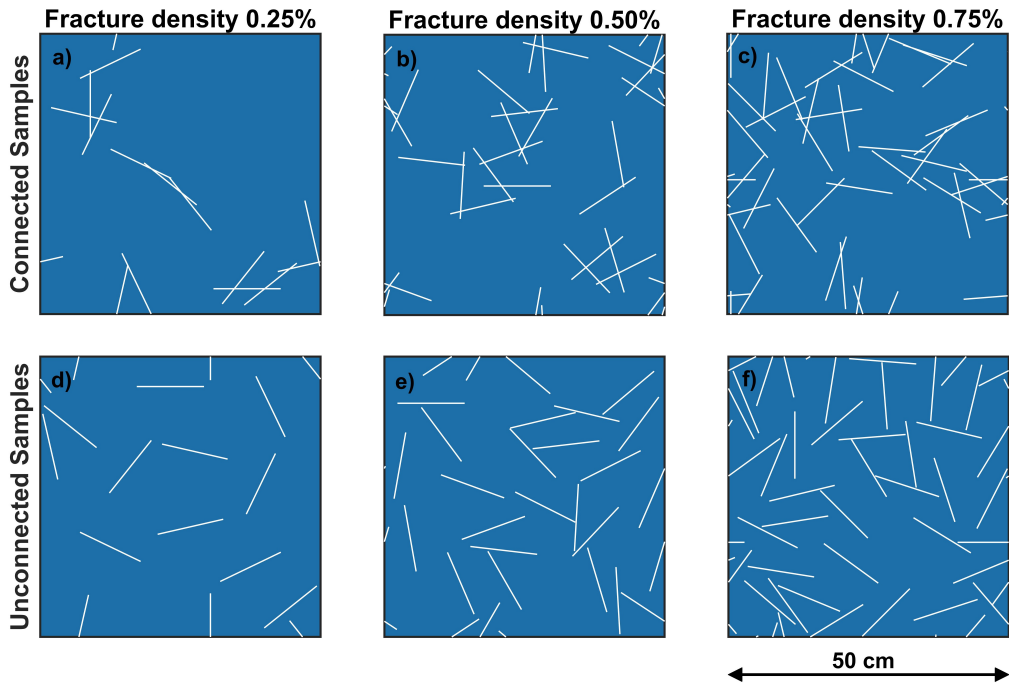


Figure 2.3: Examples of fracture distributions employed to derive effective body wave velocities of the fractured layer (Figure 2.2). We consider representative samples comprising (a, b, c) connected and (d, e, f) unconnected fracture distributions. Each column depicts a different fracture density: (a, d) 0.25%, (b, e) 0.50% and (c, f) 0.75%. The side length of the samples is 50 cm, and fractures are rectangular poroelastic features with a length of 12 cm and a width of 0.4 mm.

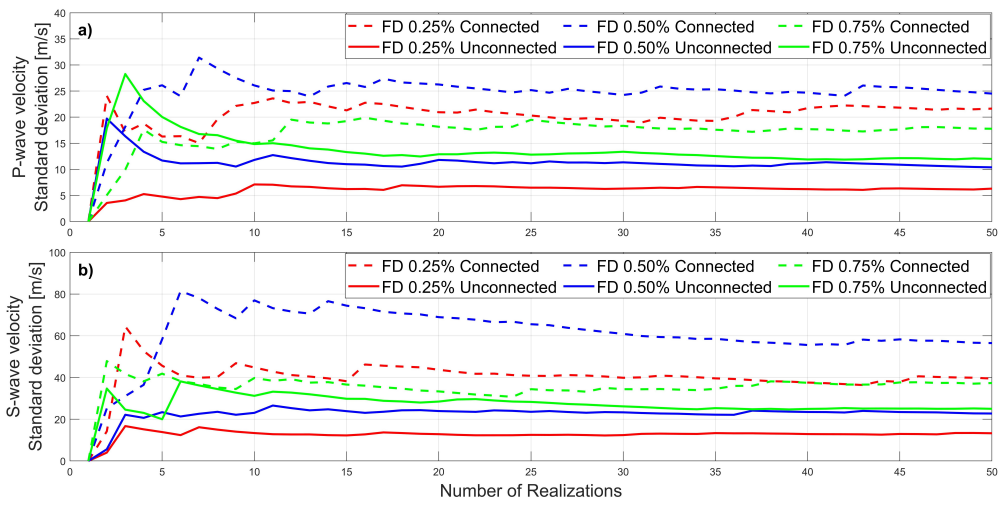


Figure 2.4: Standard deviations of (a) P- and (b) S-waves at 1 Hz as functions of the number of realizations for connected (dashed lines) and unconnected (solid lines) samples of constant fracture length and fracture densities of 0.25%, 0.50%, and 0.75%.

fractures, there is a significant pressure buildup in the fluid contained in the fractures in response to the passage of seismic waves, which in turn, opposes the deformation. Conversely, in the presence of connected fractures, there is enough time for the fluid pressure within connected fractures to equilibrate, the stiffening effect of the fracture fluid is correspondingly diminished and, hence, the medium behaves as if it was softer, which manifests itself in the form of the observed velocity drop (Figure 2.5). It is interesting to observe in Figure 2.5 that the body wave velocity drop is more significant for the case of S-waves than for the P-waves. The reason for this is that, in the case of P-waves, regardless of the orientation, the fluid contained in a given fracture will experience a pressure increase in response to the associated compression. Conversely, in the case of S-waves, the associated deformation of the fractures increases the fluid pressure in some fractures and diminishes it in others, depending on their orientation with respect to the direction of propagation of the seismic perturbation (Rubino et al., 2017). This particularity, in turn, implies that in the presence of connected fractures, the local fluid pressure gradients may be significantly higher for S-waves than for P-waves. Consequently, the associated reduction of stiffening effects and, thus, the magnitude of the associated velocity drop is much more significant in the case of S-waves (Figure 2.5). These effects are accounted for in the model within the framework of poroelasticity.

It is, however, important to remark that, for the range of frequencies usually employed for passive seismic surveys ($\sim 0.1 - 10$ Hz) , dispersion

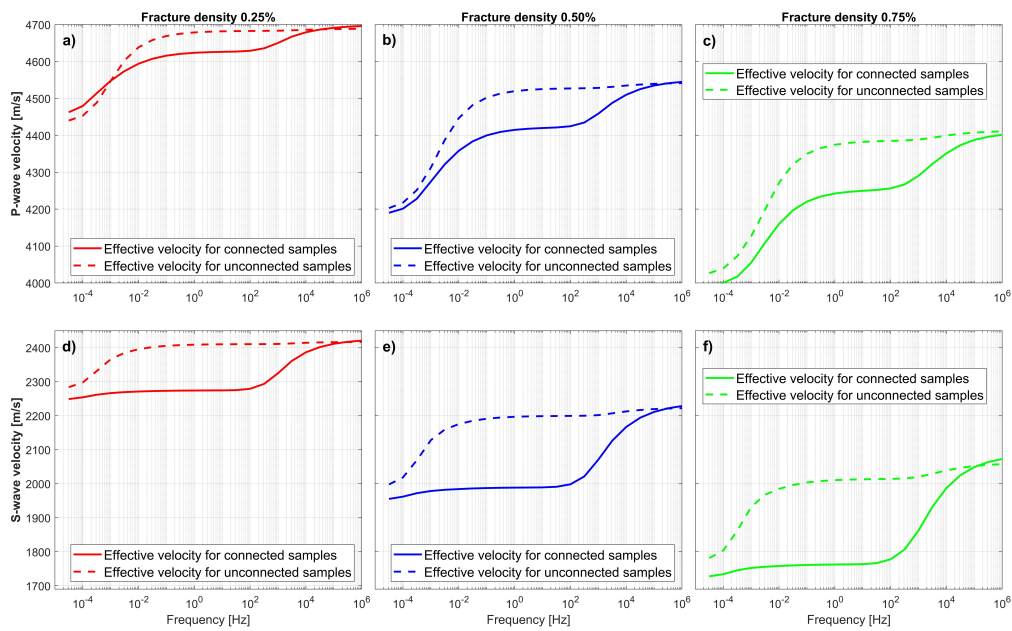


Figure 2.5: (a, b, c) Effective P- and (d, e, f) S-wave velocities inferred through a Monte Carlo approach for connected (solid lines) and unconnected (dashed lines) fractures of constant length and fracture densities of 0.25%, 0.50%, and 0.75%.

in the resulting effective velocities is almost non-existent (Figure 2.5). We have verified that the residual P-wave dispersion in the considered frequency range has no noticeable effect on the simulations we performed. This allows, in turn, for the use of the upscaled effective body wave velocities to compute Rayleigh wave velocity dispersion curves employing an elastic model (Section 2.2). Table 2.2 summarizes the corresponding velocity values (Figure 2.5) which we consider in the following to study Rayleigh wave characteristics.

The Rayleigh phase and group velocities obtained for the canonical model are shown in Figure 2.2 and the different characteristics for the fracture network, summarized in Table 2.2, are shown in Figure 2.6. In general, there is a distinct phase velocity behaviour for all scenarios considered (Figures 2.6a to 2.6c). This is due to the fact that different frequencies are sensitive to different depths of investigation, with low frequencies being dominated by the properties of intact granite and high frequencies by those of sandstone. Sensitivity to the fractured granite layer prevails for frequencies between ~ 0.1 Hz and ~ 1 Hz. We note that differences between the Rayleigh wave phase velocities associated with the connected and unconnected cases increase with fracture density, which is expected from the body wave velocity results (Figure 2.5). We quantify the relative velocity variation, computed as the ratio between the differences and the average of the connected and unconnected case for each frequency (black dashed line in Figures 2.6 a to f). The peak of the relative difference curve for phase velocities occurs around 0.3 Hz, with values of 1%, 1.8%, and 2.7% for fracture densities of 0.25%, 0.50%,

Table 2.2: Layer thicknesses and seismic properties of the considered model (Figure 2.2).

Lithology	Thickness [m]	V_P [m/s]	V_S [m/s]	ρ_b [kg/m ³]
Sandstone	2500	3500	2000	2500
Fractured granite	700	See Below	See Below	See Below
Intact granite	Infinite	4810	2620	2700

Properties of the fractured granite layer: constant length fracture distributions

Fracture density	Connectivity	V_P [m/s]	V_S [m/s]	ρ_b [kg/m ³]
0.25%	Connected	4623	2274	2694
0.25%	Unconnected	4679	2409	2694
0.50%	Connected	4415	1989	2690
0.50%	Unconnected	4520	2197	2690
0.75%	Connected	4242	1762	2687
0.75%	Unconnected	4374	2011	2687

Note. The properties corresponding to the fractured granite layer are depicted in the lower half of the table and result from taking the velocities corresponding to the non-dispersive plateau (Figure 2.5).

and 0.75%, respectively. Rayleigh wave group velocities (Figures 2.6 d to f) exhibit similar characteristics as the phase velocities. For intermediate frequencies, where the curves are sensitive to the fractured granite layer, we note that the relative differences for the group velocities are twice of the phase velocities, with a peak located near 0.25 Hz and a notch near 0.3 Hz. Peak relative difference values between the connected and unconnected cases are 2%, 3.8%, and 5.5% for fracture densities of 0.25%, 0.50% and 0.75%, respectively. These results indicate that, for the considered scenarios and for constant fracture lengths, both phase and group Rayleigh wave velocities are highly sensitive to changes in the fracture connectivity.

2.4.3 Stochastic Distribution of Fracture Lengths

As seen above, fracture connectivity greatly influences Rayleigh wave dispersion characteristics when the fracture lengths are constant. In the following, we consider a more realistic scenario based on a stochastic distribution of fracture lengths. Following pertinent previous works on this topic (e.g., de Dreuzy et al., 2001; Bonnet et al., 2001; Hunziker et al., 2018), we use a power law of the form

$$n(L) = f_d(a - 1) \frac{L^{-a}}{L_{min}^{1-a}}; L \in [L_{min}, L_{max}], \quad (2.12)$$

where L is the fracture length, $n(L)$ is the number of fractures in the considered sample with a length comprised between L and $L + dL$, f_d is the fracture density, a is the characteristic exponent of the fracture size distribution, and L_{min} and L_{max} are the bounding minimum and maximum values

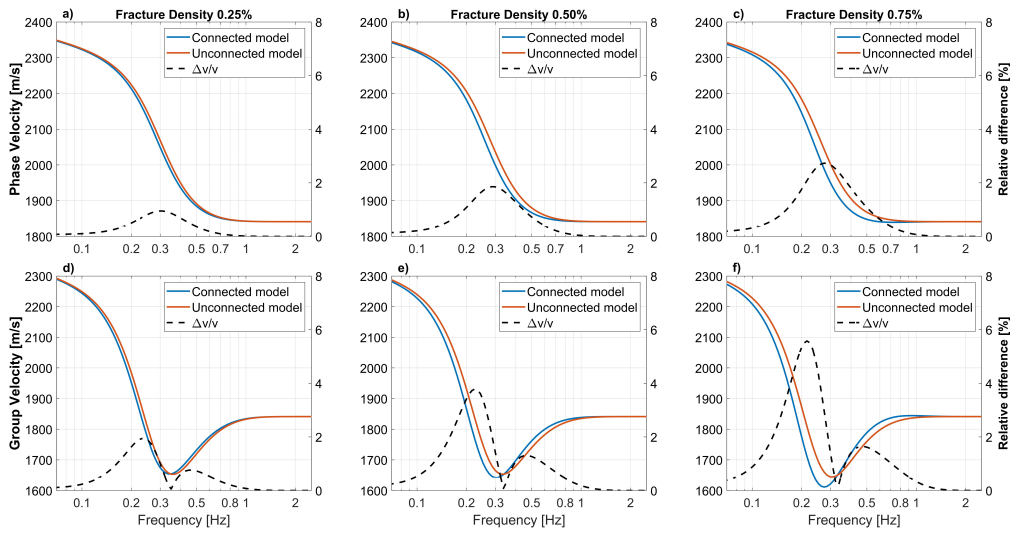


Figure 2.6: (a, b, c) Rayleigh wave phase and (d, e, f) group velocities for the connected (blue solid lines) and unconnected (orange solid lines) scenarios for different fracture densities. Given the small value of the absolute differences, we also illustrate relative velocity differences (dashed black lines) with scales depicted on the right-hand side of the corresponding plots. The latter are computed as the ratio between the differences and the average of the connected and unconnected case for each frequency.

of the distribution, respectively. While earlier works (e.g., de Dreuzy et al., 2001) consider fracture density as the number of fracture centers per area, Hunziker et al. (2018) defines it as the ratio of the fracture area over the total area of the studied medium. This allows to distinguish between the effects associated with changes of fracture volume and fracture length. The exponent a can take values between 1.5 and 3 and controls the prevalence of shorter to longer fractures within the limits given by L_{min} and L_{max} . For this work, we choose L_{min} and L_{max} as 4 cm and 25 cm, respectively. Together with a fixed aperture of 0.4 mm, results in fracture aspect ratios between 100 and 625, which is in agreement with corresponding observations of Vermilye and Scholz (1995) for real fractures. For the exponent a , we choose an intermediate value of 2.25, which implies that there is no predominance of neither shorter nor longer fractures on the seismic response of the medium (Hunziker et al., 2018).

The considered samples are generated in the same way as those characterized by constant length fractures and we employ the same physical properties for the fractures and background given in Table 2.1. Again, we consider three different fracture densities: 0.25%, 0.50%, and 0.75%, and two end-member-type connectivity scenarios of fully connected and fully unconnected fractures. Figure 2.7 illustrates some examples of the fracture distribution realizations considered in this section. We again employ the upscaling procedure described in section 2.2 in combination with a Monte Carlo approach to obtain the effective mechanical properties of the fractured formation. Al-

though not shown here for brevity, we found that 50 samples are sufficient to obtain a stable standard deviation and, thus, representative body wave velocities.

The results for the effective P- and S-body wave velocities as functions of frequency are shown in Figure 2.8. The characteristics of the velocity dispersion curves are similar to those for the constant fracture length scenario (Figures 2.5 and 2.8). Each fracture density shows the manifestations of FPD effects described in section 2.2, with a constant velocity plateau for the frequencies of interest between ~ 0.01 and ~ 3 Hz. We note that velocities for P-waves (Figures 2.8a to 2.8c) and S-waves (Figures 2.8d to 2.8f) decrease for increasing fracture density. As observed previously the difference in body wave velocities between connected and unconnected fracture distributions increases for larger fracture densities and is more prominent for S-waves than for P-waves. This indicates that, regardless of the fracture length distribution, velocity variations associated with changes in fracture connectivity are strongly affected by the fracture density. The resulting effective velocities for each scenario are listed in Table 2.3.

Figure 2.9 illustrates the Rayleigh wave velocity dispersion for the variable fracture length case. Phase and group velocities present limiting values at high and low frequencies corresponding to the values of sandstone and intact granite, respectively. Sensitivity to the fractured layer prevails at frequencies between ~ 0.1 Hz and ~ 1 Hz. For Rayleigh wave phase velocities (Figures 2.9a to 2.9c), the maximum of the relative difference between connected

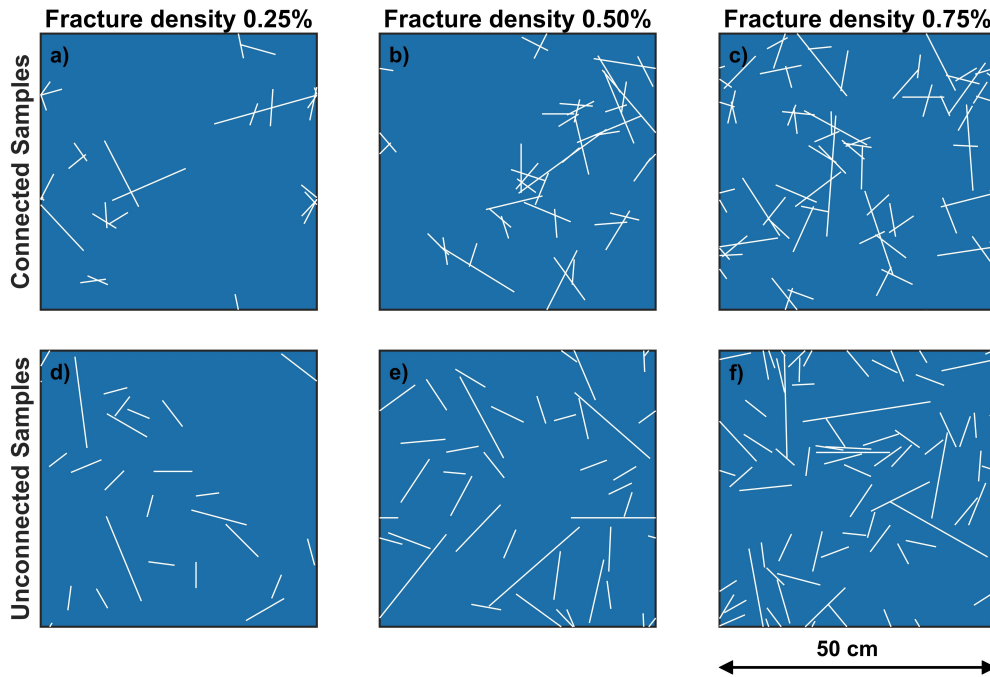


Figure 2.7: Examples of the variable length fracture distributions employed to derive the effective body wave velocities of fractured granite. We consider representative samples comprising (a, b, c) connected and (d, e, f) unconnected fractures. Each column depicts a different fracture density: (a, d) 0.25%, (b, e) 0.50%, and (c, f) 0.75%. Samples have a 50 cm side length. Fractures are rectangular features with a constant aperture of 0.4 mm and length drawn from a power law distribution (Equation 2.12).

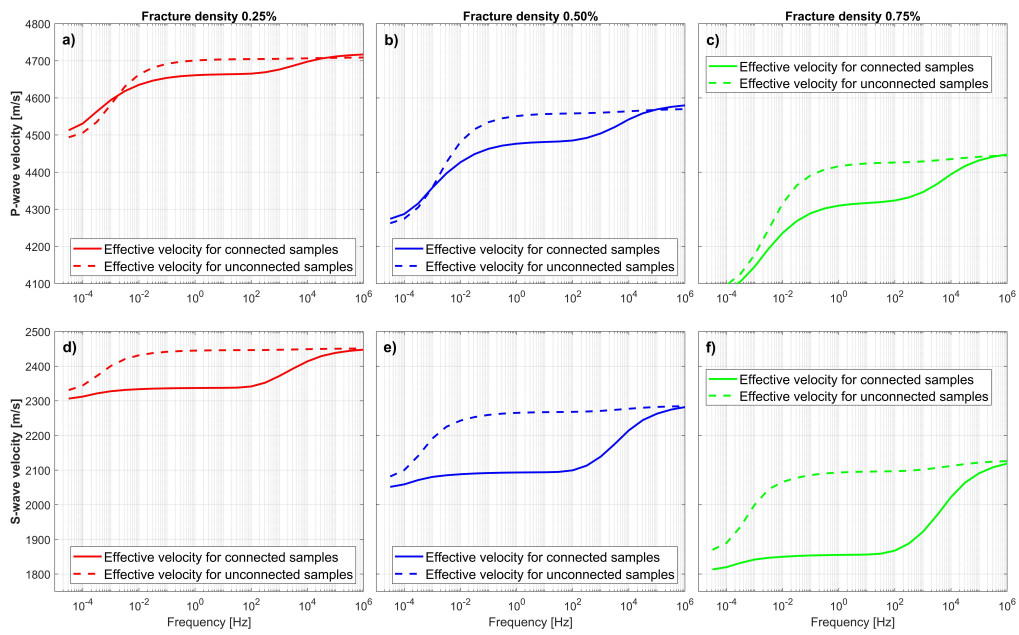


Figure 2.8: (a, b, c) Effective P- and (d, e, f) S-wave velocities for connected (solid lines) and unconnected (dashed lines) fractures of variable lengths (Figure 2.7). We illustrate the results for fracture densities of 0.25%, 0.50%, and 0.75%. The curves are obtained by averaging the responses of 50 fracture network realizations.

Table 2.3: Properties of the fractured granite layer: Variable length fractures distributions

Fracture density	Connectivity	V_P [m/s]	V_S [m/s]	ρ_b [kg/m ³]
0.25%	Connected	4661	2337	2694
0.25%	Unconnected	4701	2445	2694
0.50%	Connected	4477	2093	2690
0.50%	Unconnected	4551	2265	2690
0.75%	Connected	4310	1855	2687
0.75%	Unconnected	4416	2093	2687

Note. Characteristics of the fractured layer schematically illustrated in Figure 2.2 used for computing Rayleigh wave dispersion curves.

and unconnected cases occurs near 0.3 Hz with values of 0.7%, 1.4%, and 2.3% for fracture densities of 0.25%, 0.50%, and 0.75%, respectively. For Rayleigh wave group velocities, maximum relative differences occur for a frequency close to 0.25 Hz with values of 1.5%, 2.9%, and 4.8% for fracture densities of 0.25%, 0.50%, and 0.75%, respectively. A comparison of Rayleigh wave velocities for the variable length case with the corresponding results obtained for the constant length fracture distributions show that the relative differences for the latter case are approximately 25% higher. However, the relative effect of changing fracture density or connectivity is the same for both variable and constant length fracture distributions. This implies that for the fracture length variations considered in this work, the controlling factors regarding FPD effects on Rayleigh waves are the fracture density and fracture connectivity rather than the length distribution of the fractures.

In order to obtain a clearer idea on the impact of FPD effects on Rayleigh wave dispersion, we repeat the analysis for additional values of fracture density ranging between 0.25% and 0.90% (Figure 2.10). Figures 2.10a and 2.10b show the results of the effective body wave velocities for a frequency of 1 Hz, which is representative of the non-dispersive plateau (dashed lines). In addition to the connected and unconnected scenarios, we also consider samples which have not been subjected to the previously outlined control of connectivity and, hence, have not undergone any fracture substitution. We refer to this case as randomly connected. As the end-member-type cases of fully connected and fully unconnected distributions are not likely to occur in real

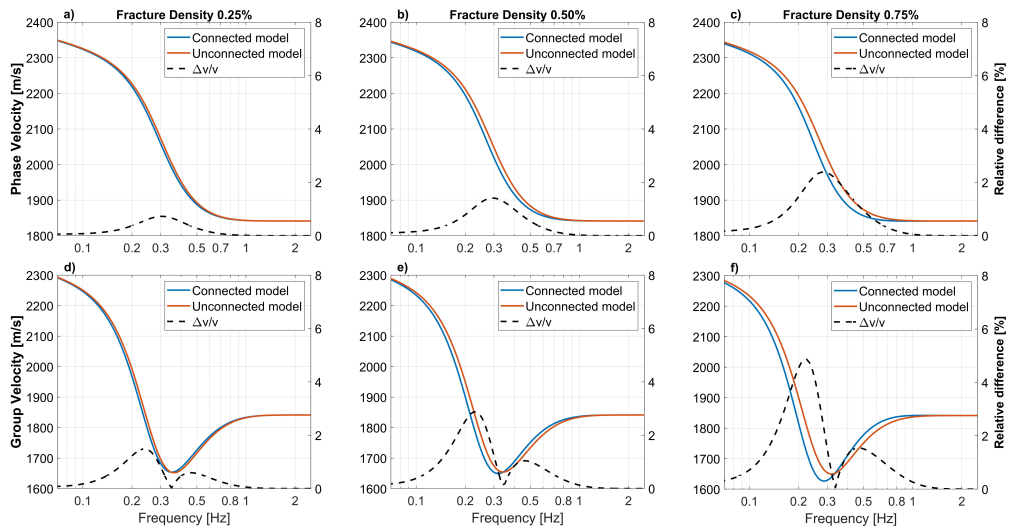


Figure 2.9: (a, b, c) Rayleigh wave phase and (d, e, f), group velocities for connected (blue solid lines) and unconnected (orange solid lines) fractures whose length distribution obey the power law given in Equation 2.12 (Figure 2.7). Dashed black lines indicate the relative velocity difference, computed as the ratio between the differences and the average of the connected and unconnected case for each frequency.

formations, the randomly connected scenario is expected to be more representative of the naturally-occurring degree of connectivity for a given fracture density. We again observe a clear trend of decreasing P- and S-wave velocities with increasing fracture density (Figures 2.10a and 2.10b). In particular, we observe that for a given fracture density, connected fracture distributions have the lowest velocities, unconnected fracture distributions have the highest velocities, and randomly connected fracture distributions (red dashed lines) have intermediate velocities. The velocities of the randomly connected fracture distributions are closer to those of the unconnected fracture distributions for lower fracture densities and closer to those of connected fracture network for higher fracture densities. This is expected as the probability of interconnections increases with the fracture density.

Figures 2.10a and 2.10b also show the velocities in the high-frequency or no-flow limit at 10^6 Hz, which corresponds to the elastic behaviour of the samples (solid lines). We observe that, while the trend of decreasing velocity with increasing fracture density is still present, the effect of fracture connectivity is largely negligible. This is consistent with works based on elastic approximations of fractured media (e.g., Grechka and Kachanov, 2006), where FPD effects are neglected and, thus, suggest that fracture connectivity has no impact on the mechanical properties. Interestingly, P- and S-wave velocities for the randomly connected case considering FPD effects (red dashed lines) decreases more drastically with the fracture density than the corresponding high frequency estimates (red solid lines). Figures 2.10c

and 2.10d show the maximum relative Rayleigh wave velocity difference between connected and unconnected fractures for a given fracture density in the presence and absence of FPD. For the cases considering FPD effects, this corresponds to the analysis shown in Figure 2.9 extended for additional fracture densities. For the cases disregarding FPD effects, the relative difference corresponds to velocities in the high-frequency no-flow limit (10^6 Hz). Figure 2.10c corresponds to the maximum relative difference between connected and unconnected fracture distributions for Rayleigh wave group velocity, at a frequency of ~ 0.2 Hz, and Figure 2.10d shows the maximum relative difference for Rayleigh wave phase velocity, at a frequency of ~ 0.3 Hz. We note that, when considering FPD effects, the difference between connected and unconnected cases is already significant for lower fracture densities and increases progressively with increasing fracture density. Conversely, in the absence of FPD effects, the difference between the connected and unconnected cases remains largely negligible for all fracture densities considered. Overall, these results suggest that disregarding FPD effects in a velocity analysis, that is, considering the high frequency elastic representation, may lead to an overestimation of the fracture density changes required to explain a given velocity change.

Finally, we consider variations in the thickness and the depth of the fractured granite layer in our canonical model (Figure 2.2, Table 2.2) in order to assess whether and to what extent such changes affect the sensitivity to variations in fracture connectivity. Figure 2.11 shows the effects of varying

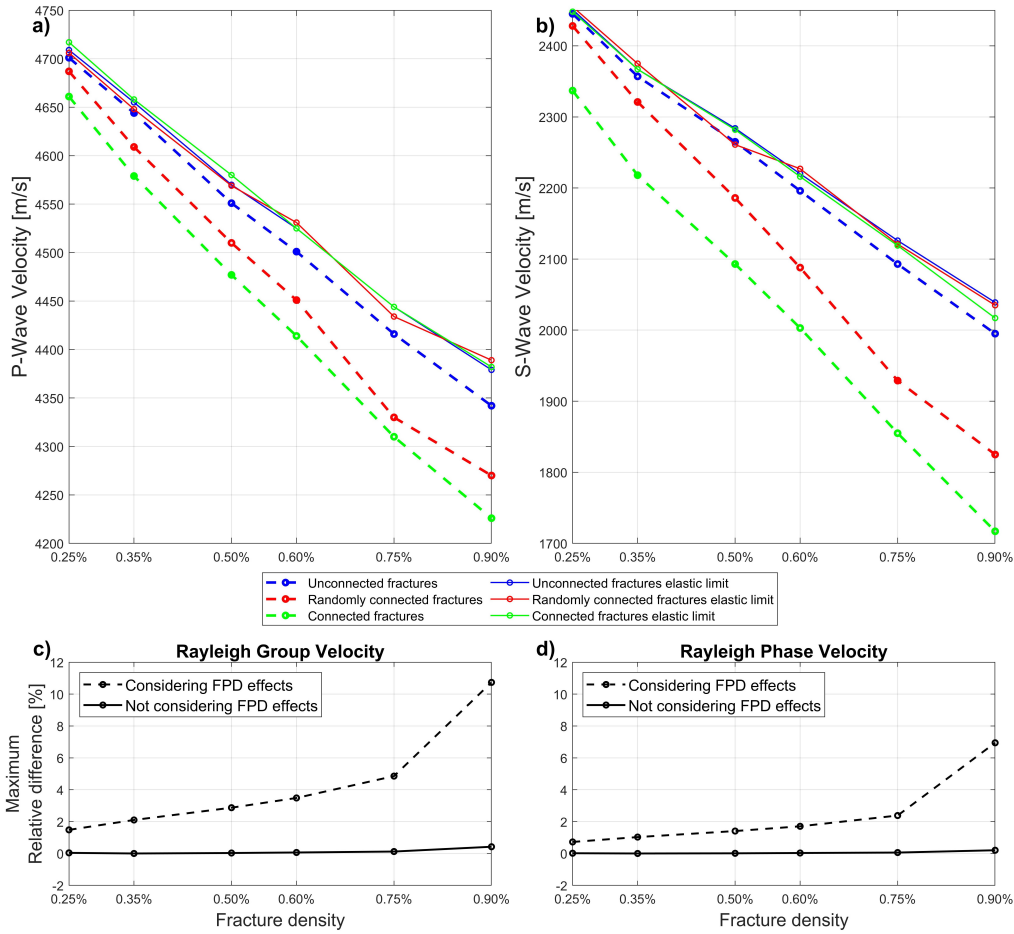


Figure 2.10: (a) Effective P- and (b) S-wave velocities as functions of fracture density for different degrees of fracture connectivity considering a stochastic distribution of the fracture lengths (Equation 2.12, Figure 2.7). Dashed lines correspond to a frequency of 1 Hz, which is representative for passive seismic studies, while solid lines are computed using a frequency of 10^6 Hz, thus resulting in elastic behaviour of the probed samples. Maximum relative difference for (c) Rayleigh wave group and (d) phase velocities between the connected and unconnected distributions computed for the elastic and poroelastic scenarios.

the depth and thickness of the fractured layer for a fracture density of 0.50% (Table 2.3). Figures 2.11a and 2.11d document the Rayleigh wave phase and group velocities after increasing the thickness of the surficial sandstone layer from 2500 m to 3500 m, while keeping the thickness of the fractured layer unchanged. Figures 2.11b and 2.11e show the results for reference model without modifications. For a deeper location of the fractured layer (Figures 2.11a and 2.11d), we observe that the maximum relative differences between the connected and unconnected cases shift towards lower frequencies, as longer wavelengths are sensitive to greater depths. We also see that the magnitude of the relative difference decreases, as the increase of the thickness of the overlaying formation diminishes the impact of the reservoir on the Rayleigh wave dispersion. Figures 2.11c and 2.11f show the results after reducing the thickness of the fractured layer from 700 m to 350 m. We observe no appreciable frequency shift but there is, as expected, an important decrease of the relative differences, which, nevertheless, remain relevant when compared to corresponding field evidence (e.g., Obermann et al., 2015; Taira et al., 2018).

2.5 Discussion

We employed a numerical upscaling procedure based on the assumption of quasi-static poroelasticity, which does not account for inertial effects to obtain the effective body wave velocities of fractured samples. The transition frequency, at which inertial effects become relevant, depends on the material properties. For all scenarios of practical interest in the given context, this

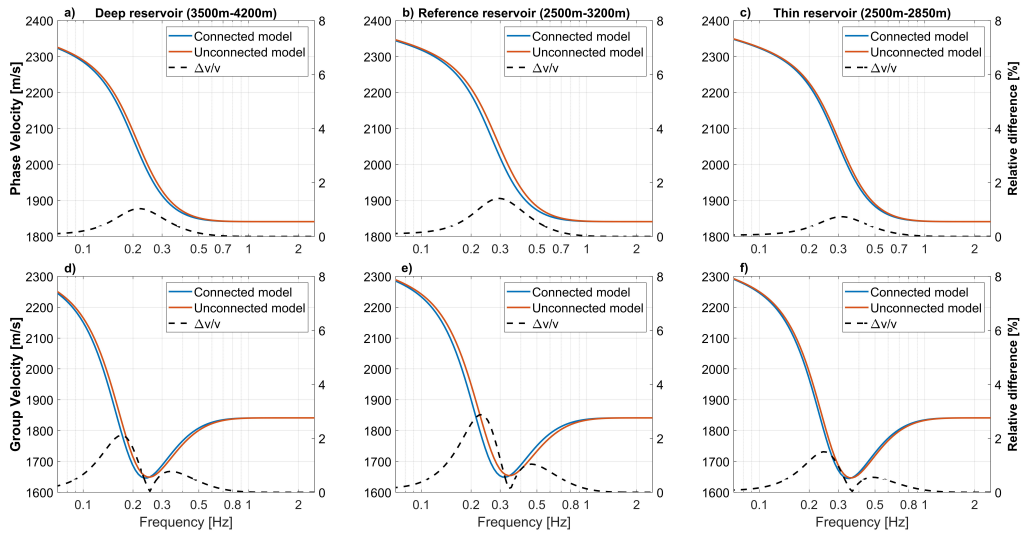


Figure 2.11: Effects of variations in the depth and thickness of the fractured layer in our canonical model (Figure 2.2, Table 2.2) for a fracture density of 0.50% and considering a stochastic distribution of lengths (Equation 2.12, Figure 2.7). (b, e) Phase and group velocities for the reference case (Table 2.3). Phase and group velocities (a, d) when the fractured layer is located 1000 m deeper and (c, f) for fractured layer with a thickness of 350 m as compared to one of 700 m used for the reference model.

frequency is much higher than the frequency range used in passive seismic exploration in general and Rayleigh wave studies in particular and, hence, the poroelastic upscaling procedure used in this study is valid as long as fracture sizes remain much smaller than the predominant wavelength.

The observed fracture connectivity effects on Rayleigh wave velocities are significantly higher than the velocity variations reported from passive seismic monitoring of geothermal sites (Obermann et al., 2015; Taira et al., 2018). This is likely due to the fact that in a natural environment, changes of fracture connectivity are likely to be small and gradual, while we are considering the end-member scenarios of entirely unconnected and connected fracture networks. Moreover, 2D simulations tend to overestimate FPD effects on the seismic response of the samples (Hunziker et al., 2018). Another point of discrepancy may be the thickness of the fractured reservoir of our model, as natural and enhanced fractured reservoirs are likely to be thinner than 700 m. In addition, to compute Rayleigh wave dispersion curves, we adopted a model consisting of isotropic and homogeneous layers. It is known that in the case of fractures with preferential orientations, FPD effects have significant impact on the velocity anisotropy of the probed samples (Rubino et al., 2017). The corresponding effects in surface wave dispersion, in addition to more complex model geometries including lateral variations of the material properties and layer thicknesses should be addressed in future works.

We also considered distributions of fractures with constant aperture and material properties, and while the resulting aspect ratio distribution of the

fractures is realistic (e.g., Vermilye and Scholz, 1995), the length variation ranges and sample sizes are governed by computational constraints. This raises the question regarding the scalability and relevance of our results for realistic fractures, which can be several orders-of-magnitude larger than the ones considered in our samples. Following the work of Guo et al. (2017), which considers fracture networks composed by two sets of orthogonal equal fractures, the characteristic frequency of FB-FPD, F_{fb} , can be expressed as

$$F_{fb} = \frac{8D_b}{a_f^2}, \quad (2.13)$$

where a_f denotes the length of the fractures and D_b the diffusivity of the background medium. D_b is expressed as

$$D_b = \frac{M_b L_b \kappa_b}{\eta L_b^{sat}}, \quad (2.14)$$

where M_b corresponds to the inverse of the fluid storage coefficient of the background material, L_b and L_b^{sat} are the P-wave moduli for the dry and saturated cases, respectively, κ_b is the permeability and η is the fluid viscosity. As background properties are not affected by changes in fracture size, F_{fb} is expected to decrease for increasing fracture size (Equation 2.13). On the other hand, the characteristic frequency of FF-FPD effects, F_{ff} , corresponding to the maximum attenuation and dispersion due to this process, is given by (Guo et al., 2017)

$$F_{ff} = \frac{8D_e}{a_f^2}, \quad (2.15)$$

where D_e denotes the diffusivity of an effective medium, which considers the fractures as the pore space and the background as the solid phase. D_e is

expressed as

$$D_e = \frac{M_e L_e \kappa_{fr} f_d}{\eta L_e^{sat}}, \quad (2.16)$$

where M_e corresponds to the inverse of the effective medium fluid storage coefficient, L_e and L_e^{sat} are the P-wave moduli for the dry and saturated effective medium, respectively, κ_{fr} is the permeability of the fractures and f_d is the fracture density. As can be seen in Equations 2.15 and 2.16, F_{ff} depends on the effective medium diffusivity and the fracture size. Neglecting possible changes in elastic properties of the fractures and considering that an increase in fracture length is associated with an increase in aperture (e.g., Vermilye and Scholz, 1995) and, therefore, in permeability (e.g., Brown, 1987), it can be shown that the impact of fracture size on F_{ff} tends to be counteracted by the associated increase in permeability. For this reason, we expect that the FF-FPD characteristic frequency will not be significantly affected by the scale of the fractures. This, together with the fact that F_{fb} decreases with increasing fracture size implies that the frequencies typically employed in ambient seismic noise studies are likely to remain in the non-dispersive plateau. This, in turn, suggests that the effects of connectivity are expected to remain significant regardless of the scale of the fractures considered. However, further work is required in this direction to assess associated scaling characteristics for complex fracture distributions and possible fracture compliance changes with scale. This would allow to evaluate the corresponding impact not only on the characteristic frequencies but also on the magnitude of the fracture connectivity effects.

2.6 Conclusions

We have employed a numerical upscaling procedure together with a Monte Carlo approach to obtain effective body wave velocities of a fractured formation. This approach allows to account for FPD effects between fractures and their embedding background as well as between connected fractures. For the frequency range typical of ambient seismic noise analysis, we have found that there is no body wave velocity dispersion or attenuation due to FPD effects for our models. However, the presence of interconnections between fractures produces a significant drop of the body wave velocities in comparison with the corresponding unconnected scenario. This is an important poroelastic phenomenon, which is generally referred to as pore fluid softening/stiffening and which cannot be explained from a purely elastic perspective. The effective body wave velocities we obtained were employed to determine the effects of fracture connectivity on Rayleigh wave phase and group velocities. Based on the prevailing elastic models, changes in Rayleigh velocities in fractured environments were so far largely attributed to changes in fracture density or aperture. Our results indicate that fracture connectivity plays an important role in the seismic response of fractured formations due to FPD effects and that these effects are appreciable when performing Rayleigh wave dispersion analysis.

We compared the results from distributions with constant fracture lengths and fracture lengths drawn from a power law distribution. We found that, for the range of length variations employed, fracture length distribution seems

to be of subordinate importance with respect to changes in connectivity or fracture density. Our results demonstrate the importance of FPD effects for Rayleigh waves in fractured media, and notably, that neglecting FPD effects between connected fractures may lead to an overestimation of fracture density.

2.7 Acknowledgments

The data set used to plot the Figures presented in this paper can be downloaded from <https://doi.org/10.5281/zenodo.4788646>. This work is supported by grant number 200020-178946 from the Swiss National Science Foundation and was in part completed within the Swiss Competence Center on Energy Research - Supply of Electricity, with the support of Innosuisse. J. G. R. gratefully acknowledges the financial support received from the Agencia Nacional de Promoción Científica y Tecnológica of Argentina (PICT 2017-2976).

Chapter 3

Seismic Signatures of Partial Steam Saturation in Fractured Geothermal Reservoirs: Insights From Poroelasticity

Gabriel E. Quiroga¹, J. Germán Rubino², Santiago G. Solazzi¹, Nicolás D.

Barbosa¹, Marco Favino¹, and Klaus Holliger¹

¹ Institute of Earth Sciences, University of Lausanne, Lausanne,
Switzerland.

² CONICET, Centro Atómico Bariloche - CNEA, San Carlos de Bariloche,
Argentina.

Published as: Quiroga, G. E., Rubino, J. G., Solazzi, S. G., Barbosa, N. D., Favino, M., and Holliger, K. (2023). Seismic signatures of partial steam saturation in fractured geothermal reservoirs: insights from poroelasticity. *Geophysics*, 88(5), 1-68.

3.1 Abstract

Detecting the presence of gaseous formation fluids, estimating the respective volumes, and characterizing their spatial distribution is important for a wide range of applications, notably for geothermal energy production. The ability to obtain such information from remote geophysical measurements constitutes a fundamental challenge, which needs to be overcome to address a wide range of problems, such as the estimation of the reservoir temperature and pressure conditions. With these motivations, we compute the body wave velocities of a fractured granitic geothermal reservoir formation with varying quantities of steam to analyze the seismic signatures in a partial saturation context. We employ a poroelastic upscaling approach that accounts for mesoscale fluid pressure diffusion (FPD) effects induced by the seismic strain field, and, thus, describes the governing physical processes more accurately than standard representations. Changes in seismic velocities due to steam saturation are compared with changes associated with fracture density variations, as both are plausible results of pressure changes in geothermal reservoirs. We find that steam saturation has a significant impact on P-wave velocities while affecting S-wave velocities to a significantly lesser

extent. This contrasting behavior allows to discriminate between fracture density and steam saturation changes by means of P- and S-wave velocity ratio analyses. To evaluate the potential of seismic methods to provide this information, a canonical geothermal reservoir model is employed to compute Rayleigh wave velocity dispersion and seismic reflection amplitude vs angle (AVA) curves. These studies reveal that AVA analyses allow to differentiate changes in fracture density from changes in steam saturation. We also note that Rayleigh-wave-based techniques are much less sensitive to steam content changes than to fracture density changes. Comparisons with elastic approaches show that including FPD effects through the use of a poroelastic model is crucial for the reliable detection and characterization of steam in fractured geothermal reservoirs.

3.2 Introduction

The remote detection and characterization of the presence of gaseous phases in fractured geological formations is essential for numerous applications of economic and environmental importance, such as, for example, the monitoring of CO₂ sequestration projects or the identification of gas pockets in hydrocarbon reservoirs (e.g., Fatti et al., 1994; Kazemeini et al., 2010; Roach et al., 2015; Stork et al., 2018). In particular, the detection of the presence or absence of steam in high-enthalpy geothermal reservoirs can provide unique insights with regard to the system's temperature and pressure conditions (e.g., Scott, 2020). Most high-enthalpy geothermal reservoirs are associated

with fractured environments. Open fractures are weak and permeable features that tend to constitute preferential pathways for fluid flow and, thus, greatly affect the overall hydraulic and mechanical properties of the medium. Correspondingly, seismic methods are extensively used for the characterization and monitoring of geothermal projects (e.g., Gunasekera et al., 2003; Obermann et al., 2015; Taira et al., 2018; Sánchez-Pastor et al., 2021; Toledo et al., 2022).

Fractures prevail over a wide range of scales (e.g., Vermilye and Scholz, 1995; Bonnet et al., 2001), from the regional scale all the way to the microscopic one. Seismic waves travelling through fractured media tend to experience an increase in attenuation, dispersion, and scattering as well as a general decrease in the overall propagation velocity. The relative scale of the fractures with respect to the prevailing seismic wavelengths determines which physical mechanisms dominate. Mesoscale fractures, which are the focus of this study, are much smaller than the prevailing wavelengths, but much larger than the pore scale. Fractures in this scale range do not promote significant scattering and are well below the explicit resolution of seismic exploration techniques, but they do manifest themselves through pronounced increases of attenuation and dispersion. Given the seemingly universal hyperbolic distribution of fracture lengths (e.g., de Dreuzy et al., 2001; Bonnet et al., 2001), mesoscale fractures tend to be particularly abundant and play a correspondingly important role with regard to the effective hydraulic properties of fractured reservoirs. When a seismic wave travels through a

formation containing mesoscale fractures, pore fluid pressure gradients arise between the softer fractures and the stiffer embedding background as well as between interconnected fractures (e.g., Rubino et al., 2013, 2014, 2016; Vinci et al., 2014; Gurevich et al., 2009). These pressure imbalances cause fluid pressure diffusion (FPD) between the fractures and their embedding background known as fracture-to-background FPD, as well as between connected fractures, known as fracture-to-fracture FPD. The corresponding effects manifest themselves in the form of seismic attenuation and velocity dispersion. The governing physical processes can be assessed using Biot's (1962) theory of poroelasticity, which permits to comprehensively characterize FPD effects induced by the strains associated with seismic waves. However, the numerical simulation of wave propagation accounting for the effects of mesoscale fractures on seismic attenuation and dispersion is computationally prohibitive, due to the very fact that the scale, at which these effects prevail, is much smaller than the seismic wavelengths (e.g., Rubino et al., 2016). To circumvent this problem, effective-medium-type upscaling approaches have proven to be an efficient means of characterizing FPD effects in formations containing mesoscale heterogeneities and/or fractures.

In the context of effective-medium-type upscaling approaches, a representative sample of the formation of interest is subjected to a series of numerical stress or displacement tests in order to emulate the deformation imposed by a propagating seismic wavefield (e.g., Masson and Pride, 2007; Rubino et al., 2009). The resulting stress and strain fields are then used to infer the equiv-

alent phase velocity and attenuation for the medium. In the recent past, these upscaling approaches have been successfully employed to explore FPD effects in mesoscale fractured media of increasing complexity and realism (e.g., Rubino et al., 2013, 2017; Hunziker et al., 2018). Most of the above mentioned works were, however, based on the assumption of full water saturation. Conversely, in high-enthalpy geothermal systems, it is important to assess the effects of partial saturation, as steam may be present due to natural causes (e.g., Scott, 2020) or due to decompression effects during production operations (e.g., Barbier, 2002).

The presence of steam in geothermal reservoirs is governed by the local pressure and temperature conditions, and, thus, it is of interest to assess whether seismic methods can provide relevant information in this regard. Grab et al. (2017a) studied the seismic effects of partial steam saturation in a fractured geothermal reservoir. To do so, the authors considered that the steam phase is distributed in the form of sub-pore-scale bubbles throughout primarily water-saturated fractures and their embedding background. As such, the authors represent the properties of the corresponding gas-liquid mixture as an effective fluid for the purposes of modelling. There is, however, evidence to show that the spatial distribution of wetting and non-wetting fluids, such as water and steam, in fractured formations is partly determined by capillary forces (e.g., Glass et al., 2004). This characteristic, in turn, implies that steam should preferentially concentrate in fractures, as they constitute regions with particularly low entry pressures. Taking this fluid

distribution characteristic into account, Solazzi et al. (2020) analyzed the effects of fracture-to-background and fracture-to-fracture FPD processes in a brine- and CO₂-saturated fractured formation. The authors show that the amount and the spatial distribution of the fluid phases have a significant effect on seismic velocity and attenuation estimates for both P- and S-waves. Conversely, the importance of these effects in scenarios with varying fracture densities and connectivities, which have been identified as key variables with regard to the seismic response of monosaturated media, remains as of yet unexplored.

The objective of this study is to improve our understanding of the seismic response of partially saturated fractured media in general and high-enthalpy fractured geothermal reservoirs in particular. To this end, we focus on the presence or absence of steam in high-enthalpy fractured geothermal reservoirs and explore the corresponding impact on seismic characterization and monitoring efforts. Throughout this study, changes in seismic velocities due to steam saturation are compared with changes associated with pure fracture density variations, as both saturation and fracture density changes are plausible results of pressure changes in geothermal reservoirs. The paper proceeds as follows. First, we present the methodological background related to the generation of poroelastic models of partially saturated fractured media and for evaluating their effective seismic properties by accounting for the prevailing FPD effects. Then, we analyze the resulting behavior of P- and S-wave velocities as functions of the steam saturation of the fractures and their in-

terconnectivity degree. These results are compared to those corresponding to the high-frequency limit, which does not account for FPD effects. Based on these results, we then consider a canonical geological model and study the sensitivity of Rayleigh waves and variations of seismic reflection amplitudes with incidence angle (AVA) with regard to these parameters. As previously mentioned, we also explore whether time-lapse seismic monitoring has the potential of differentiating between changes in fracture density and steam saturation.

3.3 Methodology

In this section, we provide a summary of the numerical upscaling procedure employed to obtain effective seismic properties of poroelastic samples containing mesoscale fractures. We then describe how we generate realistic fracture networks with different levels of fracture interconnectivity and varying fracture fluid content. Finally, we provide an overview of FPD effects in fractured media and their impact on key seismic characteristics.

3.3.1 Numerical Upscaling Procedure

To obtain effective seismic properties of a porous medium containing mesoscale fractures, we consider a typical sample of the corresponding medium and subject it to a set of numerical tests consisting of harmonic displacements applied on its boundaries (e.g., Rubino et al., 2009). The response of the samples are evaluated using Biot's theory of poroelasticity, which naturally

accounts for FPD effects (Biot, 1956a,b). The rock samples contain mesoscopic fractures that are conceptualized as highly porous, highly permeable, and highly compliant inclusions embedded in a much stiffer and much less porous and permeable background (e.g., Nakagawa and Schoenberg, 2007). It is worth noting that, even in presence of media with very low porosities and permeabilities, the theory of poroelasticity remains valid and that, for sufficiently low values of these properties, the medium effectively behaves as an elastic solid (e.g., Bourbié et al., 1987; He et al., 2022). For seismic frequencies, it is safe to neglect inertial terms in the numerical upscaling procedure (e.g., Rubino et al., 2013). Hence, the poroelastic equations of motion (Biot, 1956a,b) reduce to the so-called consolidation equations (Biot, 1941), which, in the so-called $\mathbf{u} - p$ form and in the space-frequency domain are given by

$$\nabla \cdot \boldsymbol{\sigma} = 0, \quad (3.1)$$

$$-j\alpha \nabla \cdot \mathbf{u}(\omega) - j \frac{p(\omega)}{M} + \frac{1}{\omega} \nabla \cdot \left(\frac{\kappa}{\eta} \nabla p(\omega) \right) = 0, \quad (3.2)$$

where $\boldsymbol{\sigma}$ is the total stress tensor, ω the angular frequency, j the imaginary unit, \mathbf{u} is the solid displacement, p the fluid pressure, η the fluid viscosity, κ the permeability, M the inverse of the fluid storage coefficient, and α the Biot-Willis parameter. The total stress tensor $\boldsymbol{\sigma}$ is a function of the strain $\boldsymbol{\epsilon}$ and of the fluid pressure p and can be written as

$$\boldsymbol{\sigma} = 2\mu \boldsymbol{\epsilon}(\mathbf{u}) + \lambda_{\text{ct}} \text{tr}(\boldsymbol{\epsilon}(\mathbf{u})) \mathbf{I} - \alpha p \mathbf{I}, \quad (3.3)$$

with $\boldsymbol{\epsilon}(\mathbf{u})$ defined as

$$\boldsymbol{\epsilon}(\mathbf{u}) = \frac{\nabla \mathbf{u} + \nabla \mathbf{u}^T}{2}, \quad (3.4)$$

where μ is the shear modulus of the dry frame, λ_c the Lamé parameter, \mathbf{I} is the identity matrix, and $\text{tr}()$ denotes the trace operator. The Biot-Willis parameter α , and the Lamé parameter λ_c are given by

$$\alpha = 1 - \frac{K_m}{K_s}, \quad (3.5)$$

$$M = \left(\frac{\alpha - \phi}{K_s} + \frac{\phi}{K_f} \right)^{-1}, \quad (3.6)$$

and

$$\lambda_c = K_m + \alpha^2 M - \frac{2}{3}\mu, \quad (3.7)$$

where ϕ denotes the porosity and K_f , K_m , and K_s are the bulk moduli of the fluid phase, the dry matrix, and the solid grains, respectively.

Due to computational constraints, we perform a 2D analysis under the hypothesis of plane strain conditions (Rubino et al., 2016). As previously stated, in order to obtain the effective stiffness matrix of the considered medium, we apply three oscillatory relaxation tests to a representative sample (Rubino et al., 2016). The first test (Figure 3.1a) consists of a harmonic vertical compression, which is performed by applying a time-harmonic homogeneous vertical displacement at the top boundary of the representative sample, while keeping the vertical displacement null at the bottom boundary. The second test (Figure 3.1b) is a harmonic horizontal compression test, which consists of the application of a normal displacement at a lateral boundary of the sample, while keeping the horizontal displacement null at the opposing boundary. The third and final test (Figure 3.1c) consists of the application of a harmonic horizontal displacement at the top boundary

of the sample, while keeping the bottom boundary fixed in place. Following Favino et al. (2020), unless otherwise stated, the displacements and pressures obey periodic boundary conditions. Given that the overall response of a heterogeneous poroelastic medium can be effectively reproduced by those of an effective homogeneous viscoelastic solid (e.g., Rubino et al., 2016; Sollazzi et al., 2016), the volumetric averages of stress and strain, in response to each of the three tests outlined above, can be related through an effective frequency-dependent and complex-valued stiffness matrix (e.g., Rubino et al., 2016)

$$\begin{pmatrix} \langle \sigma_{11}^k(\omega) \rangle \\ \langle \sigma_{22}^k(\omega) \rangle \\ \langle \sigma_{12}^k(\omega) \rangle \end{pmatrix} = \begin{pmatrix} C_{11}(\omega) & C_{12}(\omega) & C_{16}(\omega) \\ C_{12}(\omega) & C_{22}(\omega) & C_{26}(\omega) \\ C_{16}(\omega) & C_{26}(\omega) & C_{66}(\omega) \end{pmatrix} \begin{pmatrix} \langle \epsilon_{11}^k(\omega) \rangle \\ \langle \epsilon_{22}^k(\omega) \rangle \\ \langle 2\epsilon_{12}^k(\omega) \rangle \end{pmatrix}, \quad (3.8)$$

where $k = 1, 2, 3$ refers to three oscillatory tests, $C_{ij}(\omega)$ are the components of the stiffness matrix in Voigt notation, and $\langle \epsilon_{ij}^k(\omega) \rangle$ and $\langle \sigma_{ij}^k(\omega) \rangle$ represent the volume-averages of the strain and stress components in response to the test k , respectively. This system of equations has nine equations and six unknowns, and the best-fitting values of $C_{ij}(\omega)$ are obtained by a least squares algorithm, using the averaged stress and strain fields obtained from the three tests for each frequency. The resulting phase velocities are (Rubino et al., 2016):

$$V_{P,S}(\omega, \theta) = \frac{\omega}{\Re(\tilde{\nu}_{P,S}(\omega, \theta))}, \quad (3.9)$$

where \Re denotes the real part, $\tilde{\nu}_{P,S}(\omega, \theta)$ are the complex-valued wavenumbers obtained by solving the elastodynamic equation in a medium defined by the stiffness matrix in Equation (3.8). The reader is referred to the work of

Rubino et al. (2016) for the detailed procedure of obtaining the coefficients of the stiffness matrix combining the stress and strain measurements of the three oscillatory tests and the resulting phase velocities. Further details about the corresponding numerical implementation and boundary conditions can be found in Favino et al. (2020). Effective-medium-type scaling approaches are based on the assumption that the size of the sample modelled constitutes a representative elementary volume (REV) of the probed formation. A sample corresponds to a REV, (i) when it is structurally typical of the studied rock volume and (ii) when the inferred seismic properties are independent of the boundary conditions applied (e.g., Milani et al., 2016; Caspari et al., 2016). When considering complex fracture networks, generating samples of the medium that are large enough to constitute a REV may not be feasible. To overcome this difficulty, we follow the approach of Rubino et al. (2009) and Quiroga et al. (2022), who employ the previously outlined upscaling approach in a Monte Carlo fashion on sub-REV-size samples that are within our numerical capabilities. The Monte Carlo procedure consists of obtaining representative mechanical properties by averaging a sufficient number of stochastic realizations of samples with the same statistical properties. In this study, we obtain P- and S-wave velocities of samples with the same degree of fracture connectivity and steam saturation. The stabilization of the standard deviation of the averaged velocities as a function of the number of realizations serves as the convergence criterion (Rubino et al., 2009). Once the convergence has been achieved, we can consider the inferred averaged

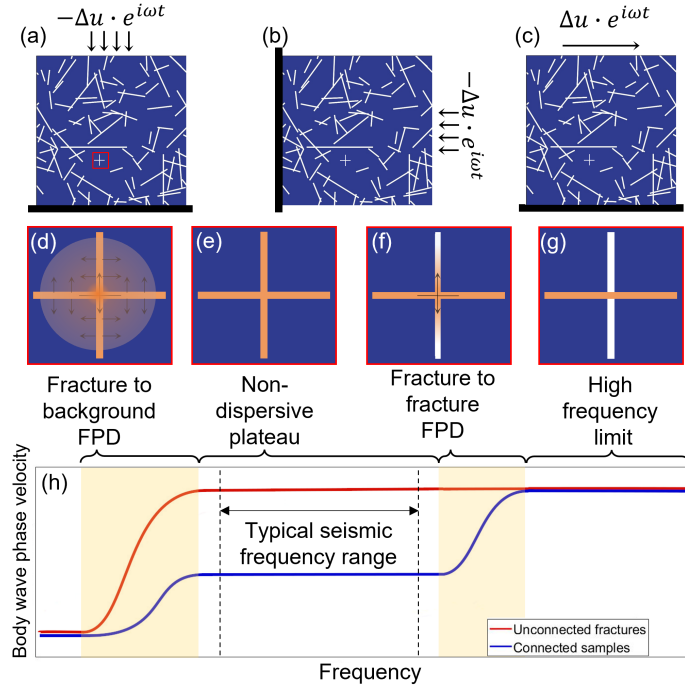


Figure 3.1: Schematic illustration of the (a) vertical, (b) horizontal, and (c) shear numerical oscillatory relaxation tests employed to obtain the equivalent stiffness matrix of the considered sample. (d, e, f, g) Fluid pressure distributions in a subsection of the sample highlighted in (a) subjected to a vertical compression for different dispersion regimes. Increasing pressure is denoted by progressive intensities of orange. (d) FB-FPD: pressure exchange between fractures and their embedding background, (e) non-dispersive plateau: pressure is equilibrated between connected fractures; (f) FF-FPD: pressure exchange between connected fractures; (g) High frequency limit: pressure confined to the horizontal fracture. (h) body wave velocities as functions of frequency for samples with unconnected (red line) and connected fractures (blue line). The frequency ranges where body wave dispersion due to FPD prevails are highlighted in yellow. Typical frequency range of seismic studies is shown inside the non-dispersive plateau.

seismic velocities as being representative for the considered formation as a whole. Correspondingly, we refer to these averages as *effective body wave velocities* from now on. Appendix A provides a step-by-step description of the upscaling procedure outlined above.

3.3.2 Fracture Network Properties

For the numerical analysis, we consider mesoscale fracture networks with a uniform distribution of fracture orientations and a power law distribution of fracture lengths. The latter is widely regarded as a seemingly universal and ubiquitous characteristic of fractures (e.g., de Dreuzy et al., 2001; Bonnet et al., 2001). Following previous works on this topic (e.g., Hunziker et al., 2018; Quiroga et al., 2022), we use

$$n(L) = F_d(a - 1) \frac{L^{-a}}{L_{min}^{1-a}}; L \in [L_{min}, L_{max}], \quad (3.10)$$

where L is the fracture length, $n(L)$, is the density function quantifying the number of fractures in the considered fractured formation with a length comprised between L and $L + dL$, where dL denotes an infinitesimal increment of length, a is the so-called characteristic exponent of the fracture size distribution, and L_{min} and L_{max} are the bounding minimum and maximum length values, respectively. The exponent a can take values between 1.5 and 3 and controls the prevalence of shorter to longer fractures within the limits given by L_{min} and L_{max} . Following Hunziker et al. (2018), we choose an intermediate value of 2.25. F_d is the fracture density defined as the ratio of area of the fractures and the total area of the sample. With regard to the intercon-

nectivity of fractures, we consider three scenarios: (i) a randomly connected scenario, where fractures are randomly placed; (ii) a fully connected scenario, where fractures are randomly placed but ensuring that all of them have at least one connection with another fracture by randomly relocating unconnected fractures; (iii) a fully unconnected scenario, where fractures do not have any connections between each other, a configuration that is achieved by randomly relocating connected fractures.

In order to simulate partial saturation of water and steam in the context of a fractured formation, we use the following saturation procedure. We start with samples whose embedding background and fractures are completely saturated with water. Then, we progressively increase the percentage of steam saturation in the fracture pore space until all fractures are steam saturated, while the background remains saturated with water. We ignore the possibility that some regions of the embedding low-porosity background may also contain steam as the corresponding mechanical effects are of subordinate importance to fracture related FPD effects. Fractures are always completely saturated with either water or steam. This is achieved by saturating first the longer fractures with steam, as they tend to be associated with greater permeabilities (e.g., Vermilye and Scholz, 1995). It is expected that these fractures are more susceptible to pressure changes, which are a key driving mechanism for the appearance of steam in our model. In this context, it is important to note that the poroelastic properties, including the permeability, of the material filling the fractures, are kept invariant in our model in order to

minimize secondary effects and focus on those related to changes in saturation and interconnectivity.

In order to minimize the number of samples that ensure convergence of the Monte Carlo procedure, we impose certain restrictions in the fracture network creation process. For each realization to be averaged in the Monte Carlo procedure, we draw a particular sampling of the fracture length distribution by employing the density function described in Equation 3.10. This fracture length distribution is then used, by varying fracture placement and orientations, to generate the three different connectivity scenarios explained above. These samples are initially considered to be completely saturated with water and their fracture networks are then progressively saturated with steam according to the procedure described above, thus, resulting in samples with varying steam saturation values. In this way, each realization is composed of several samples, which share a common fracture length distribution, and, in the case of samples with a same degree of connectivity, but varying steam saturation, the placement and orientation of fractures is identical. This is illustrated in Figure 3.2, which illustrates that the saturation process is done on the same fracture network for each connectivity scenario. For each new realization to be averaged, a new fracture length distribution is drawn, and the process is repeated until the convergence criterion for each connectivity and steam saturation scenario is achieved. Like this, we can assure that changes in the mechanical properties in each realization are either due to changes in fracture connectivity or due to changes in saturation and,

hence, unrelated to other factors, which are not the objective of study of this work.

3.3.3 Fluid Pressure Diffusion Effects

In the following, we briefly outline the nature and characteristics of FPD effects in fractured formations, based on recent works in the literature (e.g., Rubino et al., 2013, 2017; Hunziker et al., 2018; Solazzi et al., 2020). We consider samples with fractures that are in the mesoscopic scale range, that is, the fractures are larger than the pore scale but smaller than the dominant wavelength. For typical seismic frequencies between 5 and 60 Hz, and typical upper crustal P-wave velocities between 3000 and 6000 m/s, the wavelengths tend to be larger than 50 m, while the fractures considered in these studies tend to be shorter than one meter. When a seismic wave propagates through a fluid-saturated porous medium containing fractures in this scale range, the viscous friction associated with FPD effects results in seismic energy dissipation, which manifests itself in the form of velocity dispersion and attenuation. In the presence of connected fractures, two manifestations of FPD can arise (Rubino et al., 2013). The large stiffness contrast between fractures and their embedding background generates pressure gradients in response to the strains associated with seismic wave propagation, which, in turn, generate oscillatory fluid flow between these regions. This process is referred to as fracture-to-background FPD (Figure 3.1d). Additionally, fluid pressure gradients occurring within intersecting fractures undergoing different levels

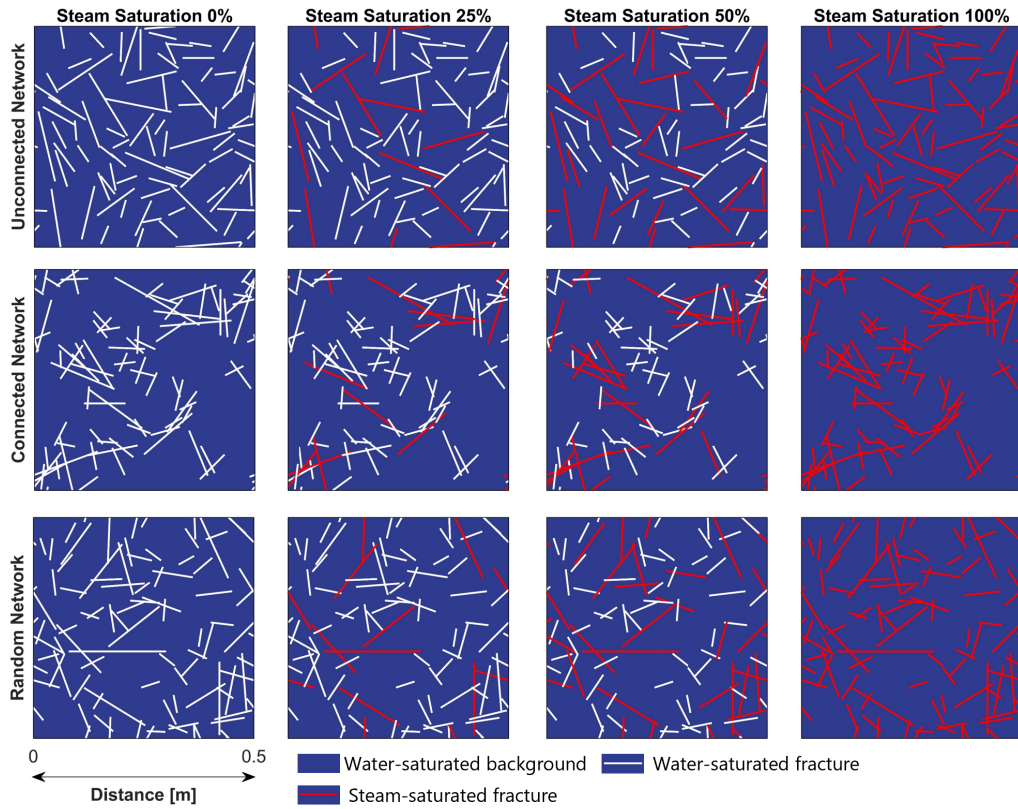


Figure 3.2: Examples of the fractured samples employed in the Monte Carlo procedure. Samples are 50 cm x 50 cm, the fracture area represents 1% of the total sample area, and the minimum and maximum fracture lengths are 4 and 25 cm, respectively. White-colored fractures denote brine-saturation while red-colored fractures denote saturation by steam. The top row represents totally unconnected fracture networks, the middle row totally connected fracture networks, and the bottom row randomly connected fracture networks. Steam saturation increases from left to right.

of compression/extension due to their respective orientations with respect to the direction of seismic wave propagation result in fracture-to-fracture FPD (Figure 3.1f). If the intersecting fractures contain fluids with differing compressibilities, such as liquid and gas, fracture-to-background FPD effects are diminished in comparison to fully water-saturated fractures (e.g., Kong et al., 2013; Solazzi et al., 2020). This is due to the fact that the lower compressibility of gas allows for a lower overall equilibrium pressure within the fractures, thus, reducing the pressure gradient between the fractures and the background and, hence, resulting in smaller fracture-to background FPD. The presence of varying fracture saturation also affects fracture-to-fracture FPD, but, in this case, the orientation of the fractures with regard to the incident P- or S-waves affects the outcome (Solazzi et al., 2020). Depending on whether the liquid or the gas are compressed by the seismic waves, FPD effects are either enhanced or diminished. If the liquid phase is preferentially compressed, the more compliant gas allows for a larger amount of liquid to flow into the connected gas-saturated fractures as compared to the scenario of both fractures being saturated with liquid. This increase in fluid flow translates into stronger FPD effects. Conversely, when the more compliant gaseous phase is preferentially compressed, the increase in pressure is less pronounced, which, in turn, does not favor FPD between connected fractures.

When looking at the associated frequency ranges, fracture-to-background FPD tends to occur at lower frequencies than fracture-to-fracture FPD, be-

cause the characteristic frequencies of these FPD manifestations are proportional to the permeability of the regions experiencing fluid flow. Given that the permeability of the embedding background is inherently much smaller than that of the fractures, fracture-to-background FPD occurs over a longer timescale and, thus, prevails at lower frequencies than fracture-to-fracture FPD. Above the frequency range, at which fracture-to-background FPD prevails, the sample behaves as if the fractures were hydraulically isolated from the background. The frequency range between the fracture-to-background and fracture-to-fracture FPD regimes is characterized by pressure equilibrium within connected fractures, which substantially reduces the stiffening effect of the fracture fluid compared to the high-frequency limit (Rubino et al., 2017). Correspondingly, this frequency range presents little to no velocity dispersion, and is hereafter denoted as the “non-dispersive plateau” (Figure 3.1e), in which the medium essentially behaves elastically. It is worth noting that, in the presence of two fluid phases, the frequency range, at which fracture-to-fracture FPD prevails, can be wider than in the case of single-phase saturation (Solazzi et al., 2020). For frequencies higher than those, at which fracture-to-fracture FPD prevails, the sample behaves as if fractures were hydraulically isolated from the background and from each other, as there is not enough time during a half wave cycle for pressure diffusion to occur. This is the so-called no-flow or high-frequency limit (Figure 3.1g), beyond which the medium essentially behaves elastically.

It is important to remark here that although there is neither attenuation

nor velocity dispersion in the frequency range covered by the non-dispersive plateau, seismic velocities are inherently lower than those associated with the high-frequency elastic limit (Figure 3.1h). This means that, even though the body wave velocities in the non-dispersive plateau are representative of a non-dispersive, elastic medium, they can only be adequately modelled by accounting for the prevailing FPD effects.

3.4 Results

3.4.1 Seismic Response of Partially Saturated Fractured Granite

In order to obtain the mechanical response of a fractured granite, which is a typical environment hosting high-enthalpy geothermal reservoirs, we employ the physical properties listed in Table 1. The rock physical properties of granite correspond to those listed in Detournay and Cheng (1993). We model the fractures as very soft, porous and permeable inclusions whose grain level properties correspond to those of the embedding granitic background. Fractures have fixed properties regardless of their length, which were adapted from Rubino et al. (2017). The permeability of the fractures is 9 orders-of-magnitude higher than that of the background, and the resulting normal and shear compliances of the fractures are consistent with recent field measurements (e.g., Barbosa et al., 2019). We consider water as the main saturating fluid and steam as the secondary fluid. The properties of water

Rock	Granite Background	Fractures
Solid grain density (ρ^S)	2700 kg/m ³	2700 kg/m ³
Solid grain bulk modulus (K^S)	45 GPa	45 GPa
Dry frame shear modulus (μ^d)	19 GPa	0.02 GPa
Dry frame bulk modulus (K^d)	35 GPa	0.04 GPa
Permeability	1e-19 m ²	1e-10 m ²
Porosity (ϕ)	0.02	0.8
Fluid	Brine	Steam
Fluid viscosity (η)	6.6e-5 Pa.s	2.38e-5 Pa.s
Fluid bulk modulus (K^f)	0.191 GPa	0.0229 GPa
Fluid density (ρ^f)	574 kg/m ³	113 kg/m ³

Table 3.1: Properties of intact granitic background and embedded fractures. Granite properties were taken from Detournay and Cheng (1993). Fractures are represented as highly compliant, porous, and permeable inclusions, whose grain-level properties correspond to those of the embedding background (Rubino et al., 2017). Fluid properties correspond to a temperature of 350 degrees Celsius and a pressure of 167 bar for brine, and the same temperature and a pressure of 165 bar for steam. These properties are obtained from the XSTEAM matlab routine (Holmgren, 2006).

and steam are a matter of study in several works, as the interactions between the two phases can be complex (e.g., Grab et al., 2017a). For simplicity, we consider water and steam to be separated phases that do not interact with each other in terms of mixing or heat transfer during the passage of seismic waves. This first-order approximation results in the maximum difference between the module of the gaseous and liquid phases, which, in turn, implies that our results represent a best-case scenario with regard to the sensitivity of seismic methods to the presence of steam. The properties of the fluids are obtained from the XSTEAM Matlab subroutine (Holmgren, 2006) following the standards of the International Association of the Properties of Water and Steam (IAPWS). In our model, we consider a fixed temperature of 350 °C and a pressure of approximately 167 bar for the liquid water phase. The latter corresponds to the saturation pressure of liquid water for that temperature. For the fractures containing steam, we consider a pore fluid pressure of 165 bar, which allows for the existence of such gaseous phase. We assume that such decrement of pressure does not affect any other properties of the fractured rock.

We employ the upscaling procedure described in the Methodology section on square samples with a side length of 50 cm, with rectangular fractures corresponding to a fracture density $Fd = 1\%$, as schematically illustrated in 3.2. We consider fractures with a stochastic distribution of fracture lengths with an $L_{max} = 25$ cm; $L_{min} = 4$ cm, and a fixed aperture of 0.4 mm. These values correspond to aspect ratios between 625 and 100, which are consistent

with values observed in nature (e.g., Vermilye and Scholz, 1995). We define the fracture steam saturation S_s^f as

$$S_s^f = 100 * V_s^f / V_p^f [\%], \quad (3.11)$$

where V_p^f is the total pore volume of the fractures and V_s^f is the fracture pore volume saturated with steam. We compute velocities for S_s^f -values of 0, 10, 25, 50, 75 and 100%. For this, we generate 50 realizations for each of the three fracture connectivity degrees described earlier and for each fracture steam saturation modelled. As illustrated in Appendix B, we found that this number of realizations is sufficient for stabilizing the standard deviations of the velocity in the non-dispersive plateau, which is the convergence criterion of the employed Monte Carlo approach (Rubino et al., 2009). It is important to mention that, for representative effective velocities and an upper frequency limit of 60 Hz, the ratio of wavelength to fracture length is at least 40 for P-waves and 25 for S-waves. This is consistent with the assumption of mesoscale fractures in our upscaling procedure. Figure 3.3 shows the P- and S-wave velocities as functions of frequency for single samples, that is, for individual fracture networks of the ensembles used to get averaged representative values for the non-dispersive plateau. Even though such realizations do not constitute representative samples, the results shown in Figure 3.3 allow to illustrate the effects of FPD on the body wave velocities of the samples. Velocity values are shown for the connected (dotted lines) and unconnected (dashed lines) cases as well as for different levels of steam saturation of the fractures. Two manifestations of velocity dispersion can be discerned, one

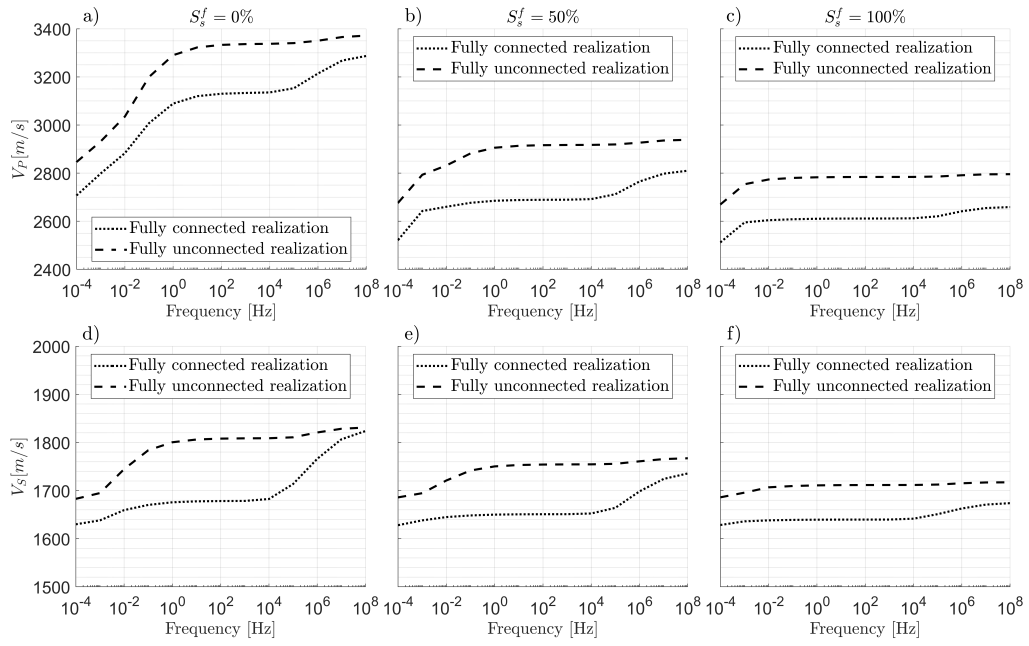


Figure 3.3: (a, b, c) P- and (d, e, f) S-wave velocities as functions of frequency for a single realization of connected (dotted lines) and unconnected (dashed lines) fracture networks. Steam saturation of the fractures S_s^f is (a, d) 0%, (b, e) 50% and (c, f) 100%.

around 10^{-2} Hz corresponding to fracture-to-background FPD and the other around 10^6 Hz corresponding to fracture-to-fracture FPD. The non-dispersive plateau is located between these two distinct FPD manifestations, where increasing levels of fracture connectivity are associated with significantly lower P- and S-wave velocities. Please note that the non-dispersive plateau includes the typical frequencies of active and passive seismic exploration and monitoring methods (approximately 60 Hz to 0.1 Hz). In this frequency range, there is not enough time in a half wave cycle to allow for pressure diffusion between the fractures and background. This means that, in the case of isolated fractures, the fluid contained inside the fractures has a significant stiffening effect in response to compressional forces. For the case of connected fractures, however, there is enough time to allow pressure to equilibrate between connected fractures, thus, greatly diminishing the fluid stiffening effect and, correspondingly, lowering the velocities of the formation. These mechanisms explains the lower velocity values for connected fracture networks in comparison to unconnected fracture networks for seismic frequencies, regardless of the saturation state in the fractures.

Again, focusing on the frequencies comprised by the non-dispersive plateau, let us now analyze the effects that partial steam saturation of the fractures has on the body wave velocities of the formation. We observe different behaviors for P- and S-wave velocities and for different connectivities of the fracture network. For P-wave velocities the marked velocity drop associated with increasing S_s^f is particularly important, indicating that P-wave veloc-

ities are adequate to detect and monitor the initial appearance of steam (Figures 3.3a, 3.3b, and 3.3c). In the case of S-wave velocities, we observe that the velocity drops associated with different levels of steam saturation are much less pronounced than for P-waves (Figures 3.3d, 3.3e, and 3.3f). These are interesting results, as Solazzi et al. (2020) reports significant effects for both P- and S-waves in a context of partial saturation of fractures with brine and CO₂. Notably, the S-wave velocities drop due to changes in fluid content are comparable to possible changes in connectivity for a fully water-saturated fracture network. In the case of P-wave velocities, on the other hand, changes associated with fluid content are much larger than those associated with changes in connectivity for a fully water-saturated fracture network.

When looking at values in the high-frequency limit, we observe that the differences between connected and unconnected cases are much narrower than those corresponding to the non-dispersive plateau. These values correspond to a high-frequency elastic representation that does not consider hydraulic communication between connected fractures. In the following, we analyze the results obtained from the Monte-Carlo-type procedure described in the Methodology section for velocities corresponding to (i) the non-dispersive plateau and to (ii) the high-frequency limit of the medium.

Figure 3.4 shows the effective body wave velocities as functions of the steam saturation for different fracture connectivities and different frequency regimes, obtained by means of the Monte Carlo approach. The frequency

regimes correspond to (i) the non-dispersive plateau (employing the velocity values for 10 Hz), in the following denominated as the *poroelastic approach*, and to (ii) the high-frequency elastic behavior of the formation, which we also refer to as *elastic*, as it corresponds to the response of an elastic background that contains elastic fractures (inclusions).

Figures 3.4a, 3.4b, and 3.4c show V_P as function of S_g^f for fully connected, randomly connected, and unconnected fracture networks, respectively, for both poroelastic (red lines) and elastic (blue lines) approaches. We observe that, in all cases, V_P decreases with increasing steam saturation in a similar way for the poroelastic and elastic models. The velocity values associated with these two cases, however, differ significantly when FPD within connected fractures is present. This is to be expected as these modelling approaches differ significantly when fracture connectivity is present, whereas in the unconnected case the responses are quite similar. We also observe that changes in V_P are more pronounced for values of S_g^f below 50%. For S-waves (Figures 3.4d, 3.4e, and 3.4f), we observe that, as in the case of V_P , while there are significant changes between the poroelastic and elastic responses randomly or fully connected networks, they are quite similar for the unconnected case. Moreover, we see that in the fully connected or randomly connected cases, the S-wave velocity turns out to be virtually insensitive to steam saturation when FPD effects are accounted for. This, in contrast with the P-wave velocity, indicates that FPD effects have a comparatively more significant impact for S-waves. We remark that fully unconnected fracture networks for a frac-

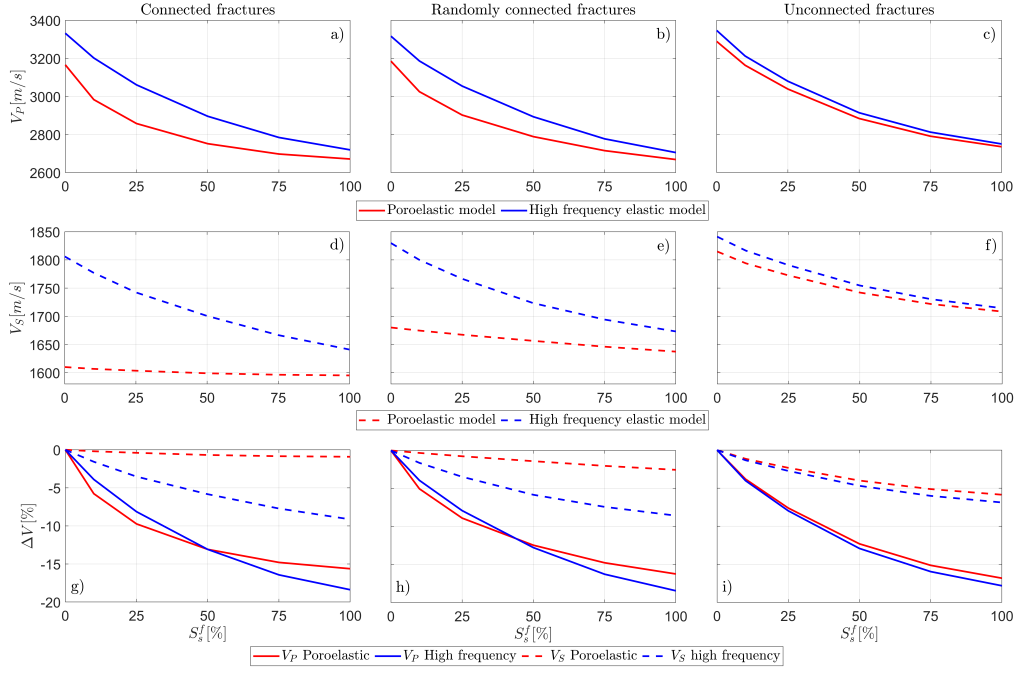


Figure 3.4: (a, b, c) P- and (d, e, f) S-wave velocities as functions of steam saturation S_s^f for different fracture connectivity scenarios. Blue lines correspond to the elastic high-frequency limit and red lines to seismic frequencies within the non-dispersive plateau. The relative velocity change for each connectivity level (g, h, i) is computed as $\Delta V = \frac{V_{P,S}(S_s^f) - V_{P,S}(S_s^f=0)}{V_{P,S}(S_s^f=0)}$, and is shown for V_P (continuous lines) and V_S (dashed lines).

ture density such as the one we consider here are unlikely in nature, and that this end-member-type scenario is shown for comparison purposes.

As previously stated, velocity changes associated with S_s^f are shown in more detail in Figures 3.4g, 3.4h, and 3.4i, which depict the relative changes with respect to $S_s^f = 0$. We can observe that the resulting relative differences for the unconnected case are similar for the poroelastic and the elastic approaches. However, in the case of fully connected (Figure 3.4g) and randomly connected (Figure 3.4h) fracture networks, there are clear differences between these models. These differences are particularly significant when considering S-wave velocities, where the poroelastic approach presents practically no changes with respect to S_s^f (red dashed lines), while the elastic model shows much higher relative changes (blue dashed lines). This result shows that employing classic elastic approaches may lead to an overestimation of the sensitivity of S-wave velocities to changes in saturation in fractured media. It is worth noting that, while S-wave velocities appear to be insensitive to changes in saturation in fractured media for the fully connected and randomly connected cases, previous research shows that they are sensitive to changes in fracture density in a geothermal reservoir context (e.g., Quiroga et al., 2022).

Given that changes of both fracture density and steam saturation can result from pressure fluctuations in geothermal reservoirs, let us analyze the sensitivity of P- and S-wave velocities to both parameters. For this, we use data from Quiroga et al. (2022) where the sensitivity of P- and S-wave velocity

Formation	Fd	V_P [m/s]	V_S [m/s]	ρ_b [kg/m ³]
	0.25%	4687	2428	2694
Fractured	0.35%	4609	2321	2692
Granite	0.50%	4510	2186	2690
	0.60%	4451	2088	2688
	0.75%	4330	1929	2687
	0.90%	4270	1825	2683

Table 3.2: Mechanical properties of fractured granite with variable fracture densities. These characteristics correspond to randomly connected fractured granite saturated with brine ($K_f = 2250 \text{ GPa}$, $\eta = 1e^{-3} \text{ Pa.s}$) for different Fd values. These values correspond to frequencies in the non-dispersive plateau. Taken from Quiroga et al. (2022).

to changes in fracture density was analyzed. The upscaling procedure and the properties of the embedding background and the fractures are identical to the ones of this work. The key difference is that in Quiroga et al. (2022) both fractures and background are saturated with brine ($K_f = 2250 \text{ GPa}$, $\eta = 1e^{-3} \text{ Pa.s}$). The effective velocities are listed in Table 3.2 and correspond to randomly connected fracture networks with fracture density Fd percentages of 0.25, 0.35, 0.50, 0.60, 0.75, and 0.90.

In order to compare the effects of steam variation considered here and the effects of fracture density in brine-saturated media explored by Quiroga et al. (2022), the plotted P-velocity values of both studies are scaled by their respective maximum values in Figure 3.5a. The highest P-wave velocity values

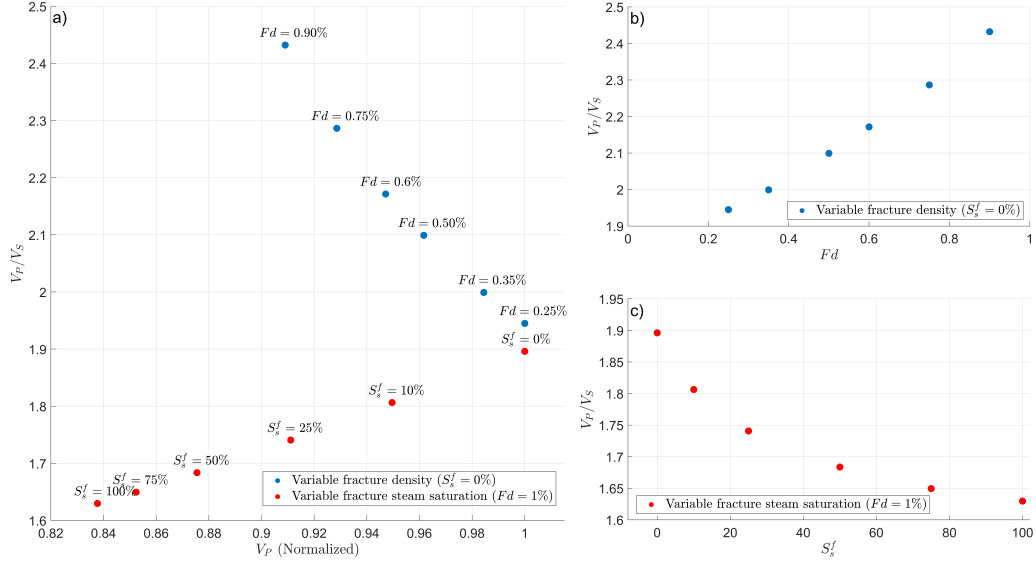


Figure 3.5: (a) Crossplot of V_P/V_S against V_P . Orange dots correspond to randomly connected fracture networks with a fixed fracture density Fd of 1% and varying S_s^f , from 0 to 100%. Blue dots were taken from Quiroga et al. (2022) and correspond to fracture networks with identical fracture properties, varying fracture density from 0.25% to 0.9% and water ($K_f = 2250$ GPa, $\eta = 1e^{-3}$ Pa.s) as the saturating fluid. V_P values are normalized with respect to the respective maximum values for ease of comparison. V_P -values for variable fracture density are divided by the value of V_P for $Fd = 0.25\%$ and the V_P -values for variable fracture steam saturation by the value of V_P for $S_s^f = 0\%$. (b) V_P/V_S ratio as a function of Fd for fracture networks with full water saturation. (c) V_P/V_S ratio as a function of S_s^f for fracture networks with fracture density $F_d = 1\%$.

occur for $S_g^f = 0\%$ in our current study and for a fracture density $Fd = 0.25\%$ for the study performed in Quiroga et al. (2022). Both increments in S_g^f and Fd are associated with similar relative decrements in P-wave velocity, therefore, it would not be possible to distinguish steam variations from fracture density changes using this parameter alone. However, the behavior of S-wave velocities allows us to distinguish between these characteristics. As shown in Figure 3.5b, increments of fracture density are associated with increases in the V_P/V_S ratio. Conversely, increasing presence of steam in the fractures is associated with decrements in the corresponding V_P/V_S ratio (Figure 3.5c). This result shows that there is a possibility for certain techniques, or combinations thereof, to identify the causes behind commonly observed velocity drops in geothermal monitoring surveys (e.g., Taira et al., 2018; Obermann et al., 2015).

3.4.2 Impact of Partial Saturation on Seismic Monitoring Techniques

Let us now explore the impact of the presence of steam on seismic monitoring methods. For this, we consider the canonical model of a high-enthalpy geothermal reservoir as depicted in Figure 3.6. We assume that the reservoir has a temperature of 350°C . In order to be close to the saturation pressure of liquid water, which, for this temperature, is approximately 1.67×10^7 Pa or 167 bar. Considering a normal lithostatic pressure gradient (e.g., Tiab and Donaldson, 2015), this corresponds to a depth of approximately 700 m.

Formation	Lithology	Depth	S_s^f	V_P [m/s]	V_S [m/s]	ρ_b [kg/m ³]
Overburden	Sandstone	0-600	-	3000	1600	2500
		m				
Upper reservoir	Partially saturated	600- 800 m	0%	3186	1680	2684
			10%	3025	1675	2683
			25%	2902	1667	2683
			50%	2789	1656	2682
			75%	2715	1646	2681
			100%	2668	1637	2681
Lower reservoir	Fractured granite	800- 1000 m	0%	3186	1680	2684
Basement	Intact granite	1000- ∞ m	-	4810	2620	2700

Table 3.3: Properties of the geological model

The physical properties of the geological model employed are described in Table 3.3. This model consists of a surficial layer of homogeneous sandstone to 600 m depth, below which the reservoir formation is located. This layer consists of 400 m of fractured granite, which we consider to be divided in two different sections. The upper section of the reservoir is located at depths between 600 m and 800 m, and can have either steam or water in its fractures. The lower section of the reservoir is located between 800 m and 1000 m depth, and it is saturated exclusively with water, as, at these depths the higher lithostatic pressure does not allow for the occurrence of steam. Below the reservoir formation, there is a semi-infinite layer of intact granite, with the same petrophysical properties as the background reservoir rock (Table 3.1). The sandstone layer and the intact granite basement are considered homogeneous and elastic, and, hence, seismic waves traversing them are not attenuated or dispersed. Conversely, the seismic velocities for the upper and lower reservoir are those obtained from the upscaling procedure (Figure 3.4). We consider for the upper reservoir different values of S_g^f , while the lower reservoir is fully saturated with water. We employ the velocity values corresponding to randomly connected fracture networks, as it is the case that can be considered as more realistic compared to the end-member type scenarios of completely unconnected or completely connected fracture networks explored in the previous section. In the following, we utilize this model to simulate results related to Rayleigh wave monitoring and reflection seismic surveys.

Rayleigh wave dispersion modelling

To compute Rayleigh wave velocity dispersion, we employ the so-called fast delta matrix algorithm (Buchen and Ben-Hador, 1996). This algorithm considers homogeneous horizontal layers with no velocity dispersion. Although we are employing a poroelastic upscaling procedure that accounts for velocity dispersion due to FPD, for the frequencies of interest for this analysis (~ 0.1 Hz to ~ 3 Hz) fall into the non-dispersive plateau and the corresponding velocities, thus, present negligible velocity dispersion (Figure 3.3). As absolute differences between Rayleigh wave dispersion curves might be difficult to discern, we compute relative velocity differences as $\Delta V_{p,g}(S_s^f) = \max_{freq}(\frac{V_{p,g}(S_s^f) - V_{p,g}(0)}{V_{p,g}(0)})$, that is, $\Delta V_{p,g}$ is the relative velocity difference for the frequency where it attains its maximum value, $V_{p,g}(S_s^f)$ is the frequency-dependent Rayleigh wave velocity for a given S_s^f and $V_{p,g}(0)$ is the Rayleigh wave velocity for $S_s^f = 0$. The subindexes p, g denote phase and group velocities, respectively. To model the sensitivity of Rayleigh wave based methods to different fracture steam saturation, we consider different values of S_s^f in the upper part of the reservoir. The results of the Rayleigh wave phase and group velocity, as well as the associated relative velocity differences for different S_s^f values, are shown in Figure 3.7.

Figures 3.7a and 3.7b show the Rayleigh wave phase and group velocity dispersion considering the poroelastic and elastic approaches, respectively. For both phase and group velocities and for both approaches, we observe higher velocities for low frequencies, due to the fact that Rayleigh waves

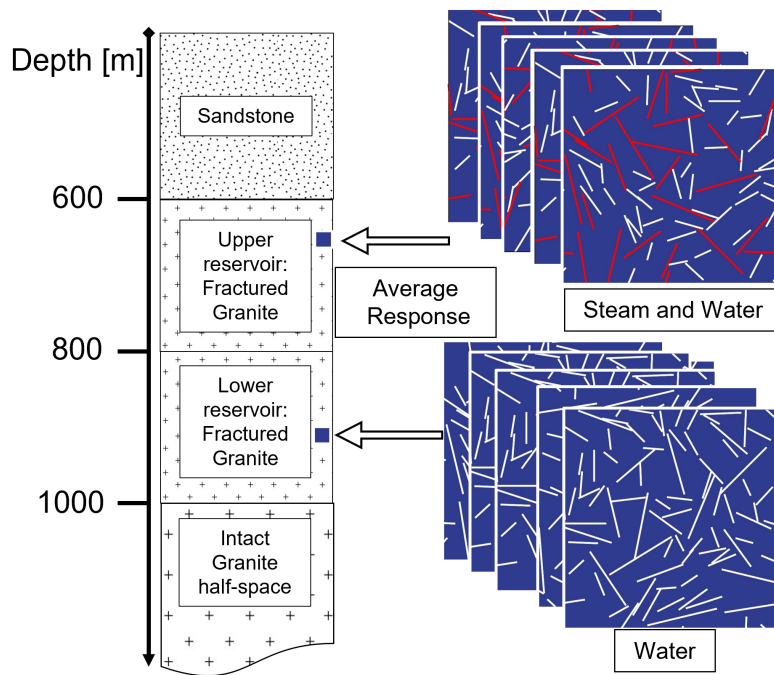


Figure 3.6: Schematic representation of the geothermal reservoir model employed in the analysis. The sandstone and intact granitic layers are considered to be homogeneous, while the granitic reservoir is characterized as a fractured formation with the fractures being saturated with either water and steam (upper part of the reservoir) and only water (lower part of the reservoir).

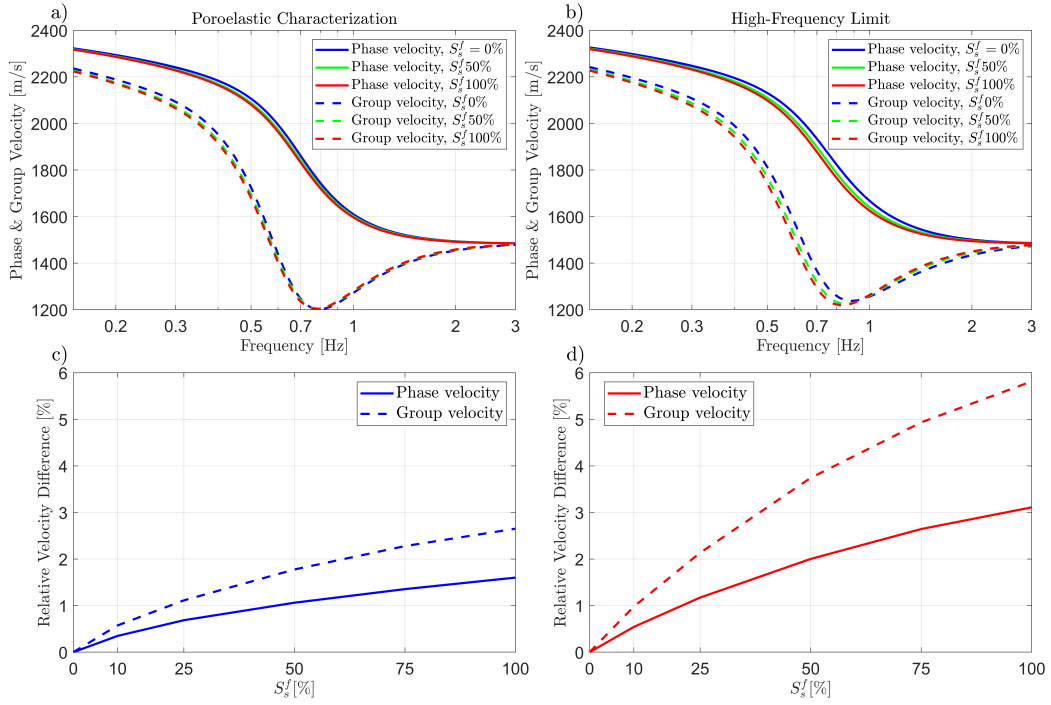


Figure 3.7: (a, b) Phase and group velocity dispersion of Rayleigh waves for the model described in Table 3.3 for different levels of steam saturation in the upper part of the reservoir, considering (a) a poroelastic and (b) an elastic approach. Relative velocity difference ($\Delta V_{p,g}(S_s^f)$) for phase (solid lines) and group velocities (dashed lines) for (c) poroelastic and (d) elastic approaches. Relative velocity differences are computed as the maximum difference between the dispersion at a certain steam saturation and the dispersion corresponding to a steam saturation of 0% divided by the value of the latter.

penetrate deeper due to the correspondingly longer wavelengths. This corresponds to the stiffer intact granitic basement in our model. In addition, the velocities decrease as the frequency increases, and we can observe that the frequencies where variations of S_s^f have an impact on the Rayleigh wave measurements are comprised between 0.2 Hz and 1.5 Hz. It is also worth noting that there is a discrepancy between the modelled impact of steam saturation using a poroelastic approach and an elastic approach. This discrepancy may lead to an overestimation of the ability of Rayleigh-wave-based techniques to detect the presence of steam in geothermal reservoirs. Figures 3.7c and 3.7d show the relative difference between varying degrees of steam saturation in the upper reservoir and the case of an upper reservoir without the presence of any steam. As the impact of partial saturation on S-waves is limited when FPD are taken into account, we observe that, in this case, the relative velocity changes in Rayleigh wave velocity dispersion amount to a maximum of $\sim 3\%$ for the case of Rayleigh group velocities and less than 2% when steam saturation goes from 0% to 100% . We observe that the relative changes for the elastic approach are almost double those of the models considering FPD effects.

It is interesting to compare the corresponding impact of varying S_s^f or fracture density Fd . As shown in Figure 3.5, changes of Fd from 0.25% to 0.90% produce relative variations of P-wave velocity similar to those produced by changes in S_s^f for the properties considered in this work. To explore the sensitivity of Rayleigh wave velocity dispersion to changes in Fd we con-

sider the reservoir's properties listed in Table 3.2. We consider the extreme case of a lower reservoir composed of brine-saturated granite with a Fd of 0.25% and fully brine-saturated upper reservoir, with varying Fd . Based on this model, the maximal variation of Rayleigh wave velocities occurs when the upper reservoir changes its density from 0.25% to 0.90%, in which case the relative change in velocities is $\Delta V_{p,g}(0.90\%) = \max_{freq}(\frac{V_{p,g}(0.90\%) - V_{p,g}(0.25\%)}{V_{p,g}(0.25\%)})$. In this case $V_{p,g}(0.90\%)$ and $V_{p,g}(0.25\%)$ correspond to the Rayleigh wave phase and group velocities for the corresponding values of Fd in the upper reservoir. $\Delta V_{p,g}(0.90\%)$ amounts to 17% and 7% for Rayleigh wave group and phase velocities, respectively. These results, compared to the values of 3% and 2% corresponding to the most extreme changes in steam saturation, show that Rayleigh wave monitoring is considerably more sensitive to changes in mechanical properties due to fracture density increments than to changes in the fluid content of the fractures, as the former have a more pronounced relative impact on the S-wave velocity.

AVA modelling

Given that, as previously shown, the impact of partial saturation is most important with regard to the P-wave velocity, reflection seismic methods are expected to be more sensitive than surface-wave-based techniques to variations in the fluid content of a fractured reservoir. To assess this hypothesis, we again employ the geological model defined by Table 3.3 to compute its amplitude-versus-angle (AVA) seismic response. The AVA response of an

interface is affected by changes in P- and S-wave velocities, and, considering the body wave velocity results previously shown, we may expect to obtain information about the fluid content of the formation. For this, we consider the target of the AVA inversion to be the intra-reservoir interface located at 800 m between the upper part of the reservoir with the presence of steam in its fractures and the lower part of the reservoir that is completely saturated by water (Table 3.3). This will provide insights on whether or not reflection seismics can, in principle, identify the lower limit of steam caps in geothermal reservoirs.

Considering that for typical surface-based seismic reflection analyses, the thicknesses of the layers involved in the considered geological model are larger than the predominant seismic wavelengths, the AVA response at the target interface can be modelled using Zoeppritz's equations (e.g., Dvorkin et al., 2014). These equations exactly model the reflection coefficients as a function of incidence angle at an interface between two homogeneous elastic solids. As the frequencies of interest of reflection seismics (approximately from 20 to 60 Hz) fall into the non-dispersive plateau for our study, the lower and upper parts of the reservoir behave as elastic solids, and Zoeppritz's equations can indeed be employed. We employ the implementation of Zoeppritz equations by Hall (2015) to compute the P-wave reflection coefficient of the intra-reservoir interface for different values of S_g^f for the upper part while the lower part is fully saturated with water. Figure 3.8a shows the P-wave reflection coefficient of the intra-reservoir interface as a function of incidence angle.

Different colors correspond to different percentages of fractures saturated by steam in the upper part of the reservoir. Solid lines correspond to the poroelastic approach for modelling the response of the reservoir and dashed lines to the elastic approach. It is worth noting that the AVA response of the formation in both cases does not present significant variations for low angles.

In practice, AVA analysis consists of extracting the properties of the subsurface from the inversion of observed reflection coefficients. To do so, it is common practice to employ a linearized approximation of Zoeppritz' equations (e.g., Mavko et al., 1998) to retrieve impedances and velocities from reflection coefficients. We employ two classic approximations due to their widespread presence in the literature and considering that the information they can infer from seismic data may be different due to the different assumptions employed by the respective authors (e.g., Thomas et al., 2016). One of the approximations we employ is that of Fatti et al. (1994), which in its two-term version approximates the P-wave reflectivity R_{PP} as function of incidence angle θ as

$$R_{PP}(\theta) = (1 + \tan^2 \theta) \frac{\Delta I_P}{2I_P} - 8 \left(\frac{V_S}{V_P} \right)^2 \sin^2 \theta \frac{\Delta I_S}{2I_S}, \quad (3.12)$$

where $\Delta I_{P,S}$ denotes the difference in P- or S-wave impedance across the interface and $I_{P,S}$ correspond to the average of the P- and S-impedances of both sides of the interface. Although the term $(\frac{V_S}{V_P})^2$ depends on the values to retrieve, we consider the usual approach of approximating it as 1/2 for the inversion process. The other approximation we consider is based on that

of Shuey (1985) and given by (e.g., Avseth et al., 2010)

$$R_{PP}(\theta) = A + G \sin^2 \theta, \quad (3.13)$$

where A is known as the intercept and corresponds to the P-reflectivity for a normal incidence and G as the gradient and depends on the physical properties of the medium. In the following, we refer to Equations (3.12) and (3.13) simply as Fatti's and Shuey's approximations, respectively. We follow a least squares inversion procedure (e.g., Quiroga et al., 2018) to obtain the corresponding AVA coefficients from synthetic reflectivity curves obtained using Zoeppritz's equations to explore their sensitivity to the steam saturation levels. For simplicity, we do not consider added noise in these simulations. Figure 3.8b shows the results of inverting for AVA intercept A and gradient G (Equation 3.13), while Figure 3.8c shows those for the inversion of Fatti's coefficients $\Delta I_p/I_p$ and $\Delta I_s/I_s$ (Equation 3.12). For these inversion results, dots represent values obtained from the poroelastic representation and crosses those corresponding to the elastic response. We observe that there is a correlation of increases of steam saturation with increase of the coefficients A and G . We observe that both coefficients tend to increase as the degree of steam saturation increases (Figure 3.8b). However, while the behavior of the inversion corresponding to the poroelastic approach and that corresponding to the elastic approach are similar, there is a significant difference in the values of the coefficients, specially for lower values of steam saturation. This shows the importance of taking into account FPD effects for the detection and monitoring of steam. For the inversion based on Fatti's

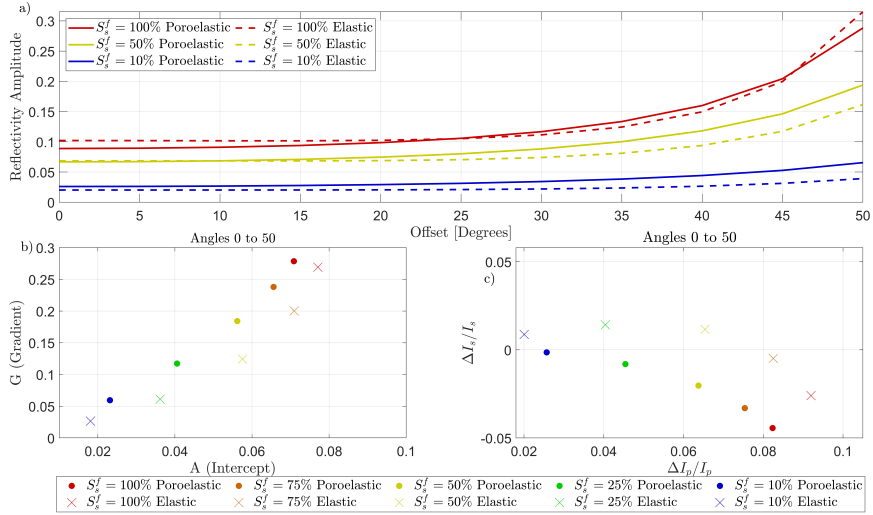


Figure 3.8: P-wave reflection coefficient and AVA coefficients for the interface between the partially steam-saturated upper part of the reservoir and the water-saturated lower part of the reservoir. (a) Reflectivity as a function of angle and S_s^f (100% red, 50% yellow, and 10% blue) for poroelastic (continuous lines) and elastic approaches (dashed lines). Results for the inversion using (b) Shuey's and (c) Fatti's approximations for incidence angles between 0° and 50° . Inversion results are shown for the poroelastic (dots) and for elastic (crosses) approaches.

equation (Figure 3.8c) we observe that there is also sensitivity to steam saturation for both coefficients. In this case, however, we can see that the behavior of the poroelastic modelling differs significantly with regard to that of the elastic approach, as the results corresponding to the latter present positive values of $\Delta I_s/I_s$ for fracture steam saturation below 75% which are negative for the poroelastic approach. This is a very important distinction as it may lead to erroneous interpretations of reflection seismic data. These results indicate, in principle, that AVA analysis is appropriate for detecting the base of the steam cap in fractured geothermal reservoirs. Comparisons of the poroelastic and elastic approaches in Figures 3.8b and 3.8c show that there are significant differences between the AVA coefficients which, thus, points to the importance of FPD effects on such coefficients.

Considering the results for body wave velocities shown in Figure 3.5, it is also interesting to determine whether AVA inversion is useful to distinguish between variations in steam saturation and fracture density. Employing the values for granitic rock with variable fracture density (Table 3.2) in the geological model of Table 3.3, we compare the results corresponding to changes in the steam saturation of the fractures and changes in fracture density. For variable fracture density AVA analysis, we consider the lower part of the reservoir to be composed of fractured granite with a fracture density of 0.25%, and the upper reservoir to have variable fracture density ranging from 0.35% to 0.90%. Figure 3.9 shows the reflectivity and the AVA inversion results for both cases for velocities corresponding to the non-dispersive plateau. In

Figure 3.9a, we see the P-wave reflectivity for different values of saturation (solid lines) and different values of fracture density (dashed lines). We observe that the reflectivities at 0° incidence show some discrepancies, which become more significant with increasing incidence angle. This translates into a good separation in the crossplots of A vs G for Shuey's approximation (Figure 3.9b) and of $\Delta I_P/I_P$ vs $\Delta I_S/I_S$ for Fatti's approximation (Figure 3.9c). These results indicate that AVA crossplot analysis could be suitable for distinguishing between increases in fracture density and changes in fluid saturation.

3.5 Discussion

In this work, we employed a numerical upscaling procedure in order to obtain effective seismic body wave velocities of granitic rocks containing mesoscopic fractures saturated with water or steam. In this context, it is important to note that the mesoscopic assumption allows us to study FPD effects by means of a numerical upscaling approach based on concepts of effective medium theory. However, the hyperbolic characteristics of fracture length distributions in nature implies that some fracture lengths will clearly exceed the considered mesoscale range. It is, in principle, possible to include mesoscopic fractures along with larger scale fractures whose length is comparable to the prevailing wavelengths in the seismic analysis and, thus, to account for both FPD and scattering effects. For this, one could perform wave propagation experiments using the effective properties derived in this work as those of the

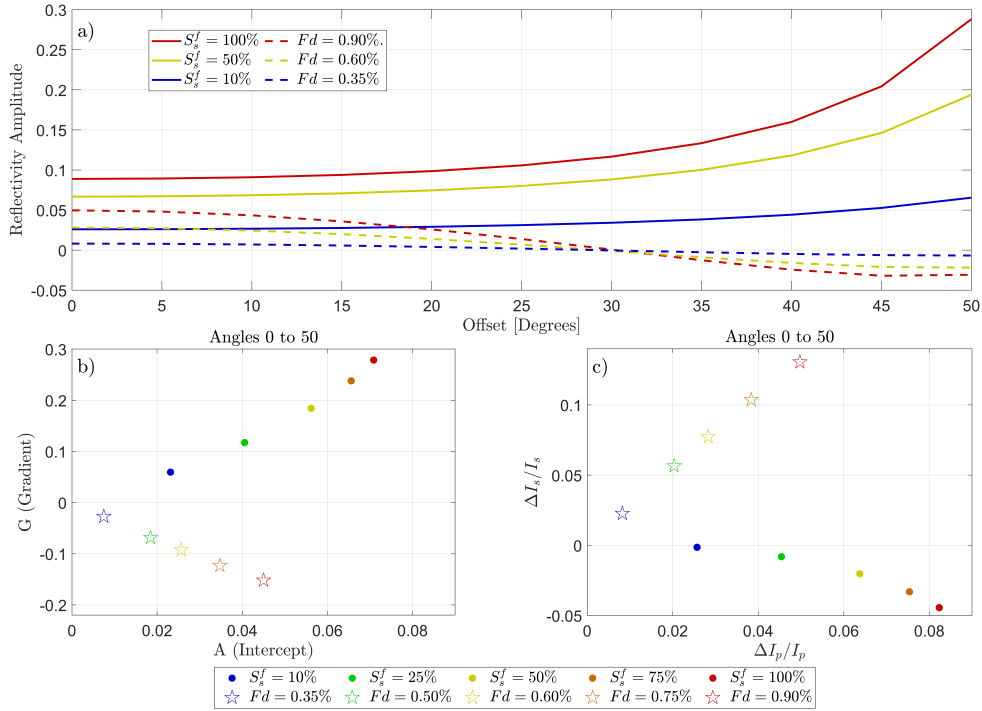


Figure 3.9: P-wave reflection coefficient as a function of incidence angle for the interfaces between: a partially steam-saturated upper part of the reservoir and a fully water-saturated lower part of the reservoir (solid lines); a fully water-saturated upper part of the reservoir with varying fracture density Fd over a fully water-saturated lower part of the reservoir with a $Fd=0.25\%$ (dashed lines). Results for the inversion using (b) Shuey's and (c) Fatti's approximations for incidence angles between 0 and 50° . Inversion results are shown for both variable S_g^f (dots) and the variable Fd scenarios (stars).

background while the larger-scale fractures would be represented by means of discrete fracture network (DFN) approaches (e.g., Lei and Sornette, 2021). An inherent limitation of this approach would be, however, that hydromechanical interaction between the mesoscopic and larger-scale fractures can not be considered.

As previously mentioned, when modelling partially saturated fracture networks, we consider fractures whose lengths obey a realistic power law distribution. However, we also apply some simplifications, both with regard to the mechanical and geometrical properties of the fractures as well in the way we saturate fractures. While we consider varying fracture lengths, we do not consider changes in the fractures' mechanical properties. This is an interesting and important topic for future research. We also consider fractures that have a rectangular shape and constant apertures, while in nature fractures present a wide range of complex geometries. Shape variations are expected to affect the mechanical properties of the fractures, for example, in the the presence of curved fracture surfaces, FPD manifestations may arise even when the fractures are isolated (Lissa et al., 2021). This is a vast field of research in its own and, hence, clearly exceeds the scope of this work, which focuses on first-order effects of partial steam saturation.

Regarding our saturation approach, our main assumptions are that the background remains saturated with water at all times and that fractures are saturated completely with either steam or with water. Regarding the former, the embedding background rock is much more stiff than the fractures,

and also considering that for seismic frequencies the background behaves as hydraulically isolated from the fractures, the potential presence of steam in the background would have a negligible effect in terms of the mechanical response of the medium. For the latter, if fractures were simultaneously saturated with both steam and water, this would, provided these fluids behave as immiscible, result in additional internal FPD effects within fractures (e.g., Solazzi et al., 2021). Recall that the distribution of fluids within individual fractures is governed by (i) the fracture properties, such as local variations in aperture (e.g., Hu et al., 2019) and (ii) the flow history (e.g., Chen et al., 2017). These effects are likely to be of subordinate importance in the given context. It is also important to note that, if fractures are simultaneously saturated by both water and steam, the assumption that these phases behave as immiscible may not be adequate, as thermodynamic fluid interactions could become important. In such a scenario, a model considering effective fluid properties might indeed be preferable (Grab et al., 2017a).

When computing AVA reflectivities, we assume a sharp separation between the upper part of the reservoir, which is partially saturated with steam, and the lower part of the reservoir, which is fully saturated with water. In reality, the transition from full steam to full water saturation is likely to be progressive, which would compromise the sensitivity of AVA methods to detect the lower limit of the steam cap. Furthermore, while AVA inversion shows promise, there are situations for which it is not possible to determine the second term of the governing equations in an inversion, for example, when

for logistical reasons, the offset range of seismic surveys is limited. In such situations, reflectivity measurements are still able to detect changes in the properties of the reservoir due to presence of steam, but it is not possible to differentiate the effects of increasing steam saturation to those related to increases of the density or connectivity of the fractures. Finally, as shown in the Results section, Rayleigh-wave-based methods are less sensitive to changes in the fluid content of the rock, but they are quite sensitive to changes in fracture density (Quiroga et al., 2022). It is, therefore, conceivable to employ Rayleigh wave inversion to complement P-wave impedance measurements, as both techniques are sensitive to changes in fracture density, while they respond very differently to changes in the fluid content of the reservoir.

3.6 Conclusions

In this work, we have analyzed the seismic response of a fractured granite formation with varying levels of steam saturation and different levels of fracture connectivity. We employed a poroelastic upscaling approach in a Monte Carlo fashion in order to obtain effective body wave velocities. The analysis of the effective body wave velocities of realistic samples reveal that partial steam saturation significantly affects the P-wave velocity while it does not have a significant impact on the S-wave velocity. These particularities are due to FPD effects and are not adequately modelled by an elastic approach. A comparison with previous works that investigate changes in fracture density and connectivity as driving causes for velocity drops observed during

seismic monitoring of geothermal scenarios indicates that the effects of increasing steam saturation and fracture density can be differentiated through an analysis of the V_P/V_S ratio. To further develop this analysis, we incorporate these velocities in a geological model compatible with the presence of hot water and steam to assess the sensitivity of different characterization and monitoring techniques. We find that: (i) Rayleigh-wave-based techniques are much less sensitive to changes in fluid saturation compared to changes in fracture density, and that employing a purely elastic characterization may lead to an overestimation of the sensitivity of this method to such changes; (ii) AVA attributes are robust in characterizing discontinuities in fluid content but correct modelling of effects of FPD on the seismic velocities is required in order to improve the interpretation of the data, especially when the range of incidence angles is limited; and (iii) in zones where AVA characterization is not possible, P-wave velocity or P-impedance estimates could be potentially combined with Rayleigh wave monitoring in order to discriminate between changes in steam saturation and fracture density.

3.7 Acknowledgments

This research has been supported by grants 200020-178946 (G. E. Q. and K. H.) and PZ00P2_180112 (M. F.) from the Swiss National Science Foundation. J. G. R. gratefully acknowledges the financial support received from CON-ICET (grant PIP 11220210100346CO). We wish to thank Junxin Guo and two anonymous reviewers as well as the editorial team for lucid comments

and constructive suggestions, which allowed us to significantly improve the quality of this work.

3.8 Appendix A

Poroelastic Characterization Workflow

In the following, we summarize the steps required for the evaluation of effective seismic body wave velocity and attenuation characteristics of a formation. This approach is based on the theory of poroelasticity of Biot (1956a,b) and takes into account FPD effects. The underlying assumptions are that the heterogeneities in the probed formation are in the mesoscale range, that is, much larger than the pore scale but much smaller than the prevailing seismic wavelengths, and that the frequencies analyzed are sufficiently low to be able to ignore Biot's intrinsic attenuation effects. For upper crustal rocks with fractures below a meter in length and typical seismic frequencies (<60 Hz), these assumptions are safely met.

The workflow is then the following:

1. Obtain the poroelastic material properties of the rocks and fluids to be modelled. For the purpose of this study, the required properties and their sources are listed in Table 1.
2. Determine the statistical properties of the fractured formation, such as fracture density, minimum and maximum fracture length, fracture aperture distribution, degree of fracture interconnectivity. Generate fractured rock

samples with the desired statistical characteristics. For this study, we employ a fixed fracture density, a power law distribution of lengths, described by Equation 3.10 (Hunziker et al., 2018), and an iterative fracture placement procedure to obtain different degrees of fracture interconnectivity. We also model different degrees of steam saturation of the fractures of the samples by completely saturating individual fractures until the desired steam saturation has been reached.

3. Apply the upscaling procedure described in the Methodology section and schematically outlined in Figure 3.1 to the rock samples to obtain the volumetric average of stress and strain (Rubino et al., 2016; Favino et al., 2020).

4. Follow the procedures described in Rubino et al. (2016) to obtain the frequency-dependent effective stiffness matrix coefficients and, thus, obtain the P- and S-wave velocities and attenuation.

5. In order to obtain the effective seismic velocities, average the results associated with samples sharing the same statistical characteristics. In our study, we average samples that share the same fracture density, degree of interconnectivity and steam saturation percentage. The averaged values can be considered as representative of the formation of interest once the standard deviation of the resulting properties as a function of the number of samples averaged stabilizes (Rubino et al., 2009).

3.9 Appendix B

Standard Deviation of the Effective Velocities

Figure 3.9 depicts the evolution of the standard deviation of the effective velocities as a function of the number of stochastic realizations averaged for fully unconnected, fully connected, and randomly connected fracture network realizations. The stabilization of this value is indicative of the convergence of the Monte Carlo procedure (Rubino et al., 2009). In view of these results, we consider an average of 50 realizations as representative of the effective velocities of the considered fractured media.

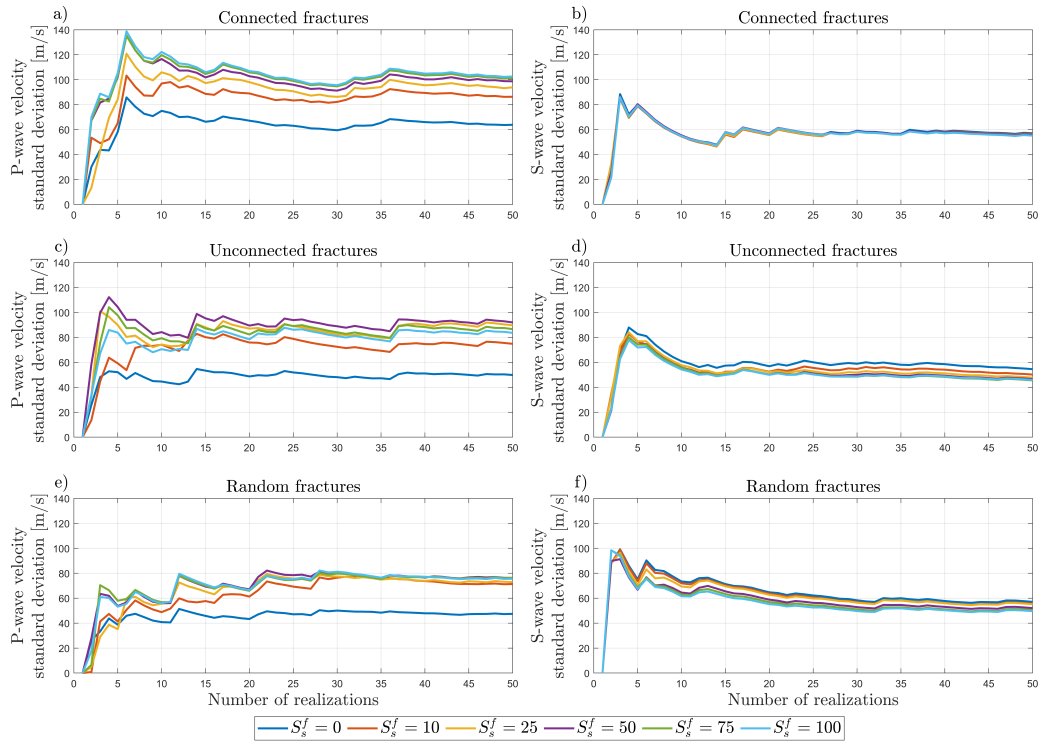


Figure 3.10: Standard deviations of (a, c, e) P- and (b, d, f) S-wave velocities for the non-dispersive plateau as functions of the number of realizations for (a, b) connected, (c, d) unconnected, and (e, f) randomly connected samples. Colors denote the percentage of steam saturation of the fractures for each series of realizations.

Chapter 4

Effective Seismic Properties of Fractured Rocks: The Role Played by Fracture Scaling Characteristics

Gabriel E. Quiroga¹, J. Germán Rubino², Santiago G. Solazzi¹, Nicolás D.
Barbosa¹, and Klaus Holliger¹

¹ Institute of Earth Sciences, University of Lausanne, Lausanne,
Switzerland.

² CONICET, Centro Atómico Bariloche - CNEA, San Carlos de Bariloche,
Argentina.

Manuscript in preparation

4.1 Abstract

Seismic characterization of fractured geological formations is important for various applications, such as hydrocarbon exploration, CO₂ sequestration, and tunneling operations. Poroelasticity is a theoretical framework that is commonly used to explore the seismic response of fluid-saturated porous formations containing fracture networks, as it permits to naturally account for the effects of fluid pressure diffusion (FPD) between fractures and their embedding background as well as within connected fractures. Despite the importance that fracture properties have on the seismic response of fractured formations, current modelling approaches tend to employ fracture properties that are independent of fracture length. This hypothesis conflicts with the evidence that suggests that several key properties of fractures are correlated in nature, such as length, aperture, compliance and permeability. This work proposes incorporating length-dependent fracture properties to improve the accuracy of seismic modelling. For this, existing datasets are used to derive relationships between aperture, permeability, and compliance of fractures with fracture length. These length-scaling properties are then employed to analyze the seismic characteristics of formations containing isolated or connected fractures. The results demonstrate that length-dependent fracture properties have a key impact on the seismic response of the models. In particular, we observe that shorter fractures tend to control the seismic response of fractured formations, producing lower velocities and higher attenuation and dispersion levels. Also, the transition frequency of the fracture-to-fracture

FPD manifestation tends to get lower values as fractures get shorter. These results are at odds with theoretical and numerical results available in the literature, thus, highlighting the importance of considering length-dependent properties in the modelling of the seismic response of fractured formations.

4.2 Introduction

The mechanical and hydraulic properties of subsurface formations are of utmost importance for a wide range of applications of economic and environmental importance, such as hydrocarbon exploration and production, CO₂ sequestration projects, nuclear waste storage, tunneling operations, and exploration and monitoring of hydrothermal reservoirs. In the particular cases of unconventional hydrocarbon reservoirs and geothermal explorations, the reservoir formations that these applications target typically consist of rocks with low intrinsic permeability. In these cases, fractures play a chief role in the overall hydraulic characteristics of the formations, as they constitute preferential paths for fluid flow. This is evidenced by the success of hydraulic fracturing to recover hydrocarbons from shale formations and also by enhanced geothermal systems that rely on fracturing to improve the efficiency of the operations. Seismic methods have proven to be particularly appropriate for the characterization of fractured rocks, due to their resolution and sensitivity to key mechanical properties. Fractures do not only affect the fluid flow within the formation, but they also have a significant impact on their mechanical properties. Fractures are softer than the embed-

ding background rock, and, as such, their presence significantly lowers the velocity of seismic waves, and they also affect other attributes, such as their anisotropy or attenuation. Linking the seismic response of a formation with their overall hydraulic properties is the goal pursued by many characterization efforts. In this regard, the use of the theory of poroelasticity of Biot (1941; 1956a; 1956b) has permitted to achieve important advances in recent years that helped to improve the interpretation of the seismic response of fractured formations.

The theory of poroelasticity allows to consider complex interactions between the rock matrix and the fluids contained within. These effects are of particular importance when fractures are considered in the models, as shown by the pioneering works of Gurevich et al. (2009) and Rubino et al. (2013), among others. In a poroelastic framework, fractures are modelled as inclusions with higher permeability, porosity, and compliance compared to the background material. Given these characteristics, the fluid contained in fractures experience higher pressure changes with respect to that occurring in the background, due to the effects of passing seismic waves, which, in turn, generate fluid pressure diffusion between the fractures and their embedding background, as well as between connected fractures of different orientations (Rubino et al., 2013, 2014). The first of these processes is known as fracture-to-background FPD (FB-FPD), and the second one as fracture-to-fracture FPD (FF-FPD). The occurrence of FPD depends on the permeability of the materials involved (e.g., Rubino et al., 2013), and, as the background rock

is less permeable than the fractures, FB-FPD occurs at lower frequencies than FF-FPD. It is proven that fracture connectivity plays a significant role in the seismic response of fractured formations (e.g., Rubino et al., 2013, 2014), which constitutes a landmark in terms of inferring fracture network characteristics from remote seismic measurements. In more recent works, the employment of the theory of poroelasticity has been considered in a wide range of applications in the context of fractured media, including analyses of the reflectivity response of fractured rocks (e.g., Rubino et al., 2022; Sotelo et al., 2021), the effects of partial saturation of fluids (e.g., Solazzi et al., 2020; Quiroga et al., 2023; Grab et al., 2017a) as well as considering frameworks for various applications such as geothermal exploration (e.g., Grab et al., 2017b,a; Quiroga et al., 2022, 2023), or borehole measurements (e.g., Barbosa et al., 2019). In particular, several works include the representation of complex fracture networks in their models, such as Hunziker et al. (2018); Quiroga et al. (2022, 2023); Grab et al. (2017b); among others. However, despite considering increasingly complex fracture network geometries, these works usually employ simple models for the properties of the fractures.

Fractures are characterized by their physical dimensions, including length, aperture and shape, as well as by their mechanical and hydraulic properties, quantified by their porosity, permeability, and compliance. Several works study the distribution of fracture lengths in natural rock formations, and support the hypothesis of fractal length distributions (e.g., de Dreuzy et al., 2001; Bonnet et al., 2001). The study of the geometrical properties of frac-

tures also extends to analyses aimed at understanding the correlation between fracture length and aperture (e.g., Hatton et al., 1994). Works focused on the mechanical properties of fractures suggest a link between fracture compliance and fracture length (e.g., Barbosa et al., 2019; Hobday and Worthington, 2012). In addition to these field studies, classic works such as Witherspoon et al. (1980) and Barton et al. (1985) establish theoretical and empirical basis pointing to the control of fracture aperture over the permeability of fractures.

Despite the abundance of evidence that suggests a correlation between fracture properties, with length appearing as a controlling factor on aperture, permeability, and compliance of the fractures, the impact that correlated fracture properties might have on the seismic response of fractured media has yet to be explored. Indeed, these correlated properties are expected to have a significant impact, as FPD is very sensitive to changes in length, permeability, and compliance of fractures. With these motivations, in this work, we first consider different sets of fracture property measurements available in the literature to derive empirical expressions for aperture, permeability, and compliance of fractures as functions of their length. We then utilize these relationships to generate different fracture models to explore the associated impact on the seismic response of fractured formations. The results are compared to models that do not consider correlated fracture properties to assess the differences caused by this common simplification.

4.3 Length-scaling Fracture Properties

4.3.1 Poroelastic Representation of Fractures

Fractures are ubiquitous features that result in discontinuities in the mechanical properties of the embedding rock, which often also have significant impact on the hydraulic properties of the host rock. The numerical representation of fractures is challenging, as the interstitial space between the interfaces that define a fracture is often filled with fragments of rock, mineral deposits or other elements, which are then compressed by the stresses prevailing on the subsurface. In view of this, open fractures can be modelled as thin poroelastic inclusions that are more compliant and permeable than the host rock (e.g., Rubino et al., 2014; Nakagawa and Schoenberg, 2007). This representation of fractures is particularly convenient as it allows to compute the seismic response in the context of Biot's theory of poroelasticity, which naturally accounts for FPD effects. This approach can be employed to obtain the seismic response of a medium that has fractures in the mesoscopic scale range, that is, fractures that are much smaller than the predominant seismic wavelength, but bigger than the pore scale. For common seismic frequencies and velocities, fractures that are below a few meters in length can be considered mesoscale.

To represent the different parts of a fractured medium of interest in the context of Biot's theory of poroelasticity, it is required to determine certain material and geometrical properties. We will consider a water-saturated

granitic rock as the background material, using the properties as listed by Detournay and Cheng (1993) and standard values for the viscosity and bulk modulus of water (Table 4.1). On the other hand, we denote the properties corresponding to the porous material composing the fractures with a superscript f . These consist of the drained bulk K_m^f and shear μ_m^f moduli of the infill material, its permeability k^f and porosity ϕ^f , alongside with the density ρ_s^f and bulk modulus K_s^f of the solid grains. In addition, the properties of the saturating fluids are required, that is, the fluid's viscosity η and bulk modulus K^{fluid} , which in this case are the same as in the background rock. Open fractures are known to have high porosity. For this reason, we assume that the fractures have a fixed porosity of 80% and that the grain-level properties (K_s^f and ρ_s^f) are identical to those of the background rock. To obtain the rest of the fracture properties, we will derive empirical relationships using fracture property measurements from the literature. These relationships consider a dependence of the fractures' mechanical and hydraulic properties with their size, according to what is commonly observed in nature.

4.3.2 Fracture Aperture

The study of the macroscopic geometric characteristic of fractures has been addressed by many authors both from a theoretical perspective (e.g., Pollard and Segall, 1987; Renshaw and Park, 1997; Olson, 2003) and based on field measurements of fractured formations (e.g., Bonnet et al., 2001; de Dreuzy et al., 2001; Hatton et al., 1994; Vermilye and Scholz, 1995). A common

Table 4.1: Properties of granitic background rock and saturating fluid (brine).

Property	Background
Solid grain density (ρ_s)	2700 kg/m ³
Solid grain bulk modulus (K_s)	45 GPa
Dry frame shear modulus (μ)	19 GPa
Dry Frame bulk modulus (K_d)	35 GPa
Permeability (k)	1e−18 m ²
Porosity (ϕ)	0.02
Fluid viscosity (η^{fluid})	1e−3 Pa.s
Fluid bulk modulus (K^{fluid})	2.25 GPa
Fluid density (ρ^{fluid})	1090 kg/m ³

Note. Embedding background is assumed to correspond to intact granite (Detournay and Cheng, 1993). The pore fluid properties correspond to brine.

aspect in these studies is a positive correlation between fracture aperture and length. To obtain a relationship that could allow to link fracture aperture values to their length, we consider the dataset presented in the classical work of Hatton et al. (1994), where fracture apertures and lengths can be compared. In Figure 4.1 we show a subset of this dataset, which corresponds to mesoscale fractures. The data are fitted to a power law function by means of a least-squares procedure which results in the following relationship

$$h = 10^{-2.12}l^{1.49}, \quad (4.1)$$

where h is the fracture aperture and l is the fracture length. Considering fractures with lengths between 1 cm and 1 m, this relationship provides apertures in the range of 1 mm and 7.6 mm, which, in turn, correspond to length over aperture aspect ratios between approximately 260 and 130. These values are within the range of those reported by de Dreuzy et al. (2001). It is interesting to note that, when considering fixed apertures for fractures, the aspect ratios grow with fracture length, while when employing this power-law-type relationship larger fractures are associated with smaller aspect ratios. In principle, this increased aspect ratio for longer fractures increases the relative contribution to fracture volume or area of larger fractures when compared to shorter fractures with the same total length. From a numerical point of view, this also affects the capability of representing smaller fractures, as the mesh should be fine enough to present enough elements inside the fractures in order to properly model FPD effects (Hunziker et al., 2018; Favino et al., 2020).

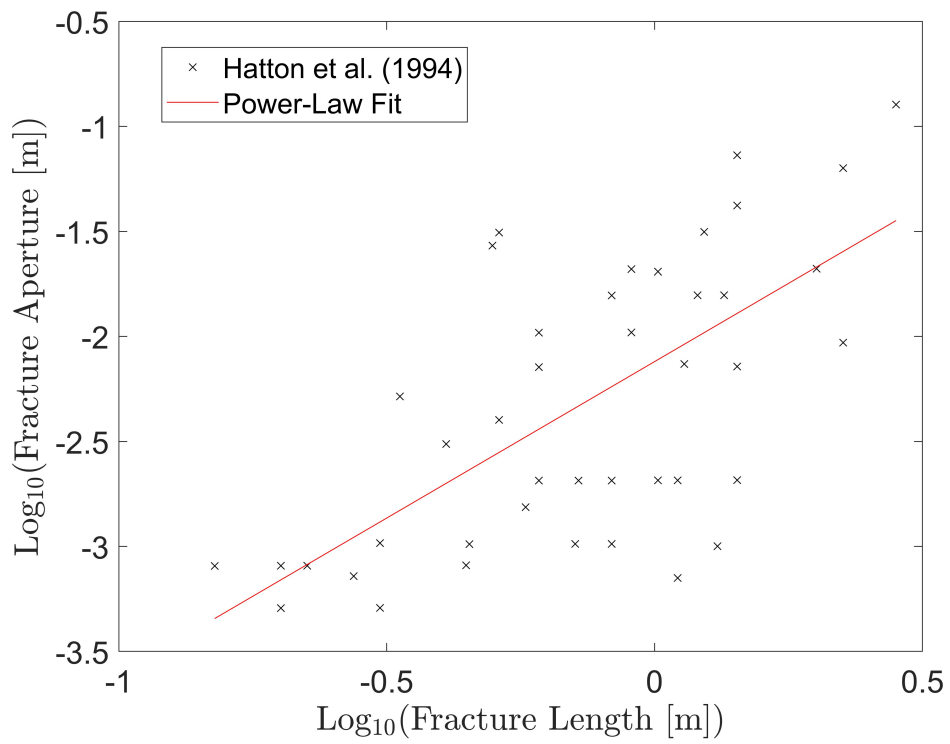


Figure 4.1: Subset of fracture length vs aperture data retrieved from Hatton et al. (1994). The power law fit follows the formula $h = 10^{-2.12}l^{1.49}$.

4.3.3 Permeability

The permeability of open fractures refers to the capacity of the fracture to allow fluids to flow through them. One of the basic ways to estimate permeability is based on the assumption that the fracture is bounded by two smooth, parallel walls. This approximation is known as the cubic law (e.g., Witherspoon et al., 1980). It leads to a hydraulic permeability as a function of the fracture aperture of the form

$$k^f = \frac{h_{pw}(h)^2}{12}, \quad (4.2)$$

where h_{pw} is the parallel wall equivalent aperture of the fracture. As the cubic law considers smooth walls for its calculation, it predicts permeabilities much higher than those observed in nature. The parameter h_{pw} accounts for discrepancies between smooth- and rough-walled fractures when implementing the cubic law. Based on experimental observations, Barton et al. (1985) proposes

$$h_{pw} = \frac{JRC^{2.5}}{\left(\frac{h}{h_{pw}}\right)^2} [\mu m], \quad (4.3)$$

where h is the aperture of the fracture and JRC is the joint roughness coefficient, which takes values from 2.5 to 20 describing fractures from very smooth to very rough, respectively (Barton and de Quadros, 1997). Different values of this parameter affect the range of permeabilities corresponding to the length variations within a sample. In order to employ this approximation, we calibrate the resulting permeabilities with those corresponding to previous works, to allow for comparisons. Despite being above the limit considered

in Barton and de Quadros (1997), we choose a JRC value of 35, which results in a permeability of approximately 100 darcys (10^{-12}m^2) for a fracture with an aperture of 0.5 mm. This relation between apertures and permeability is consistent with works such as Hunziker et al. (2018) and Quiroga et al. (2023). Considering this value of JRC , and fractures with apertures between 1 mm and 7.6 mm, the permeabilities for that range correspond to values between 1380 and 5000000 darcys. Differences in the permeability of fractures are known to affect the frequency range where FF-FPD prevails, with higher values of permeability resulting in higher frequency values (e.g., Rubino et al., 2014).

4.3.4 Dry Frame Elastic Moduli

The shear and bulk moduli of the material composing fractures cannot be directly estimated from geophysical measurements. However, these values can be inferred from measurements of dry fracture compliance. Fracture compliance is a measure of the resistance a fracture presents to closure or displacement. Several works have studied the compliance of fractures in natural rocks, both in laboratory (e.g., Lubbe et al., 2008; Pyrak-Nolte et al., 1990) and field settings (e.g., Barbosa et al., 2019; Lubbe and Worthington, 2006). These works suggest the existence of a relationship between the compliance and size of fractures, as shown, for example, in Hobday and Worthington (2012). Based on this, we consider compliance estimates of fractures available in the literature to derive a scaling relationship between fracture

length and fracture compliance.

Deriving a relationship between fracture length and compliance is challenging. The available data corresponds to a variety of rocks, methodologies, frequency ranges, confining pressures and other variables. The data available for smaller fractures is often derived from laboratory measurements, which are carried on on samples of rock that were retrieved from the field. This causes a loss of the in-situ conditions, which then need to be recreated by artificial means. For larger fractures, the measurements are performed in the field by a variety of methods that work at different frequencies and by different principles, which affects the consistency of the measurements between different works. Compliance is also known to be affected by pressure conditions (e.g., Pyrak-Nolte et al., 1990), which is also a source of uncertainty in many estimations. For these reasons, we consider two different relationships of fracture compliance with length, corresponding to static and dynamic compliance measurements. With this approach, we expect to consider a range of possible fracture compliances for a given fracture length to determine the impact of these systematically different estimations on the seismic response of fractured formations (Hobday and Worthington, 2012).

To derive a dry-fracture-compliance and length relationship for the dynamic case, which encompass frequencies from seismic to ultrasonic, we employ the compilation of results shown in Barbosa et al. (2019). From the results listed in this work, we discarded estimates corresponding to static compliance measurements, those that did not correspond to natural rocks

or those that have been superseded by more recent estimates that employ the same raw data. The dry fracture compliance results that are considered appropriate are shown in Figure 4.2, as a function of the corresponding fracture length, as reported or estimated by the respective authors. These data correspond to the works of Lubbe et al. (2008); Verdon and Wüstefeld (2013); Bakku et al. (2013); Prioul et al. (2008); Prioul and Jocker (2009); Pyrak-Nolte et al. (1990); Lubbe and Worthington (2006); Hobday and Worthington (2012); Myer et al. (1995); Herwanger et al. (2004) and Barbosa et al. (2019). For the case of the results obtained by Barbosa et al. (2019), under the assumption that the resulting fracture compliances correspond to an undrained, fluid-saturated estimation, we used Gassmann's fluid substitution method (Gassmann, 1951) to remove the effect of the saturating fluid. For this, we assume that the fluid saturating the fractures is water with a bulk modulus of 2.25 GPa, a fracture porosity of 0.8, a bulk modulus of the solid grains of 30 GPa and a fracture aperture obtained from Equation 4.1 corresponding to the length of fractures of 5 meters, as estimated by the authors.

For the case of static dry fracture compliance measurements, we base our model on the compilation of results of Hobday and Worthington (2012). From the results of this work, we do not consider the compliance estimates of fractures with lengths above the hundred of meters in length, as these fracture length values are too far from the ones of interest of this work. The works considered for this relationship are, then, those of Rutqvist (1995);

Makurat et al. (1991); Pratt et al. (1977); Zangerl et al. (2008); Giwelli et al. (2009); Barton (2006) and Pyrak-Nolte et al. (1987).

It is worth noting that for the compliance estimates corresponding to field measurements, the values may have uncertainties associated with the estimation of the number of fractures present in a formation, which can result in variations of up to one order-of-magnitude. The associated fracture lengths may also have an error of an order-of-magnitude, as the values correspond to indirect estimates rather than to direct measurements. In the case of laboratory measurements, the size of the fractures correspond to the diameter of the core samples on which the experiments are performed.

As can be seen in Figure 4.2, the estimates of static compliance are generally higher than estimates of dynamic compliance. For this reason, the relationship derived from static compliance values can be considered as an upper bound of the values of compliance that a fracture can assume, while the relationship corresponding to dynamic compliance estimates represents the corresponding lower bound. We propose a power-law-type fit of the compliance information for the static and dynamic cases as presented in Figure 4.2, with the corresponding parameters determined by a least-squares procedure. The resulting relationships between fracture dry normal compliance and length are

$$\eta_N^{dynamic} = 10^{-12.071} l^{1.257}, \quad (4.4)$$

$$\eta_N^{static} = 10^{-11.491} l^{0.64876}, \quad (4.5)$$

where η_N^x is the normal compliance of the fractures and the superscripts

indicate to which type of data it corresponds.

Estimations of fracture shear compliance in the literature are rare. So, in order to obtain the shear compliance of the fractures, we employ its relationship with normal compliance as estimated in the work of Lubbe et al. (2008), where ratios between the shear and normal compliance $\frac{\eta_N}{\eta_S}$ between 0.2 and 0.5 are reported. We consider an intermediate value of 0.35 for this study. This is consistent with earlier works, such as Nakagawa and Schoenberg (2007) where $\frac{\eta_N}{\eta_S} = 0.33$ is employed. We then obtain the shear and drained bulk moduli of the fractures from the compliances derived from the obtained empirical relationships. For this, we follow Rubino et al. (2014),

$$\eta_N = h/(K_d^f + 4/3\mu^f), \quad (4.6)$$

$$\eta_S = h/\mu^f. \quad (4.7)$$

Using these relationships and considering fracture lengths between 0.1 and 1 m, we find K_d^f to vary between 1.63 and 4.76 GPa, and μ^f between 1.07 and 3.12 GPa for the dynamic case. For the static case, K_d^f varies between 0.026 and 1.25 GPa, while μ^f varies between 0.017 and 0.82 GPa.

4.4 Effective Seismic Properties of Fractured Rocks

We employ a numerical upscaling procedure based on Biot's theory of poroelasticity to obtain the effective seismic properties of fractured formations of

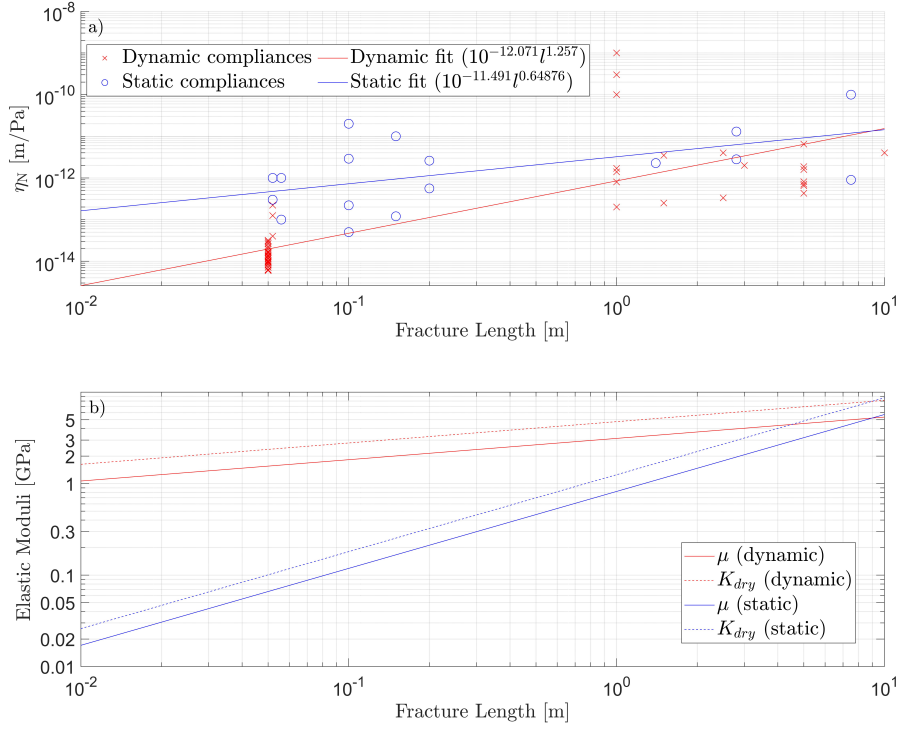


Figure 4.2: (a) Subset of fracture dry normal compliance data obtained from the literature as a function of fracture length. The dynamic compliance data (red crosses) has been selected from Barbosa et al. (2019) and the static fracture compliance data (blue circles) has been selected from Hobday and Worthington (2012). The power law fit for the dynamic case (red line) follows the formula $\eta_N = 10^{-12.071}l^{1.257}$, while the power law fit for the static case (blue line) is given by $\eta_N = 10^{-11.491}l^{0.64876}$. (b) Resulting dry frame elastic moduli for the fracture material based on the dynamic (red) and static (blue) compliance data, $\frac{\eta_N}{\eta_S} = 0.35$, and the fracture length and aperture relationship of Equation 4.1.

Table 4.2: Properties of fractures depending on their length according to the empirical relationships derived in this work.

Property/Length	0.01 m	0.1 m	1 m
Aperture [mm]	0.008	0.245	7.600
ρ_s [kg/m ³]	2700	2700	2700
K_s [GPa]	45	45	45
K^{fluid} [GPa]	2.25	2.25	2.25
η^{fluid} [Pa.s]	1e ⁻³	1e ⁻³	1e ⁻³
μ^{static} [GPa]	0.017	0.118	0.822
K_d^{static} [GPa]	0.026	0.180	1.253
$\mu^{dynamic}$ [GPa]	1.069	1.828	3.126
$K_d^{dynamic}$ [GPa]	1.629	2.786	4.764
k [μm^2]	6.4e ⁻⁶	5.8	5.3e ⁶
ϕ	0.8	0.8	0.8

interest. With this aim, we apply a series of oscillatory relaxation tests to a representative elementary volume (REV) of the medium. For the frequencies and physical properties considered, seismic attenuation and velocity dispersion due to FPD are governed by fluid pressure diffusion and we can neglect inertial terms (e.g., Rubino et al., 2013). Hence, Biot's poroelastic equations of motion (Biot, 1956a,b) reduce to the so-called consolidation equations (Biot, 1941), which, in the space-frequency domain are given by

$$\nabla \cdot \boldsymbol{\sigma} = 0, \quad (4.8)$$

$$\nabla p_f = -i\omega \frac{\eta}{\kappa} \mathbf{w}, \quad (4.9)$$

where $\boldsymbol{\sigma}$ is the total stress tensor, p_f the pore fluid pressure, η the fluid viscosity, κ the permeability, ω the angular frequency, and \mathbf{w} the relative fluid-solid displacement. These equations are coupled by the stress-strain constitutive relations (Biot, 1962)

$$\boldsymbol{\sigma} = 2\mu_m \boldsymbol{\epsilon} + \mathbf{I}(\lambda_c \nabla \cdot \mathbf{u} - \alpha M \xi), \quad (4.10)$$

$$p_f = -\alpha M \nabla \cdot \mathbf{u} + M \xi, \quad (4.11)$$

where \mathbf{I} is the identity matrix, \mathbf{u} the solid displacement, and $\xi = -\nabla \cdot \mathbf{w}$ a measure of the local change in the fluid content. The strain tensor is given by $\boldsymbol{\epsilon} = \frac{1}{2}(\nabla \mathbf{u} + (\nabla \mathbf{u})^T)$, where the superscript T denotes the transpose operator. The Biot-Willis parameter α , the inverse of the fluid storage coefficient M , and the Lamé parameter λ_c are given by

$$\alpha = 1 - \frac{K_m}{K_s}, \quad (4.12)$$

$$M = \left(\frac{\alpha - \phi}{K_s} + \frac{\phi}{K_{fluid}} \right)^{-1}, \quad (4.13)$$

and

$$\lambda_c = K_m + \alpha^2 M - \frac{2}{3} \mu_m, \quad (4.14)$$

where ϕ denotes the porosity, μ_m the shear modulus of the bulk material, which is equal to that of the dry frame, and K_{fluid} , K_s , and K_m are the bulk moduli of the fluid phase, the solid grains, and the dry matrix, respectively.

In order to obtain the effective stiffness matrix of the considered medium in two dimensions, three oscillatory relaxation tests are applied to the considered REV (Rubino et al., 2016). The first test consists of a harmonic vertical compression, which is performed by applying time-harmonic homogeneous vertical displacement of opposing directions at the top and bottom boundaries of the REV, while keeping the lateral displacement null at the lateral boundaries. The relative fluid displacement \mathbf{w} , is forced to be null in the vertical direction for the top and bottom boundaries and null in the horizontal direction for the lateral boundaries. The second test is a harmonic horizontal compression test, which consists of the application of opposing horizontal displacement at each of the lateral boundaries of the sample, while keeping the vertical displacements null at at the rest of the boundaries. Components of \mathbf{w} normal to the boundaries are null. The third and final test consists of the application of harmonic horizontal displacements of opposing directions at the top and bottom boundaries of the sample, while keeping the tangential displacements along the lateral boundaries null. As in the previous cases, the normal component of \mathbf{w} at each boundary is forced to be 0. Given that the

overall response of a heterogeneous poroelastic medium can be represented by that of an effective homogeneous viscoelastic solid (e.g., Rubino et al., 2016; Solazzi et al., 2016), the volumetric averages of stress and strain, in response to each of the three tests outlined above, can be related through an effective frequency-dependent and complex-valued stiffness matrix (Rubino et al., 2016)

$$\begin{pmatrix} \langle \sigma_{11}^k(\omega) \rangle \\ \langle \sigma_{22}^k(\omega) \rangle \\ \langle \sigma_{12}^k(\omega) \rangle \end{pmatrix} = \begin{pmatrix} C_{11}(\omega) & C_{12}(\omega) & C_{16}(\omega) \\ C_{12}(\omega) & C_{22}(\omega) & C_{26}(\omega) \\ C_{16}(\omega) & C_{26}(\omega) & C_{66}(\omega) \end{pmatrix} \begin{pmatrix} \langle \epsilon_{11}^k(\omega) \rangle \\ \langle \epsilon_{22}^k(\omega) \rangle \\ \langle 2\epsilon_{12}^k(\omega) \rangle \end{pmatrix}, \quad (4.15)$$

where $k = 1, 2, 3$ refers to three oscillatory relaxation tests, $C_{ij}(\omega)$ are the components of the stiffness matrix in Voigt notation, and $\langle \epsilon_{ij}^k(\omega) \rangle$ and $\langle \sigma_{ij}^k(\omega) \rangle$ represent the volume-averages of the strain and stress components in response to the test k , respectively. This system of equations has nine equations and six unknowns, and the best-fitting values of $C_{ij}(\omega)$ are obtained by a least squares algorithm, using the averaged stress and strain fields obtained from the three tests for each frequency. The resulting phase velocities and inverse quality factors are (Rubino et al., 2016)

$$V_{P,S}(\omega, \theta) = \frac{\omega}{\Re(\tilde{\nu}_{P,S}(\omega, \theta))}, \quad (4.16)$$

$$Q_{P,S}^{-1}(\omega, \theta) = -\frac{\Im(\tilde{\nu}_{P,S}(\omega, \theta)^2)}{\Re(\tilde{\nu}_{P,S}(\omega, \theta)^2)}, \quad (4.17)$$

where \Re and \Im denote the real and imaginary parts, respectively, and $\tilde{\nu}_{P,S}(\omega, \theta)$ are the complex-valued wavenumbers obtained by solving the elastodynamic

equation in a medium defined by the effective stiffness matrix. The detailed procedure required to obtain the coefficients of the stiffness matrix and the phase velocities and attenuation are detailed in the work of Rubino et al. (2016).

4.5 Seismic Signatures of Formations Containing Fractures With Correlated Properties

4.5.1 Samples With Isolated Fractures

The starting point to analyze the effects that fractures with correlated properties have on the seismic response of fractured formations is considering the case of isolated fractures, that is, fractures that are not connected to others. In this situation, the only FPD process that can affect the seismic response is FB-FPD. In order to explore how fracture scaling properties affect the characteristics of body waves, we apply the numerical upscaling procedure to REV's containing a single fracture of varying length. In order to perform controlled comparisons, we consider REV's that share a common areal fracture density, defined as the ratio of fracture area and the total area of the REV. We also compare the results with those corresponding to cases where fracture length variations are modelled without considering that the aperture, permeability, and compliance of fractures are linked to their length.

To do this, we consider a series of REV's of granitic rock, whose properties correspond to those listed in Table 4.1. The samples contain 1 horizontal fracture with a length L which is positioned centrally. The samples' side length vary according to the fracture length and aperture in order to generate samples with the same fracture density. We first consider a rectangular REV with a height of 20 cm and a width of 40 cm, containing a horizontal fracture with a length of 10 cm. We then consider samples with fractures of 1 cm and 1 m length, choosing the side lengths of the REV's such that the fracture density remains constant and keeping the ratio between the sides unchanged (Figure 4.3). In each case, we consider four scenarios for the fracture properties. In the first one, we consider that fracture properties scale with fracture length, employing K_d and μ corresponding to static compliances. For the second case, we consider that fracture properties are independent of fracture length, and correspond to those of fractures with a length of 10 cm according to the previous length scaling case. These cases are then repeated considering values of K_d and μ corresponding to dynamic compliances.

Figure 4.4 shows the phase velocity and inverse quality factor for P-waves propagating perpendicularly to a set of horizontal equal fractures with length-scaling properties corresponding to static compliance values. In Figure 4.4a, we observe that for the whole range of frequencies, longer fractures produce higher P-wave velocities than shorter ones, and that the differences become more important for frequencies below the transition frequency of

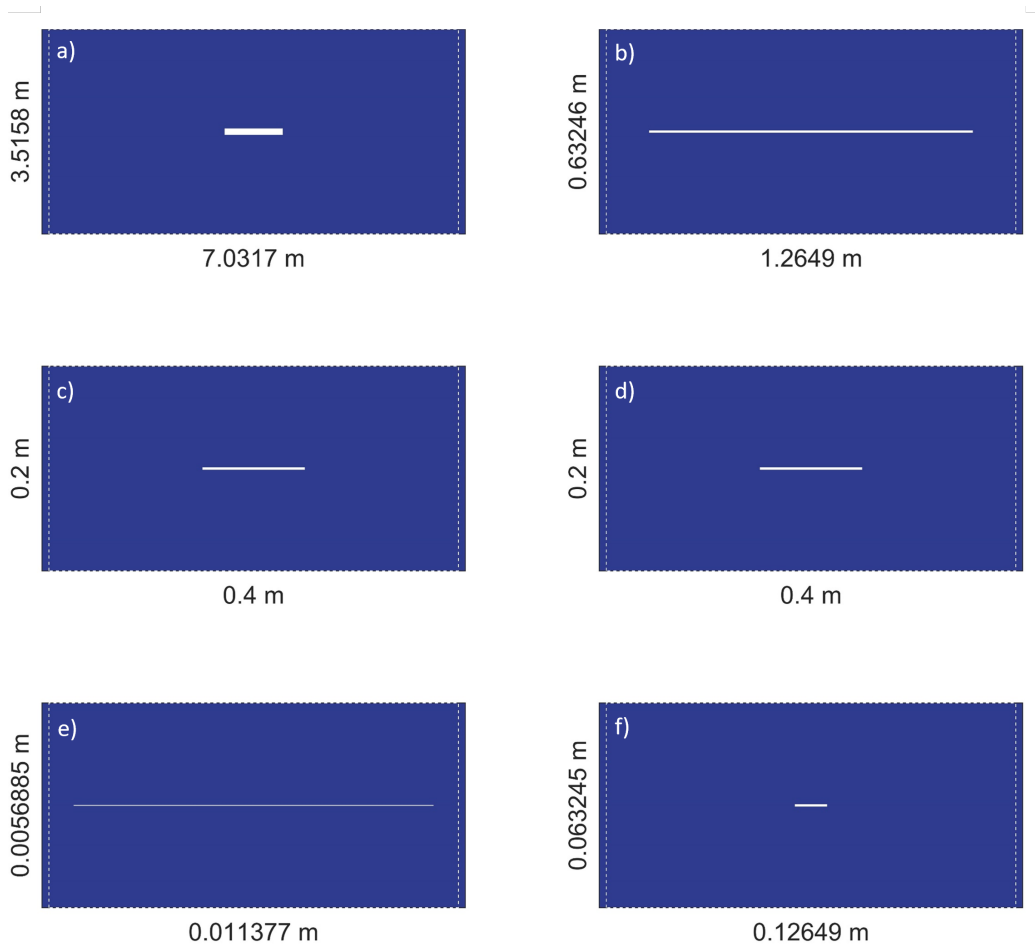


Figure 4.3: Schematic representation of the dimensions of the samples corresponding to isolated fractures of (a, b) 1, (c, d) 0.1 and (e, f) 0.01 m that (a, c, e) obey length-dependent scaling properties or (b, d, f) have constant aperture, corresponding to the properties of fractures of 10 cm in length from the length-scaling case. The samples share the same fracture density.

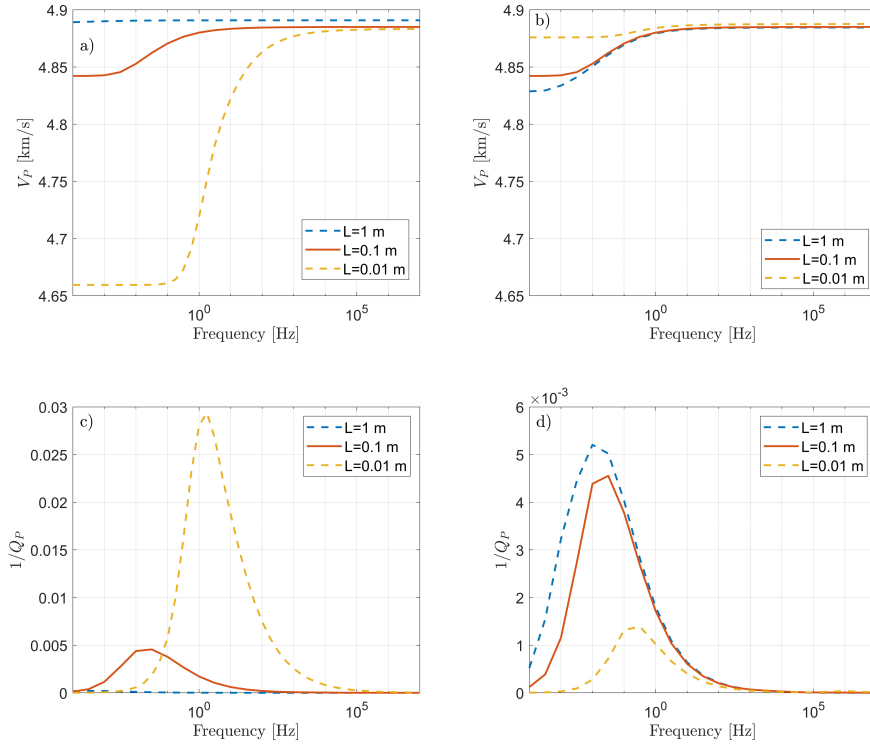


Figure 4.4: Seismic responses obtained using REV's containing 1 horizontal fracture of varying length but constant areal fracture density. (a) Vertical P-wave velocity and (c) inverse quality factor for fractures that obey length-dependent scaling properties corresponding to static compliances. (b) Vertical P-wave velocity and (d) inverse quality factor for fractures that have constant aperture, permeability, and compliance, corresponding to the properties of fractures of 10 cm in length from the length-scaling case. Note that the continuous red lines correspond to identical values of P-wave velocity and inverse quality factor across the different scenarios.

FB-FPD. The magnitude of the velocity dispersion is rather negligible for a fracture length of 1 m but it increases significantly as the fractures get shorter. This behaviour is due to the fact that smaller fractures are characterized by lower dry-frame elastic moduli (Figure 4.2) when considering length-dependent properties. This does not only produce a velocity decrease, but also an increase in the mechanical contrast between fractures and background, and, consequently, it also increases the magnitude of FPD effects. Indeed, we observe in Figure 4.4c that P-wave attenuation increases as fractures get shorter. We also observe that the transition frequency of FB-FPD shifts towards higher frequencies as the fracture length decreases. This behavior is expected, as this transition frequency is inversely proportional to the square of the fracture length (Guo et al., 2017).

Figure 4.4b shows the P-wave velocity for samples containing isolated fractures with constant aperture, compliance and permeability. We observe in this case that the relative position of velocities is inverted with respect to the length-scaling case, with longer fractures corresponding to lower velocities. We also observe that both the P-wave attenuation and the velocity dispersion are reduced with respect to the length-scaling case. In particular, we observe that, as opposed to the length-scaling properties case, P-wave attenuation is more significant for longer fractures. Figure 4.4d also shows that the transition frequency of the FB-FPD process changes. For the case of $L=0.01$ m, we observe that FB-FPD transition frequency moves towards lower frequencies than in the length-scaling case. While the scale of the

graphic does not allow to fully appreciate it, the effect is reversed in the case of $L=1$ m. This effect can, however, be clearly discerned in Figure 4.5 for REVs containing fractures with elastic moduli derived from dynamic compliance values. These are interesting results, as they show that the transition frequency of FB-FPD is also affected by other changes in fracture properties, which explains the different frequencies of the attenuation peaks in Figures 4.4c and 4.4d. Overall, this analysis shows that, for identical fracture distributions and for a constant areal fracture density, the impact on P-wave velocity and attenuation due to FB-FPD effects is more significant for shorter fractures when realistic fracture-scaling characteristics are accounted for. Most importantly, this also suggests that shorter fractures tend to control the seismic characteristics of fractured formations.

Figure 4.5 shows the P-wave velocity and inverse quality factor corresponding to fractures whose elastic properties are determined by employing dynamic compliance values. We observe that, in this case the P-wave attenuation and velocity dispersion due to FB-FPD turns out to be negligible. This is due to the fact that employing dynamic compliances results in higher values of the dry frame elastic moduli for the fractures (Figure 4.2b), thus, reducing the mechanical contrast between background and fractures. Despite the change in magnitude, we observe that the general characteristics of the behaviour of attenuation with respect to the scenario of static compliances is maintained. Figure 4.5d shows a particularity, in the form of a second attenuation peak of very low magnitude for the case of samples with fracture

lengths of 1 cm. This attenuation peak is caused by internal fluid pressure diffusion due to pressure accumulation at the ends of the rectangular fracture. An analysis employing an elliptical fracture with identical properties and whose axis corresponds to the aperture and length of the rectangular fracture does not present this effect, thus, suggesting that it is exclusively due to the shape of the fracture. The comparison of the seismic response of formations with fractures whose elastic moduli were calculated using dynamic and static compliance values illustrates the importance of the adequate estimation of compliance in order to perform modelling, as the impact of FPD effects on the seismic response of a formation may range from significant to negligible depending on the choice of compliance.

4.5.2 Samples With Connected Fractures

It is also of interest to analyze the impact that correlated fracture properties have in scenarios where fracture connectivity is present. We begin with an analysis of a series of samples that contain orthogonal intersecting fractures. In this case, the models consist of square granitic samples that are characterized by a constant areal fracture density and whose properties correspond to those of Table 4.1. The REVs contain two fractures of length L , one oriented in the vertical direction and the other in the horizontal direction. The fractures' centers coincide with the center of the REV. We compute the seismic wave velocity and attenuation employing REVs containing fractures with lengths of 1, 0.1 and 0.01 m. For fractures with $L=0.1$ m, the sample

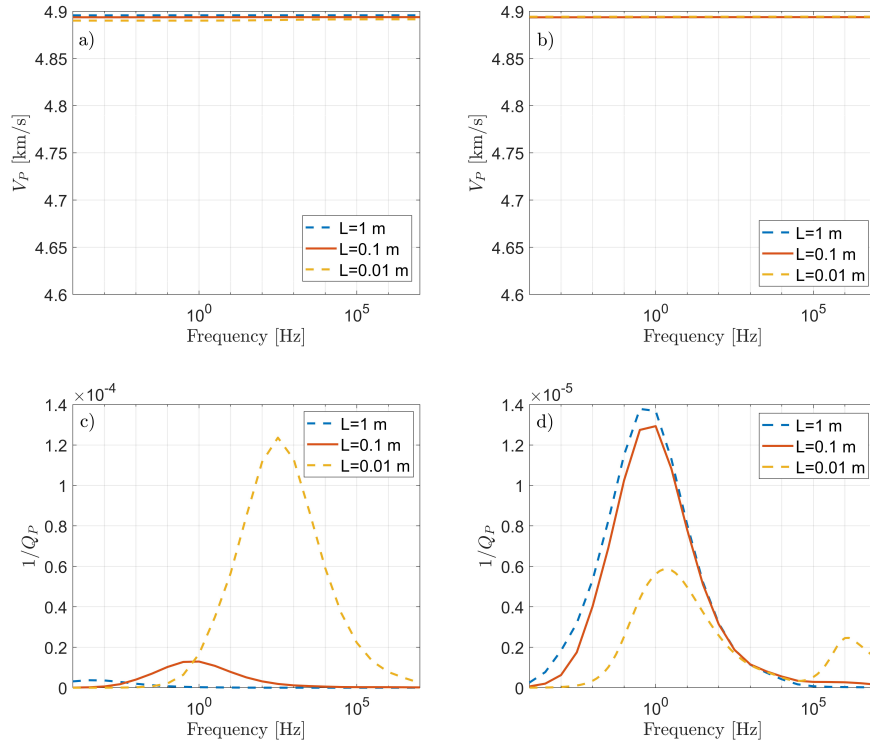


Figure 4.5: Seismic responses obtained using REV models containing 1 horizontal fracture of varying length but constant areal fracture density. (a) Vertical P-wave velocity and (c) inverse quality factor for fractures that obey length-dependent scaling properties corresponding to dynamic compliances. (b) Vertical P-wave velocity and (d) inverse quality factor for fractures that have constant aperture, permeability, and compliance, corresponding to the properties of fractures of 10 cm in length from the length-scaling case. Note that the continuous red lines correspond to identical values of P-wave velocity and inverse quality factor across the different scenarios.

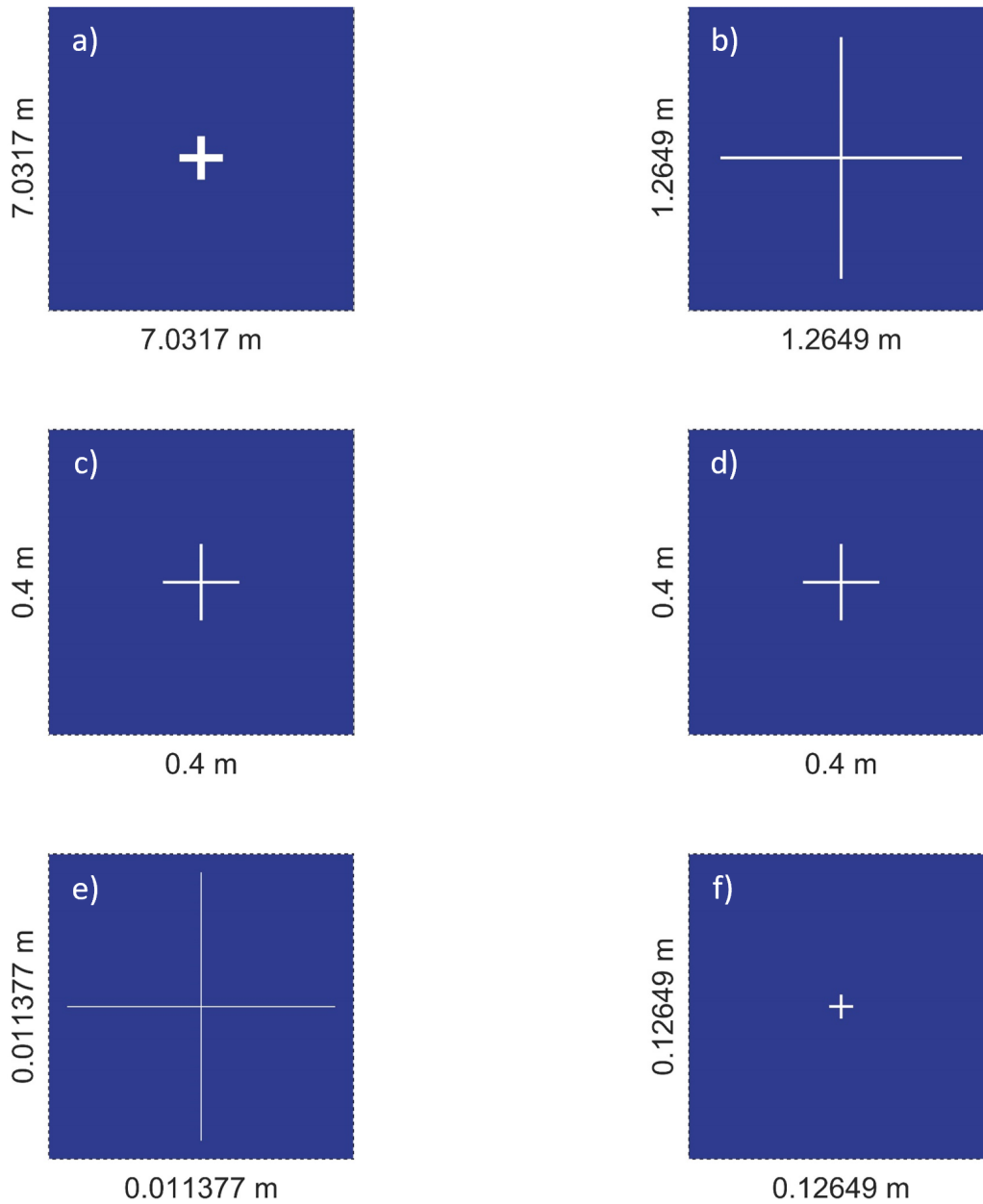


Figure 4.6: Schematic representation of the dimensions of the samples corresponding to connected fractures of (a, b) 1, (c, d) 0.1 and (e, f) 0.01 m that (a, c, e) obey length-dependent scaling properties or (b, d, f) have constant aperture, corresponding to the properties of fractures of 10 cm in length from the length-scaling case. The samples share the same fracture density.

has a side length of 0.4 m, whereas in other cases the REV side length is chosen to retain the same areal fracture density. As in the previous section, we consider cases with fracture properties scaling with length, as shown in Table 4.2, and cases where the fracture properties are independent of length and correspond to those of fractures with an intermediate length of 0.1 m in the Table 4.2.

Figure 4.7 shows the P-wave velocity and inverse quality factor for wave propagation in the vertical direction computed using REVs containing fractures whose dry-frame elastic moduli are obtained from static compliance values. In these figures, we observe, for REVs containing fractures with length $L=0.1$ m, the existence of two instances of high attenuation and dispersion, one corresponding to FB-FPD (lower frequencies) and one corresponding to FF-FPD (higher frequencies). The behaviour of the transition frequency of FB-FPD is identical to the scenario of isolated fractures, that is, it shifts to higher frequencies as the fractures get shorter. For the case of FF-FPD, on the other hand, the transition frequency is expected to be proportional to the permeability of the fractures and inversely proportional to the square of fracture length (Rubino et al., 2014). As permeability is inversely correlated with fracture length, these two effects compete with each other, but the effect of permeability dominates the transition frequency in our simulations. This can be verified by noting that the FF-FPD attenuation peaks shift towards lower frequencies as fractures get shorter. This behavior is in contrast to what the literature suggests.

Figure 4.7c also shows that the attenuation corresponding to fractures with a length of 1 m is negligible, due to their high dry-frame elastic moduli (Figure 4.2). Finally, the scenario of the REV containing fractures with a length of 1 cm is particular. Here, the combined effect of the higher transition frequency for FB-FPD and lower transition frequency for FF-FPD results in a single, prominent attenuation peak, which is located in the typical seismic frequency range. The high magnitude of this attenuation peak is also in response to the increased mechanical contrast due to the length-correlated properties of the fractures (Figure 4.2). Figure 4.7a shows that P-wave velocities are higher for longer fractures. The differences between the velocities for different fracture lengths are minimum for higher frequencies, when the REVs are in an unrelaxed state with respect to FB- and FF-FPD. This behaviour is similar to the behaviour of isolated fractures in the previous section.

The case of fractures with constant properties shows significant differences with respect to dispersion and attenuation. In Figure 4.7b, we can observe that the overall dispersion level of the REVs containing fractures with lengths of 1 m and 0.01 m are comparable with the dispersion of REVs containing fractures with a length of 0.1 m. This is due to the fact that homogeneous fractures share the same elastic moduli, which, in turn, illustrates the control that compliance has over the amplitude of seismic attenuation and dispersion. We also observe that dispersion is more significant for longer fractures as compared to shorter ones. Moreover, Figure 4.7b shows that the placement of the FB-FPD transition frequency is similar to the case of isolated

fractures with constant properties. Analyzing the placement of the FF-FPD attenuation peaks, we observe that longer fractures are associated with lower frequencies while shorter fractures have higher transition frequencies. This behaviour is opposite to what is observed in the length-scaling case, which is due to the fact that the fractures have the same permeability regardless of their length. Without the effect of permeability, the dependence of the FF-FPD transition frequency with the inverse of the square of the fracture length controls the frequency of the attenuation peak, thus, resulting in the effects observed here. It is also important to note that this effect causes the separation of the dispersion peaks for fractures with a length of 1 cm, which causes the expected on the seismic frequency range to be significantly reduced when compared to the attenuation predicted in the length-dependent case. Consequently, employing constant fracture properties may lead to incorrectly predict negligible dispersion for the seismic frequency range, which can affect the interpretation of seismic data.

Figure 4.8 shows the P-wave velocity and inverse quality factor computed using REV's containing fractures whose elastic moduli are obtained employing dynamic compliance estimates. Although the general behavior is very similar to the case based on static compliance values the resulting dispersion and attenuation due to FPD effects turn out to be negligible. This is due to the high dry-frame elastic moduli of the fracture material derived from the dynamic compliance values. The reduced mechanical contrast with respect to the background diminishes the FPD effects.

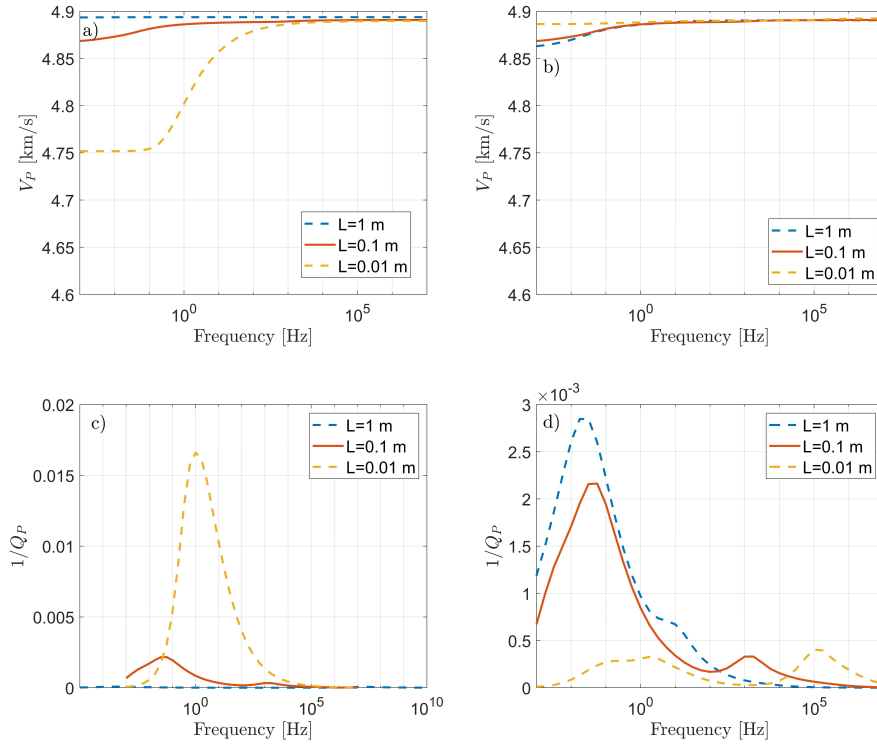


Figure 4.7: Seismic responses obtained using REV's containing orthogonal connected fractures of varying length with constant areal fracture density. (a) Vertical P-wave velocity and (c) inverse quality factor for fractures that obey length-dependent scaling properties corresponding to static compliances. (b) Vertical P-wave velocity and (d) inverse quality factor for fractures that have constant aperture, permeability, and compliance, corresponding to the properties of fractures with a length of 10 cm from the length-scaling case. Note that the continuous red lines correspond to identical values of P-wave velocity and inverse quality factor across the different scenarios.

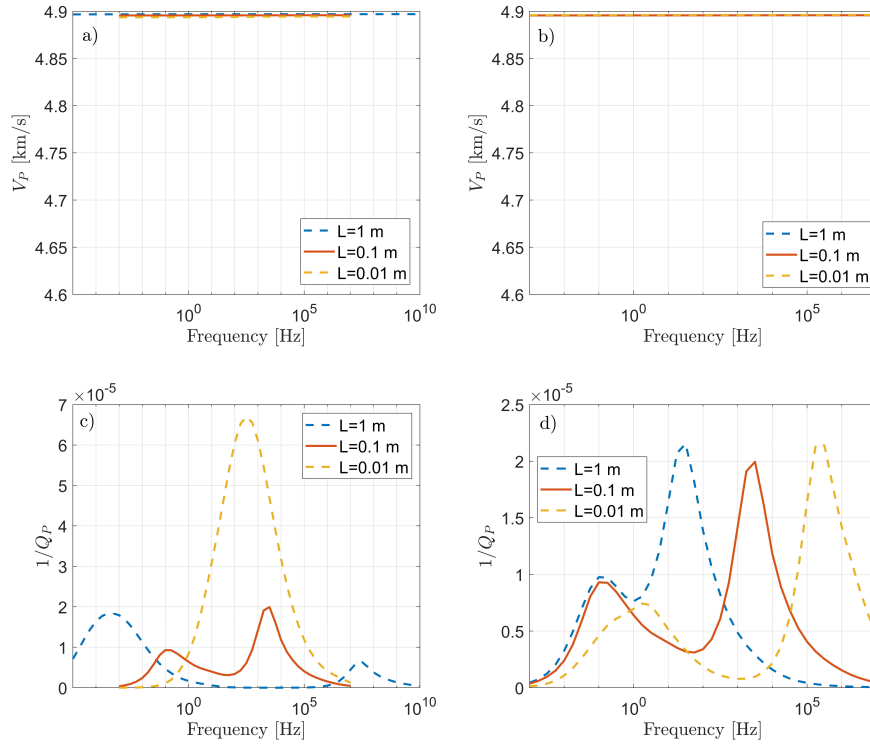


Figure 4.8: Seismic responses obtained using REV's containing orthogonal connected fractures of varying length with constant areal fracture density. (a) Vertical P-wave velocity and (c) inverse quality factor for fractures that obey length-dependent scaling properties corresponding to dynamic compliances. (b) Vertical P-wave velocity and (d) inverse quality factor for fractures that have constant aperture, permeability, and compliance, corresponding to the properties of fractures of 10 cm in length from the length-scaling case. Note that the continuous red lines correspond to identical values of P-wave velocity and inverse quality factor across the different scenarios.

The fracture density corresponding to the REVs considered in the previous analyses was kept constant in order to be able to compare the different scales of fractures considering a constant areal fracture density. In order to analyze the impact of the value of fracture density in the seismic response of the formations, we now compute the seismic response of a series of square REVs containing orthogonal connected fractures with a length of 0.1 m. The side length of the different REVs varies to generate different areal fracture densities. The base case corresponds to a REV with a side length of 0.4 m and the subsequent cases correspond to REVs with 5 and 10 times the fracture density of the base case. The fracture density corresponding to these cases is of approximately 0.03% for the base case, and 0.15% and 0.3% for the other two cases.

Figure 4.9 shows the the P-wave velocity and inverse quality factor obtained using REVs containing fractures whose elastic moduli correspond to static (Figures 4.9a and c) and dynamic (Figure 4.9 b and d) compliance estimations. In the first case, higher fracture densities are associated with lower P-wave velocities and higher levels of velocity dispersion. We observe that the magnitudes of the attenuation peaks increase approximately proportionally with regard to the increase in areal fracture density. We do not notice any associated changes in the shape or position of the peaks. On the other hand, we observe that for the case of fractures whose elastic moduli are derived from dynamic compliance measurements (Figure 4.9b and 4.9d), seismic attenuation and dispersion remain negligible despite the order-of-

magnitude increases of fracture density. This illustrates the importance of properly choosing the mechanical properties of fractures.

4.5.3 Impact of Fracture Density Definitions

In the preceding analysis, we considered comparisons between REVs that share the same areal fracture density, which is defined as the ratio of fracture area over the total area of the sample. We considered this approach, introduced by Hunziker et al. (2018), as the value obtained is representative of the impact that fractures have on the seismic response of the modelled formations. However, it is common in the literature to employ another definition of fracture density, given by the ratio between the sum of the lengths of all fractures in a sample and the total sample area (e.g., Bonnet et al., 2001; de Dreuzy et al., 2001; Lei and Sornette, 2021). The difference between these definitions of fracture density consists in that the first accounts for the apertures while the second does not.

One inherent problem of fracture density is the fact that a scalar value cannot provide information about the length or spatial distribution of fractures in a sample. As shown previously, the length distribution of fractures has a significant impact on the seismic response of a fractured rock. In the case that fractures are modelled considering that their properties are constant and independent of length, there is no significant difference between the two. However, in cases where fracture aperture is dependent on length, it is possible to analyze the characteristics of the seismic responses using

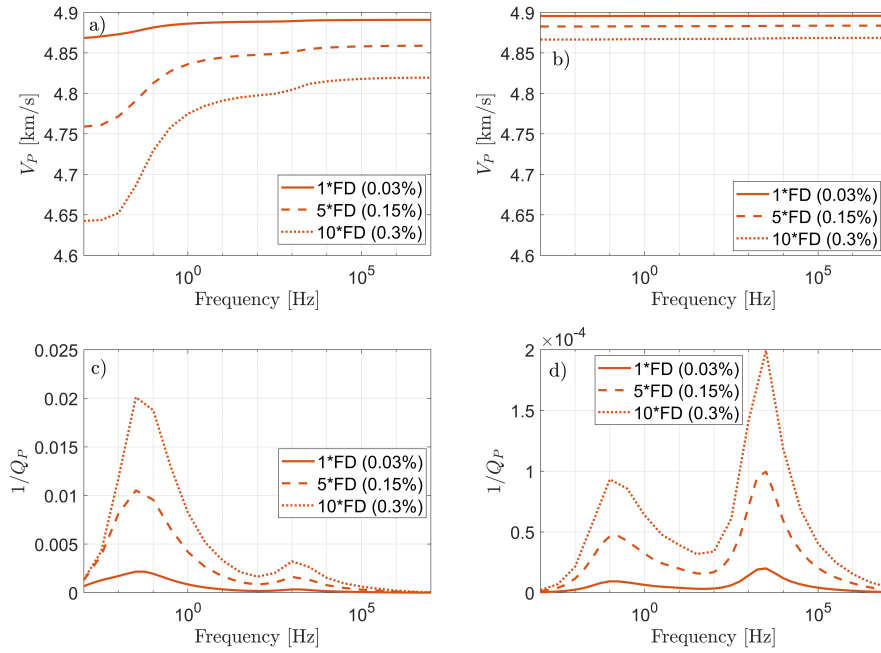


Figure 4.9: Seismic responses obtained using REV models containing orthogonal connected fractures with $L=0.1$ m with varying areal fracture density. (a) Vertical P-wave velocity and (c) inverse quality factor for fractures that obey length-dependent scaling properties corresponding to static compliances. (b) Vertical P-wave velocity and (d) inverse quality factor for fractures that obey length-dependent scaling properties corresponding to dynamic compliances. Note that the continuous red lines correspond to identical values of P-wave velocity and inverse quality factor across the different scenarios.

REVs that share either areal or linear fracture density. The objective of this comparison is to determine which approach is more representative of the impact that a fracture network has on the seismic response.

To perform this comparison, we consider formations containing isolated or connected fractures of equal length divided in two scenarios. In the first scenario, we consider REVs that have the same areal fracture density, while in the second we consider REVs that have the same linear fracture density. The reference sample for isolated fractures consists of a rectangular sample with a width of 0.4 m and a height of 0.2 m containing a horizontal fracture with a length $L=0.1$ m, located at the center of the REV. The base sample for connected fractures consist of a square sample of side length of 0.4 m, containing a vertical and a horizontal fracture with a length $L=0.1$ m each, intersecting at the center of the REV. The samples corresponding to fractures with different lengths have the same aspect ratio as the reference sample in each case with their side lengths adjusted to obtain the desired fracture density value. For brevity, we consider only samples containing fractures whose elastic moduli are derived employing static compliance values, as the values of dispersion and attenuation corresponding to dynamic compliance values turned out to be negligible.

Figure 4.10 shows the seismic responses obtained using REVs containing an isolated horizontal fracture with (Figures 4.10a and 4.10c) constant areal fracture density or (Figures 4.10b and 4.10d) constant linear fracture density. We observe that the results differ significantly. In the case of constant areal

fracture density, longer fractures are associated with higher elastic moduli and, therefore, attenuation and dispersion effects diminish. In the constant linear fracture density scenario, the behavior is opposite. We observe that longer fractures are associated with higher levels of dispersion and attenuation, despite the fractures having the same properties as in the constant areal fracture density scenario. This is because the total area of the fractures in the constant linear fracture scenario is variable. In the case of samples containing fractures with $L=1$ m, the ratio between fracture area and sample area is ~ 30 times larger than in the constant areal fracture density scenario. Conversely, in the case of samples containing fracture with $L=0.01$ m the fracture area over sample area ratio is 30 times less than in the constant fracture area scenario. The results show that these discrepancies in the fracture area ratio of the samples are more important for attenuation and dispersion effects than the changes in elastic moduli. We also observe that in the case of constant areal fracture density, the P-wave velocity increases for longer fractures and that, for the high-frequency limit, the velocities for the different fracture lengths converge. In the constant linear fracture density case, on the other hand, we observe the opposite behavior and the different scenarios do not converge in the high-frequency limit. This demonstrates that areal fracture density might be a more consistent estimator of the impact of fractures on the seismic response of the medium than its counterpart.

Figure 4.11 shows the P-wave velocity and inverse quality factor for samples containing one horizontal and one vertical connected fractures of the

same length. The samples share (Figures 4.11a and 4.11c) the same areal fracture density and (Figures 4.11b and 4.11c) the same linear fracture density. These results show identical characteristics as the previous analysis on isolated fractures. In the case of constant linear fracture density, we observe that longer fractures are associated with lower P-wave velocities and higher levels of attenuation and velocity dispersion, whereas the other case shows the opposite. And finally, in contrast to constant linear fracture density, common areal fracture density samples are associated with very similar P-wave velocities for high frequencies, thus confirming our previous interpretations. It is also worth considering that, if we assume that the porosity of the fractures is constant with length, the total fracture pore volume of samples with the same areal fracture density is constant, while this is not the case for samples that share the same linear fracture density.

4.6 Discussion

In this work, we have explored the seismic response of REV's containing fractures whose properties were derived from empirical relationships accounting for the fact that aperture, permeability, and compliance are dependent on fracture length. While there is plenty of evidence in the literature that these properties are indeed related to length, the particular model they follow is not trivial to determine. The properties of fractures can vary depending on the type of embedding rock, the prevailing lithostatic pressure, the stress conditions present at the time of their formation, weathering, and so on. Our

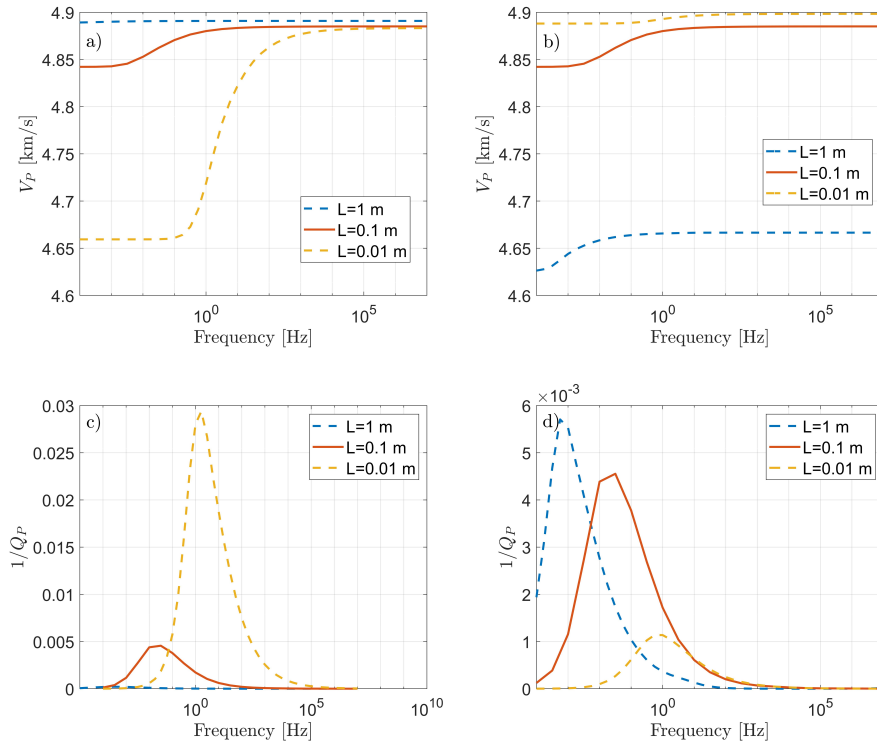


Figure 4.10: Seismic responses obtained using REVs with one horizontal fracture of varying length characterized by length-scaling properties based on static compliance estimates. (a) P-wave velocity and (c) inverse quality factor for vertical propagation and samples that share a constant areal fracture density. (b) P-wave velocity and (d) inverse quality factor for samples that share a constant linear fracture density. Note that the continuous red lines correspond to identical values of P-wave velocity and inverse quality factor across the different scenarios.

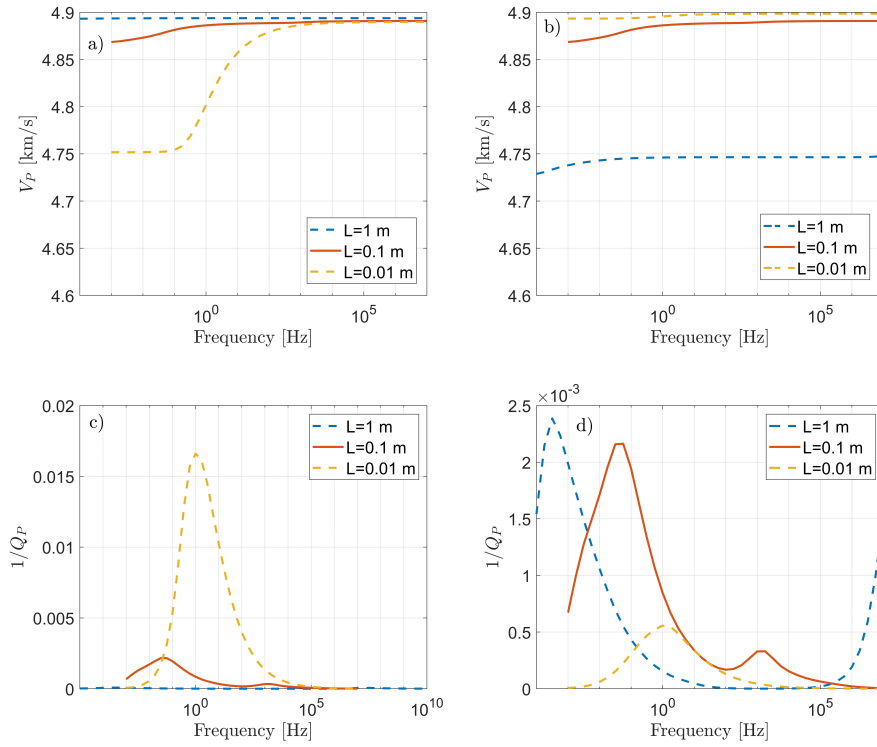


Figure 4.11: Seismic responses obtained using REV models with two orthogonally intersecting fractures of varying length characterized by length-scaling properties based on static compliance estimates. (a) Vertical P-wave velocity and (c) inverse quality factor for samples that share a constant areal fracture density. (b) Vertical P-wave velocity and (d) inverse quality factor for samples that share a constant linear fracture density. Note that the continuous red lines correspond to identical values of P-wave velocity and inverse quality factor across the different scenarios.

results and interpretations are based on careful selection of published data, but are nevertheless only first-order approximations.

When determining the elastic moduli of the porous material representing the fractures, we consider a power-law-type relationship of fracture length and aperture, and the corresponding compliance estimations. As mentioned before, the values of fracture length and compliance obtained from the literature are inherently uncertain, as the determination of the quantity and length of fractures in the field is challenging. When considering these relationships together, we obtain values of elastic moduli that have the particularity of being higher as fracture length increases. This has direct bearing on our results as we see that the dry frame elastic moduli of fractures controls the amount of dispersion and attenuation of the fractured material. Even when considering that the values of compliance shown here are generally valid, fracture length and aperture relationships are very variable (e.g, Bonnet et al., 2001; Vermilye and Scholz, 1995), even making it possible for the elastic moduli to decrease with length. This highlights the importance of determining, whenever possible, locally-adjusted models for the length-scaling relationships, employing data that corresponds to the conditions and lithology of the site of interest.

4.7 Conclusions

In this study, we utilized published datasets to establish empirical relationships between fracture aperture, permeability, and compliance as functions of

fracture length. These relationships were then employed to model the seismic responses of formations containing networks of isolated and connected fractures with lengths of 1, 0.1, and 0.01 meters. To facilitate comparisons, we considered fractured formations with constant areal fracture density, which, as demonstrated in this work, is a more reliable estimator than the more commonly used fracture density definition based on the cumulative length of fractures per area unit.

Our findings reveal that formations containing shorter fractures exhibit lower P-wave velocities and significantly higher attenuation and dispersion compared to longer fractures. This behavior is attributed to the lower dry-frame elastic moduli of shorter fractures as a consequence of the considered length-dependent fracture properties. In contrast to what the available literature suggests, the transition frequency corresponding to FF-FPD decreases as fractures shorten. This is due to the fact that the reduction of permeability associated with shorter fractures prevails over the predicted increase of transition frequency due to the reduction of fracture length. This effect, compounded with a increase of the FB-FPD transition frequency as fractures become shorter, leads to a noteworthy reduction of the width of the so-called non-dispersive plateau, to the extent of its disappearance in the case of formations containing 1 cm fractures.

Simulations assuming constant aperture, permeability, and compliance fail to capture these crucial characteristics. Instead, they incorrectly link longer fractures with increased dispersion and attenuation and fail to accu-

rately represent the position of the attenuation peaks. These conclusions were drawn from analyses based on compliance estimates obtained through dynamic and static measurements. However, it is important to note that dynamic compliance values resulted in largely negligible dispersion and attenuation, thus, limiting their interpretive scope. This, along with the inherent variability and uncertainty present in fracture property data, points to the importance of further exploring and improving the calibration of the relationships between mechanical properties of the fractures and length.

Chapter 5

Conclusions and Outlook

5.1 Summary and Conclusions

The work done in this thesis illustrates the potential of poroelastic modelling to improve the interpretation of seismic surveys, with a particular focus on the monitoring and characterization of fractured geothermal reservoirs. It was shown that FPD effects are prevalent in porous, fractured, fluid-saturated formations and that their impact varies according to different properties of the probed fracture network and the embedding background. In particular, the role played by key parameters that are of importance for the exploitation of geothermal resources was quantitatively explored, providing the necessary methodological frameworks to recreate the analyses, in order to encourage the use of poroelastic modelling in corresponding interpretation workflows. In the following, I summarize and discuss the results of the works described in Chapters 2, 3, and 4, with a focus on the impact of these

contributions as a whole.

In the first work (Chapter 2), I explored the impact of FPD effects on the seismic response in the presence of fracture networks with varying fracture density, interconnectivity, and length distribution. This analysis was performed in the context of a fractured geothermal reservoir in a crystalline rock, considering the potential effects of FPD on body wave velocities and Rayleigh wave dispersion curves. The results showed that both body wave velocities and Rayleigh wave dispersion are sensitive to the degree of fracture interconnectivity and fracture density. In particular, the analysis indicates that Rayleigh wave velocity changes, which so far have commonly been associated with fracture density changes, can be explained by changes in interconnectivity of preexisting or newly generated fractures. Comparing the results with those based on an elastic approach neglecting FPD effects reveals that the latter fails to account for the influence of fracture interconnectivity. This is due to the fact that, contrary to poroelastic approaches, elastic frameworks cannot properly account for the reduction of the stiffening effect of the fluid contained in connected fractures with different orientations in response to wave-induced FPD. The analysis presented in Chapter 2 sheds light on the importance of accounting for FPD effects in geothermal reservoir modelling and provides tools to assist the qualitative interpretation of seismic data.

In the second work of this thesis (Chapter 3), I considered the impact that steam saturation may have on the seismic response of fractured formations in a geothermal context. For this, I modelled fracture networks with

realistic fracture length distributions, considering completely connected, randomly connected, and unconnected fractures. I employed realistic physical properties for water and vapor, according to the pressure and temperatures conditions. A sensitivity analysis was performed, considering varying levels of steam saturation on the fractures. For this, I assumed that the fractures could be completely saturated with either water or steam, and that steam saturated longer fractures preferentially, until the desired steam saturation was achieved. I analyzed first the behavior of body wave velocities, considering steam saturation values from 0 to the totality of the fracture pore space. The results showed that P-wave velocity is more sensitive than S-wave velocity to changes in the steam saturation of the fractures. Comparisons with corresponding elastic approaches showed that the effects of steam saturation in formations containing interconnected fractures cannot be properly modelled unless FPD effects are adequately taken into account. The results obtained motivated the comparison of the seismic properties of formations containing fracture networks with varying steam saturation with those corresponding to formations containing fracture networks with varying fracture density. This comparison showed that as steam saturation changes and fracture density variations cause similar changes of P-wave velocities, whereas the impact on S-wave velocities are very different. These two scenarios could therefore be discriminated through a V_P vs V_P/V_S analysis. This is an important result that has the potential to be a valuable tool in the interpretation of seismic data from fractured formations in the presence of gaseous phases.

This analysis was then extended to explore the corresponding impact on Rayleigh wave dispersion and seismic reflection amplitude vs angle (AVA). The results showed that Rayleigh-based techniques are much less sensitive to fluid saturation changes than to fracture density variations. Moreover, the impact of steam saturation changes on the Rayleigh wave velocity obtained from an elastic approach resulted significantly higher than when employing a poroelastic approach, which would result in erroneous interpretations of seismic data. Finally, for the case of AVA analyses, I performed inversion of synthetic reflection coefficients considering two different AVA linear approximations. The results demonstrate that AVA curves are sensitive to steam saturation changes, and corresponding analyses have the potential to discriminate between variations of fracture density and steam saturation as the source of changes in the seismic response of the formation. This kind of analysis does, however, rely on having sufficient angle coverage in the seismic data in order to be able to appropriately invert for S-wave-dependent parameters in the AVA approximations. In circumstances where the angle coverage only allows to derive information of the P-wave velocity of the formation, the corresponding results could be employed alongside Rayleigh wave dispersion data to identify the cause of changes in velocity.

For the third and last project (Chapter 4), the detailed characteristics of the poroelastic representation of fractures previously employed in our models were revisited, focusing on improving the realism of the modelled seismic response of fractured formations. For this, empirical relationships were derived

employing existing datasets from the literature to determine the dependency of fracture aperture, permeability, and compliance with regard to fracture length. The impact on the characteristics of seismic waves of this correlation of fracture properties with length was then explored for isolated and connected fractures in the centimeter, decimeter and meter scale, and their seismic responses were compared with those obtained considering aperture, permeability, and compliance being independent from fracture length.

The results demonstrate that for both connected and unconnected fractures, and considering formations with the same areal fracture density, seismic waves are characterized by lower velocities and higher levels of attenuation and dispersion in the presence of shorter fractures compared to longer ones. These characteristics are due to the fact that, according to the derived fracture aperture and compliance relationships with fracture length, shorter fractures are characterized by lower dry-frame elastic moduli. This, in turn, suggests that shorter fractures tend to control the seismic response of fractured rocks. These important characteristics are not accounted for when considering fracture properties constant with regard to fracture length, where longer fractures are associated with lower velocities and higher attenuation levels.

In the case of connected fractures with correlated properties, it was shown that the transition frequency of FF-FPD shifts to lower frequencies as fracture length decreases. This behavior is in disagreement with previous results that predict a shift to higher frequencies instead, due to the fact that this

frequency is inversely proportional to the square of the fractures' length (Guo et al., 2017). However, the transition frequency is also directly proportional to the permeability of the fractures and, as fractures become shorter, the reduction of permeability considered in the model with correlated fracture properties overcomes the effect of length. This shift of the FF-FPD peak towards lower frequencies affects the width of the non-dispersive plateau. Indeed, this shift, in conjunction with the increase of the transition frequency of FB-FPD for shorter fractures, result in the disappearance of the non-dispersive plateau for formations containing fractures with a length of 1 cm. Conversely, employing constant fracture properties does not produce this drastic reduction of the non-dispersive zone, which could lead to erroneous predictions of the seismic attenuation properties when modelling under this simplistic assumption.

The simulations were performed considering compliance information obtained from static and dynamic measurements. It was shown that formations containing fractures with properties derived from dynamic compliance values present negligible seismic dispersion and attenuation, even in the presence of elevated values of fracture density. Conversely, formations containing fractures whose properties were derived from static compliance values showed significant dispersion and attenuation values. Finally, it was demonstrated that the definition of fracture density based on the area of the fractures in a formation instead of solely their lengths is expected to be more representative of the seismic response expected for the probed formation.

5.2 Outlook

The work presented in this thesis constitutes a first step towards the integration of poroelastic modelling into the characterization and interpretation workflows for seismic monitoring of geothermal reservoirs. Despite employing advanced modelling techniques, there are still important obstacles that impede the representation of more realistic rock models. The upscaling procedure employed in this work to obtain the seismic response of fractured formations is computationally expensive and, for this reason, it is not possible to routinely consider 3D models containing relatively complex fracture networks. It is expected that FPD effects will be diminished when considering fractures that have finite size in all directions (Hunziker et al., 2018). Furthermore, even when considering 2D samples, the nature of fracture length distributions makes it difficult to generate a sample that is large enough to be considered a REV of the fractured formation. In order to circumvent this, I employed a Monte-Carlo-type approach to obtain representative seismic properties by averaging the responses of several smaller samples. A disadvantage of this approach is that the range of variability of lengths of the fractures that can be represented is limited, which is of particular importance in light of the impact of length-correlated fracture properties.

Continuing with the topic of the representation of fracture networks, in this thesis, I performed sensitivity analyses that considered varying fracture density, connectivity, or steam saturation. However, these sensitivity analyses do not consider a realistic evolution of the explored fracture networks,

as they are simply based on new samples generated with the desired properties. Processes such as decompression, cooling, or hydraulic stimulation are expected to cause changes in a fracture network. As such, physics-based methodologies to model the evolution of fracture networks could provide valuable insights with regard to the expected seismic signatures associated with the different processes. With regards to the properties at the fracture scale, the analysis of different datasets available in the literature regarding fracture length, aperture, permeability, and compliance shows significant uncertainties that negatively affect the reliability of length-correlated fracture properties models, such as the ones presented in the third project of this thesis. Experiments that measure all these key variables, employing consistent criteria to determine length and aperture are needed in order to improve the quality of the available data.

Rubino et al. (2017) analyzed the impact of fracture connectivity on the anisotropic seismic response of fractured media. The authors found that the degree of fracture connectivity manifests itself in the form of a pronounced change of the velocity anisotropy of P- and S-waves in the seismic frequency band. This study demonstrates the potential of seismic anisotropy to be another valuable tool to constrain the degree of interconnectivity of fracture networks. This could be of particular interest for passive seismic monitoring, which is based on the inversion of surface wave dispersion curves. As these dispersion curves are controlled mainly by the S-wave velocity of the probed formation, the role played by S-wave velocity anisotropy to provide

a complementary source of information on the degree of connectivity of fractured formations, or to potentially constrain the reasons for seismic velocity changes under circumstances where only passive seismic data is available. These are important topics for future research. In particular, a comprehensive assessment of seismic anisotropy, accounting for FPD effects could help in the monitoring of hydraulic fracturing and stimulation of geothermal reservoirs, where fractures are expected to be created and fracture connectivity is expected to increase. The work of Adelinet et al. (2016) is a recent example that showcases this important interpretational objective. In this work, the authors employ an elastic modelling approach in order to aid with the interpretation of time-lapse, azimuthally variable data from stimulation procedures that took place in the Soultz-sous-Forets EGS. The seismic velocity changes are attributed to changes in the length of fractures. As has been shown in this thesis, the elastic modelling approach does not, however, have the ability to retrieve information related to the interconnectivity of fractures, a parameter that plays an important role in the overall hydraulic and seismic properties of the fractured formation. Consequently, a methodology based on poroelastic modelling of the anisotropic response of the formation could potentially improve the evaluation of the stimulation procedure, thus, allowing for identification of zones where fracture connectivity was successfully increased and those where this is not the case. This information could improve the efficiency of future stimulation efforts.

Another point of consideration should be how to improve the integration

of multi-scale approaches into characterization and interpretation workflows. As fractures span length ranges from the microscopic to the regional scale, it is difficult to address the modelling of all associated effects operating at different scales at once. It is also worth noting that different physical mechanisms may prevail at different scales, including squirt flow at the microscopic scale, FPD at the mesoscale, and, finally, scattering effects at the macroscale when the fractures are comparable in length to the wavelength of the seismic waves. One alternative could be to use effective medium approaches to characterize fractures below a certain length threshold, and use these effective properties to represent the background embedding larger fractures. This approach would have, however, the disadvantage of not being able to consider interactions between fractures that belong to different scale ranges. Specifically, addressing these interactions would then be the logical follow-up project.

REFERENCES

- Adelinet, M., Dorbath, C., Calò, M., Dorbath, L., and Le Ravalec, M. (2016). Crack features and shear-wave splitting associated with fracture extension during hydraulic stimulation of the geothermal reservoir in Soultz-sous-Forets. *Oil & Gas Science and Technology—Revue d’IFP Energies nouvelles*, 71(3):39.
- Aki, K. and Lee, W. (1976). Determination of three-dimensional velocity anomalies under a seismic array using first P arrival times from local earthquakes: 1. A homogeneous initial model. *Journal of Geophysical research*, 81(23):4381–4399.
- Aki, K. and Richards, P. G. (1980). *Quantitative Seismology: Theory and Practice*. W.H. Freeman, New York.
- Avseth, P., Mukerji, T., and Mavko, G. (2010). *Quantitative seismic interpretation: Applying rock physics tools to reduce interpretation risk*. Cambridge University Press.

- Bakku, S. K., Fehler, M., and Burns, D. (2013). Fracture compliance estimation using borehole tube waves. *Geophysics*, 78(4):D249–D260.
- Barbier, E. (2002). Geothermal energy technology and current status: an overview. *Renewable and Sustainable Energy Reviews*, 6(1-2):3–65.
- Barbosa, N. D., Caspari, E., Rubino, J. G., Greenwood, A., Baron, L., and Holliger, K. (2019). Estimation of fracture compliance from attenuation and velocity analysis of full-waveform sonic log data. *Journal of Geophysical Research: Solid Earth*, 124(3):2738–2761.
- Barton, N. (2006). *Rock quality, seismic velocity, attenuation and anisotropy*. CRC press.
- Barton, N., Bandis, S., and Bakhtar, K. (1985). Strength, deformation and conductivity coupling of rock joints. *International Journal of Rock Mechanics & Mining Sciences*, 22:121–140.
- Barton, N. and de Quadros, E. F. (1997). Joint aperture and roughness in the prediction of flow and groutability of rock masses. *International Journal of Rock Mechanics & Mining Sciences*, 34(3-4):252–e1.
- Batini, F. and Nicolich, R. (1985). P and s reflection seismic profiling and well logging in the travale geothermal field. *Geothermics*, 14(5-6):731–747.
- Biot, M. A. (1941). General theory of three-dimensional consolidation. *Journal of Applied Physics*, 12(2):155–164.

- Biot, M. A. (1956a). Theory of propagation of elastic waves in a fluid-saturated porous solid. I. Low-frequency range. *The Journal of the Acoustical Society of America*, 28(2):168–178.
- Biot, M. A. (1956b). Theory of propagation of elastic waves in a fluid-saturated porous solid. II. Higher frequency range. *The Journal of the Acoustical Society of America*, 28(2):179–191.
- Biot, M. A. (1962). Mechanics of deformation and acoustic propagation in porous media. *Journal of Applied Physics*, 33(4):1482–1498.
- Bonnet, E., Bour, O., Odling, N. E., Davy, P., Main, I., Cowie, P., and Berkowitz, B. (2001). Scaling of fracture systems in geological media. *Reviews of Geophysics*, 39(3):347–383.
- Boullenger, B., Verdel, A., Paap, B., Thorbecke, J., and Draganov, D. (2015). Studying CO₂ storage with ambient-noise seismic interferometry: A combined numerical feasibility study and field-data example for Ketzin, Germany. *Geophysics*, 80(1):Q1–Q13.
- Bourbié, T., Coussy, O., and Zinszner, B. (1987). *Acoustics of porous media*. Editions TECHNIP.
- Brenguier, F., Shapiro, N. M., Campillo, M., Ferrazzini, V., Duputel, Z., Coutant, O., and Nercessian, A. (2008). Towards forecasting volcanic eruptions using seismic noise. *Nature Geoscience*, 1(2):126–130.

- Brown, S. R. (1987). Fluid flow through rock joints: the effect of surface roughness. *Journal of Geophysical Research: Solid Earth*, 92(B2):1337–1347.
- Buchen, P. and Ben-Hador, R. (1996). Free-mode surface-wave computations. *Geophysical Journal International*, 124(3):869–887.
- Calò, M., Kinnaert, X., and Dorbath, C. (2013). Procedure to construct three-dimensional models of geothermal areas using seismic noise cross-correlations: application to the Soultz-sous-Forêts enhanced geothermal site. *Geophysical Journal International*, 194(3):1893–1899.
- Campillo, M. and Paul, A. (2003). Long-range correlations in the diffuse seismic coda. *Science*, 299(5606):547–549.
- Casini, M., Ciuffi, S., Fiordelisi, A., Mazzotti, A., and Stucchi, E. (2010). Results of a 3d seismic survey at the travale (italy) test site. *Geothermics*, 39(1):4–12.
- Caspari, E., Milani, M., Rubino, J. G., Müller, T. M., Quintal, B., and Holliger, K. (2016). Numerical upscaling of frequency-dependent P-and S-wave moduli in fractured porous media. *Geophysical Prospecting*, 64(4):1166–1179.
- Chen, Y.-F., Fang, S., Wu, D.-S., and Hu, R. (2017). Visualizing and quantifying the crossover from capillary fingering to viscous fingering in a rough fracture. *Water Resources Research*, 53(9):7756–7772.

- de Dreuzy, J.-R., Davy, P., and Bour, O. (2001). Hydraulic properties of two-dimensional random fracture networks following a power law length distribution: 1. Effective connectivity. *Water Resources Research*, 37(8):2065–2078.
- Detournay, E. and Cheng, A. H.-D. (1993). Fundamentals of poroelasticity. In Fairhurst, C., editor, *Analysis and Design Methods*, pages 113–171. Pergamon, Oxford.
- Diehl, T., Kraft, T., Kissling, E., and Wiemer, S. (2017). The induced earthquake sequence related to the st. gallen deep geothermal project (switzerland): Fault reactivation and fluid interactions imaged by microseismicity. *Journal of Geophysical Research: Solid Earth*, 122(9):7272–7290.
- Dvorkin, J., Gutierrez, M. A., and Grana, D. (2014). *Seismic reflections of rock properties*. Cambridge University Press.
- Edwards, B., Kraft, T., Cauzzi, C., Kästli, P., and Wiemer, S. (2015). Seismic monitoring and analysis of deep geothermal projects in st gallen and basel, switzerland. *Geophysical Journal International*, 201(2):1022–1039.
- Fatti, J. L., Smith, G. C., Vail, P. J., Strauss, P. J., and Levitt, P. R. (1994). Detection of gas in sandstone reservoirs using avo analysis: A 3-d seismic case history using the geostack technique. *Geophysics*, 59(9):1362–1376.
- Favino, M., Hunziker, J., Caspari, E., Quintal, B., Holliger, K., and Krause, R. (2020). Fully-automated adaptive mesh refinement for media embedding

- complex heterogeneities: application to poroelastic fluid pressure diffusion. *Computational Geosciences*, 24(3):1101–1120.
- Gassenmeier, M., Sens-Schönfelder, C., Delatre, M., and Korn, M. (2014). Monitoring of environmental influences on seismic velocity at the geological storage site for CO₂ in Ketzin (Germany) with ambient seismic noise. *Geophysical Journal International*, 200(1):524–533.
- Gassmann, F. (1951). Über die elastizität poroser medien (on the elasticity of porous media). *Vierteljahresschrift der Naturforschenden Gesellschaft Zürich*, 96(1–23).
- Giwelli, A., Sakaguchi, K., and Matsuki, K. (2009). Experimental study of the effect of fracture size on closure behavior of a tensile fracture under normal stress. *International Journal of Rock Mechanics & Mining Sciences*, 46(3):462–470.
- Glass, R. J., Nicholl, M. J., Rajaram, H., and Andre, B. (2004). Development of slender transport pathways in unsaturated fractured rock: Simulation with modified invasion percolation. *Geophysical Research Letters*, 31(6).
- Grab, M., Quintal, B., Caspari, E., Deuber, C., Maurer, H., and Greenhalgh, S. (2017a). The effect of boiling on seismic properties of water-saturated fractured rock. *Journal of Geophysical Research: Solid Earth*, 122(11):9228–9252.
- Grab, M., Quintal, B., Caspari, E., Maurer, H., and Greenhalgh, S. (2017b).

- Numerical modeling of fluid effects on seismic properties of fractured magmatic geothermal reservoirs. *Solid Earth*, 8(1):255–279.
- Grechka, V. and Kachanov, M. (2006). Effective elasticity of rocks with closely spaced and intersecting cracks. *Geophysics*, 71(3):D85–D91.
- Gunasekera, R. C., Foulger, G. R., and Julian, B. R. (2003). Reservoir depletion at the geysers geothermal area, california, shown by four-dimensional seismic tomography. *Journal of Geophysical Research: Solid Earth*, 108(B3).
- Guo, J., Rubino, J. G., Glubokovskikh, S., and Gurevich, B. (2017). Effects of fracture intersections on seismic dispersion: theoretical predictions versus numerical simulations. *Geophysical Prospecting*, 65(5):1264–1276.
- Gurevich, B., Brajanovski, M., Galvin, R. J., Müller, T. M., and Toms-Stewart, J. (2009). P-wave dispersion and attenuation in fractured and porous reservoirs—poroelasticity approach. *Geophysical Prospecting*, 57(2):225–237.
- Hall, Matt; Dramsch, J. (2015). Reflection.py. <https://github.com/agile-scientific/bruges/blob/main/bruges/reflection/reflection.py>, accessed July 18, page 2022.
- Haskell, N. A. (1953). The dispersion of surface waves on multilayered media. *Bulletin of the Seismological Society of America*, 43(1):17–34.

- Hatton, C., Main, I., and Meredith, P. (1994). Non-universal scaling of fracture length and opening displacement. *Nature*, 367(6459):160–162.
- He, Y., Rubino, J. G., Solazzi, S. G., Barbosa, N. D., Favino, M., Chen, T., Gao, J., and Holliger, K. (2022). Numerical upscaling of seismic signatures of poroelastic rocks containing mesoscopic fluid-saturated voids. *Journal of Geophysical Research: Solid Earth*, 127(6):e2021JB023473.
- Herwanger, J., Worthington, M., Lubbe, R., Binley, A., and Khazanehdari, J. (2004). A comparison of cross-hole electrical and seismic data in fractured rock. *Geophysical Prospecting*, 52(2):109–121.
- Hillers, G., Husen, S., Obermann, A., Planès, T., Larose, E., and Campillo, M. (2015). Noise-based monitoring and imaging of aseismic transient deformation induced by the 2006 basel reservoir stimulation. *Geophysics*, 80(4):KS51–KS68.
- Hirschberg, S., Wiemer, S., and Burgherr, P. (2015). Energy from the earth: Deep geothermal as a resource for the future? *TA-Swiss*, 62.
- Hobday, C. and Worthington, M. (2012). Field measurements of normal and shear fracture compliance. *Geophysical Prospecting*, 60(3):488–499.
- Holmgren, M. (2006). X steam for matlab. *www.x-eng.com*, accessed June, 21:2022.
- Hu, R., Zhou, C.-X., Wu, D.-S., Yang, Z., and Chen, Y.-F. (2019). Roughness

- control on multiphase flow in rock fractures. *Geophysical Research Letters*, 46(21):12002–12011.
- Hunziker, J., Favino, M., Caspari, E., Quintal, B., Rubino, J. G., Krause, R., and Holliger, K. (2018). Seismic attenuation and stiffness modulus dispersion in porous rocks containing stochastic fracture networks. *Journal of Geophysical Research: Solid Earth*, 123(1):125–143.
- Intergovernmental Panel on Climate Change (2022). *Global Warming of 1.5°C: IPCC Special Report on Impacts of Global Warming of 1.5°C above Pre-industrial Levels in Context of Strengthening Response to Climate Change, Sustainable Development, and Efforts to Eradicate Poverty*. Cambridge University Press.
- Kazemeini, S. H., Juhlin, C., and Fomel, S. (2010). Monitoring CO₂ response on surface seismic data; a rock physics and seismic modeling feasibility study at the CO₂ sequestration site, Ketzin, Germany. *Journal of Applied Geophysics*, 71(4):109–124.
- Kohl, T., Signorelli, S., Engelhardt, I., Andenmatten Berthoud, N., Sellami, S., and Rybach, L. (2005). Development of a regional geothermal resource atlas. *Journal of Geophysics and Engineering*, 2(4):372–385.
- Kong, L., Gurevich, B., Müller, T. M., Wang, Y., and Yang, H. (2013). Effect of fracture fill on seismic attenuation and dispersion in fractured porous rocks. *Geophysical Journal International*, 195(3):1679–1688.

- Lei, Q. and Sornette, D. (2021). Transport and localization of elastic waves in two-dimensional fractured media: Consequences on scattering attenuation. *Journal of Geophysical Research: Solid Earth*, 126(6):e2020JB021178.
- Lissa, S., Barbosa, N. D., and Quintal, B. (2021). Fluid pressure diffusion in fractured media: the role played by the geometry of real fractures. *Journal of Geophysical Research: Solid Earth*, 126(10):e2021JB022233.
- Lubbe, R., Sothcott, J., Worthington, M., and McCann, C. (2008). Laboratory estimates of normal and shear fracture compliance. *Geophysical Prospecting*, 56(2):239–247.
- Lubbe, R. and Worthington, M. (2006). A field investigation of fracture compliance. *Geophysical Prospecting*, 54(3):319–331.
- Makurat, A., Barton, N., Tunbridge, L., and Vik, G. (1991). The measurement of the mechanical and hydraulic properties of rock joints at different scales in the stripa project. *Publikasjon-Norges Geotekniske Institutt*, 182:1–8.
- Masson, Y. J. and Pride, S. R. (2007). Poroelastic finite difference modeling of seismic attenuation and dispersion due to mesoscopic-scale heterogeneity. *Journal of Geophysical Research: Solid Earth*, 112(B3).
- Mavko, G., Mukerji, T., and Dvorkin, J. (1998). *The Rock Physics Handbook*. Cambridge University Press, New York.

- Milani, M., Rubino, J. G., Müller, T. M., Quintal, B., Caspari, E., and Holliger, K. (2016). Representative elementary volumes for evaluating effective seismic properties of heterogeneous poroelastic media. *Geophysics*, 81(2):D169–D181.
- Müller, T. M., Gurevich, B., and Lebedev, M. (2010). Seismic wave attenuation and dispersion resulting from wave-induced flow in porous rocks—A review. *Geophysics*, 75(5):75A147–75A164.
- Myer, L., Hopkins, D., Peterson, J., and Cook, N. (1995). Seismic wave propagation across multiple fractures. In Myer, L., Cook, N., R.E., G., and C.F., T., editors, *Fractured and Jointed Rock Masses*, pages 105–109. Balkema.
- Nakagawa, S. and Schoenberg, M. A. (2007). Poroelastic modeling of seismic boundary conditions across a fracture. *The Journal of the Acoustical Society of America*, 122(2):831–847.
- Obermann, A., Kraft, T., Larose, E., and Wiemer, S. (2015). Potential of ambient seismic noise techniques to monitor the St. Gallen geothermal site (Switzerland). *Journal of Geophysical Research: Solid Earth*, 120(6):4301–4316.
- Obermann, A., Planès, T., Larose, E., and Campillo, M. (2013). Imaging preruptive and coeruptive structural and mechanical changes of a volcano with ambient seismic noise. *Journal of Geophysical Research: Solid Earth*, 118(12):6285–6294.

- Olson, J. E. (2003). Sublinear scaling of fracture aperture versus length: an exception or the rule? *Journal of Geophysical Research: Solid Earth*, 108(B9).
- Planès, T., Obermann, A., Antunes, V., and Lupi, M. (2020). Ambient-noise tomography of the greater geneva basin in a geothermal exploration context. *Geophysical Journal International*, 220(1):370–383.
- Pollard, D. D. and Segall, P. (1987). Theoretical displacements and stresses near fractures in rock: With applications to faults, joints, veins, dikes, and solution surfaces. In Atkinson, B. K., editor, *Fracture Mechanics of Rock*, pages 277–349. Academic Press, London.
- Pratt, H., Swolfs, H., Brace, W., Black, A., and Handin, J. (1977). Elastic and transport properties of an in situ jointed granite. *International Journal of Rock Mechanics & Mining Sciences*, 14(1):35–45.
- Press, W. H., William, H., Teukolsky, S. A., Saul, A., Vetterling, W. T., and Flannery, B. P. (1986). *Numerical Recipes: The Art of Scientific Computing*. Cambridge University Press, New York.
- Prioul, R. and Jocker, J. (2009). Fracture characterization at multiple scales using borehole images, sonic logs, and walkaround vertical seismic profile. *AAPG Bulletin*, 93(11):1503–1516.
- Prioul, R., Jocker, J., Montaggioni, P., and Escaré, L. (2008). Fracture compliance estimation using a combination of image and sonic logs. In

- SEG Technical Program Expanded Abstracts 2008*, pages 314–318. Society of Exploration Geophysicists.
- Pyrak-Nolte, L., Cook, N., and Myer, L. (1987). Seismic Visibility Of Fractures. In Farmer, I., Daemen, J., Desai, C., Glass, C., and S.P., N., editors, *Rock Mechanics: Proceedings of the 28th US Symposium*, volume All Days. Balkema.
- Pyrak-Nolte, L. J., Myer, L. R., and Cook, N. G. (1990). Transmission of seismic waves across single natural fractures. *Journal of Geophysical Research: Solid Earth*, 95(B6):8617–8638.
- Quiroga, G. E., Rubino, J. G., Solazzi, S. G., Barbosa, N. D., Favino, M., and Holliger, K. (2023). Seismic signatures of partial steam saturation in fractured geothermal reservoirs: insights from poroelasticity. *Geophysics*, 88(5):1–68.
- Quiroga, G. E., Rubino, J. G., Solazzi, S. G., Barbosa, N. D., and Holliger, K. (2022). Effects of fracture connectivity on rayleigh wave dispersion. *Journal of Geophysical Research: Solid Earth*, 127(3):e2021JB022847.
- Quiroga, G. E., Ziyisyian, A. P. K., and Späth, F. (2018). AVO inversion on unconventional reservoirs: systematic estimation of uncertainty in the Vaca Muerta shale. *First Break*, 36(12):65–74.
- Renshaw, C. and Park, J. (1997). Effect of mechanical interactions on the scaling of fracture length and aperture. *Nature*, 386(6624):482–484.

- Roach, L. A., White, D. J., and Roberts, B. (2015). Assessment of 4D seismic repeatability and CO₂ detection limits using a sparse permanent land array at the Aquistore CO₂ storage site. *Geophysics*, 80(2):WA1–WA13.
- Rubino, J. G., Barbosa, N. D., Hunziker, J., and Holliger, K. (2022). Can we use seismic reflection data to infer the interconnectivity of fracture networks? *Geophysical Journal International*, 231(2):996–1010.
- Rubino, J. G., Caspari, E., Müller, T. M., and Holliger, K. (2017). Fracture connectivity can reduce the velocity anisotropy of seismic waves. *Geophysical Journal International*, 210(1):223–227.
- Rubino, J. G., Caspari, E., Müller, T. M., Milani, M., Barbosa, N. D., and Holliger, K. (2016). Numerical upscaling in 2-D heterogeneous poroelastic rocks: Anisotropic attenuation and dispersion of seismic waves. *Journal of Geophysical Research: Solid Earth*, 121(9):6698–6721.
- Rubino, J. G., Guarracino, L., Müller, T. M., and Holliger, K. (2013). Do seismic waves sense fracture connectivity? *Geophysical Research Letters*, 40(4):692–696.
- Rubino, J. G., Müller, T. M., Guarracino, L., Milani, M., and Holliger, K. (2014). Seismoacoustic signatures of fracture connectivity. *Journal of Geophysical Research: Solid Earth*, 119(3):2252–2271.
- Rubino, J. G., Ravazzoli, C. L., and Santos, J. E. (2009). Equivalent vis-

- coelastic solids for heterogeneous fluid-saturated porous rocks. *Geophysics*, 74(1):N1–N13.
- Rutqvist, J. (1995). Determination of hydraulic normal stiffness of fractures in hard rock from well testing. *International Journal of Rock Mechanics & Mining Sciences*, 32:513–523.
- Sánchez-Pastor, P., Obermann, A., Reinsch, T., Ágústsdóttir, T., Gunnarsson, G., Tómasdóttir, S., Hjörleifsdóttir, V., Hersir, G., Ágústsson, K., and Wiemer, S. (2021). Imaging high-temperature geothermal reservoirs with ambient seismic noise tomography, a case study of the Hengill geothermal field, SW Iceland. *Geothermics*, 96:102207.
- Scott, S. W. (2020). Decompression boiling and natural steam cap formation in high-enthalpy geothermal systems. *Journal of Volcanology and Geothermal Research*, 395:106765.
- Shapiro, N. M. and Campillo, M. (2004). Emergence of broadband Rayleigh waves from correlations of the ambient seismic noise. *Geophysical Research Letters*, 31(7).
- Shuey, R. (1985). A simplification of the Zoeppritz equations. *Geophysics*, 50(4):609–614.
- Silver, P. G., Daley, T. M., Niu, F., and Majer, E. L. (2007). Active source monitoring of cross-well seismic travel time for stress-induced changes. *Bulletin of the Seismological Society of America*, 97(1B):281–293.

- Socco, L., Foti, S., and Boiero, D. (2010). Surface-wave analysis for building near-surface velocity models — Established approaches and new perspectives. *Geophysics*, 75:91–110.
- Solazzi, S. G., Hunziker, J., Caspari, E., Rubino, J. G., Favino, M., and Holliger, K. (2020). Seismic signatures of fractured porous rocks: the partially saturated case. *Journal of Geophysical Research: Solid Earth*, 125(8):e2020JB019960.
- Solazzi, S. G., Lissa, S., Rubino, J. G., and Holliger, K. (2021). Squirt flow in partially saturated cracks: a simple analytical model. *Geophysical Journal International*, 227(1):680–692.
- Solazzi, S. G., Rubino, J., Müller, T. M., Milani, M., Guarracino, L., and Holliger, K. (2016). An energy-based approach to estimate seismic attenuation due to wave-induced fluid flow in heterogeneous poroelastic media. *Geophysical Journal International*, 207(2):823–832.
- Sotelo, E., Rubino, J. G., Solazzi, S. G., Barbosa, N. D., and Holliger, K. (2021). Fractures in low-permeability rocks: Can poroelastic effects associated with damage zones enhance their seismic visibility? *Journal of Geophysical Research: Solid Earth*, 126(5):e2020JB021155.
- Stein, S. and Wysession, M. (2003). *An introduction to seismology, earthquakes, and earth structure*. Blackwell, Malden.
- Stork, A. L., Allmark, C., Curtis, A., Kendall, J.-M., and White, D. J.

- (2018). Assessing the potential to use repeated ambient noise seismic tomography to detect CO₂ leaks: Application to the Aquistore storage site. *International Journal of Greenhouse Gas Control*, 71:20–35.
- Swiss Federal Office of Energy (2021). Energy strategy 2050. <https://www.bfe.admin.ch/bfe/en/home/policy/energy-strategy-2050.html/>. Accessed: 5th of July, 2023.
- Taira, T., Brenguier, F., and Kong, Q. (2015). Ambient noise-based monitoring of seismic velocity changes associated with the 2014 Mw 6.0 South Napa earthquake. *Geophysical Research Letters*, 42(17):6997–7004.
- Taira, T., Nayak, A., Brenguier, F., and Manga, M. (2018). Monitoring reservoir response to earthquakes and fluid extraction, Salton Sea geothermal field, California. *Science Advances*, 4(1):e1701536.
- Thomas, M., Ball, V., Blangy, J., and Tenorio, L. (2016). Rock-physics relationships between inverted elastic reflectivities. *The Leading Edge*, 35(5):438–444.
- Thomson, W. T. (1950). Transmission of elastic waves through a stratified solid medium. *Journal of Applied Physics*, 21(2):89–93.
- Thurber, C. H. (1983). Earthquake locations and three-dimensional crustal structure in the Coyote Lake area, central California. *Journal of Geophysical Research: Solid Earth*, 88(B10):8226–8236.

- Tiab, D. and Donaldson, E. C. (2015). *Petrophysics: theory and practice of measuring reservoir rock and fluid transport properties*. Gulf Professional Publishing.
- Toledo, T., Obermann, A., Verdel, A., Martins, J., Jousset, P., Mortensen, A., Erbas, K., and Krawczyk, C. (2022). Ambient seismic noise monitoring and imaging at the Theistareykir geothermal field (Iceland). *Journal of Volcanology and Geothermal Research*, page 107590.
- Verdon, J. P. and Wüstefeld, A. (2013). Measurement of the normal/tangential fracture compliance ratio (z_n/z_t) during hydraulic fracture stimulation using s-wave splitting data. *Geophysical Prospecting*, 61:461–475.
- Vermilye, J. M. and Scholz, C. H. (1995). Relation between vein length and aperture. *Journal of Structural Geology*, 17(3):423–434.
- Vinci, C., Renner, J., and Steeb, H. (2014). On attenuation of seismic waves associated with flow in fractures. *Geophysical Research Letters*, 41(21):7515–7523.
- Wang, Q.-Y. and Yao, H. (2020). Monitoring of velocity changes based on seismic ambient noise: A brief review and perspective. *Earth and Planetary Physics*, 4(5):532–542.
- Witherspoon, P. A., Wang, J. S., Iwai, K., and Gale, J. E. (1980). Validity

of cubic law for fluid flow in a deformable rock fracture. *Water Resources Research*, 16(6):1016–1024.

Yilmaz, Ö. (2001). *Seismic data analysis: Processing, inversion, and interpretation of seismic data*. Society of Exploration Geophysicists.

Zangerl, C., Evans, K., Eberhardt, E., and Loew, S. (2008). Normal stiffness of fractures in granitic rock: A compilation of laboratory and in-situ experiments. *International Journal of Rock Mechanics & Mining Sciences*, 45(8):1500–1507.